The Dissertation Committee for Erin Frances Gauger certifies that this is the approved version of the following dissertation:

Production of beauty-hadron decay electrons in Pb-Pb collisions at $\sqrt{s_{\rm NN}} = 5.02$ TeV in ALICE

Committee:

Christina Markert, Supervisor

Deepa Thomas, Co-Supervisor

Irene Gamba

Can Kilic

Peter Onyisi

Production of beauty-hadron decay electrons in Pb-Pb collisions at $\sqrt{s_{\rm NN}} = 5.02$ TeV in ALICE

by

Erin Frances Gauger

DISSERTATION

Presented to the Faculty of the Graduate School of
The University of Texas at Austin
in Partial Fulfillment
of the Requirements
for the degree of

DOCTOR OF PHILOSOPHY

THE UNIVERSITY OF TEXAS AT AUSTIN
May 2021

To my teachers.

Acknowledgements

I dedicate this thesis to my teachers, everyone from Ms. Foti in my pre-K class at Rockefeller Elementary to my professors in grad school. Without their help and instruction I would have never made it this far. I would particularly like to thank Prof. Jason Woods who steered me toward a physics degree when I started undergrad and Prof. Mark Conradi, who was my undergraduate research advisor and allowed me to destroy many, many fuses in his NMR lab. (That's why they're there!)

My thanks also go to my parents (my very first teachers) and my two brothers Ryan and Daniel. Thank you for dealing with a sometimes angsty young Erin who really just wanted to read books all the time. Thanks also to Michael, who kept me sane the last few years of my PhD.

Last but not least, I would like to thank my research family. Thank you to Prof. Christina Markert, my advisor, for supporting my research these seven years. Thank you to Dr. Deepa Thomas, who offered a vast amount of help with my analysis and was seemingly always available to answer questions via chat. Thanks also to the PMA 10.310 crew (Alex Jentsch, Justin Blair, Ryan Hannigan, Amanda Flores, and Josey Wright) for offering commiseration and support. Thank you to Dr. Lanny Ray for help with understanding theory and finishing pitchers of dark beer. Finally, in memoriam of Prof. Jerry Hoffman, whose voice I can still hear saying, "It's four o'clock!"

Production of beauty-hadron decay electrons in Pb-Pb collisions at $\sqrt{s_{\rm NN}} = 5.02$ TeV in ALICE

Publication No. _____

Erin Frances Gauger, Ph.D.
The University of Texas at Austin, 2021

Supervisors: Christina Markert, Deepa Thomas

High energy heavy-ion collisions provide us with the unique opportunity to study the Quark-Gluon Plasma (QGP) in a laboratory setting. The QGP is a special state of matter in which quarks and gluons, fundamental particles that compromise the nuclei of atoms, are deconfined, not bound into larger particles (hadrons). The QGP lasts for only a short time – on the order of 10^{-23} seconds – and therefore cannot be measured directly. However, a useful probe of the QGP is the beauty quark, which is created in the first moments of a heavy-ion collision and experiences the full evolution of the QGP. As they travel through the QGP, beauty quarks interact with the other partons (quarks and gluons) via elastic and inelastic scattering [gluon bremsstrahlung], produce quark and antiquark pairs, and lose energy. The beauty quarks later form larger bound states (like B mesons), which further decay into particles such as electrons before reaching detectors.

In this thesis, electrons from beauty hadron decays (beauty-decay electrons) are measured in heavy ion collisions of lead-on-lead ions (Pb-Pb) at center-of-mass energy per nucleon pair $\sqrt{s_{\rm NN}} = 5.02$ TeV with the ALICE detector at the LHC. The analysis is conducted separately for collisions with 0-10% centrality (i.e. most "head-on" collisions) and 30-50% centrality (i.e. slightly off-center collisions). The results will be compared with previous measurements of heavy-flavor (charm and beauty) decay electrons and with theoretical predictions.

Contents

List of Figures

Chapter 1: Introduction

The Large Hadron Collider (LHC), located at the European Organization for Nuclear Research (CERN), is the largest and most powerful particle accelerator in the world. One of the four main experiments at the LHC is ALICE, A Large Ion Collider Experiment. ALICE is specifically designed to study heavy ion collisions, with the goal of understanding a unique state of matter known as the Quark-Gluon Plasma (QGP) [1]. The QGP is a "soup" of deconfined quarks and gluons. Quarks and gluons are fundamental particles that only appear in larger bound states in ordinary matter (see Section 1.1). Evidence of the QGP was first found with CERN's Super Proton Synchrotron (SPS) [2] and confirmed in 2005 by experiments studying high-energy heavy ion collisions at the Relativistic Heavy Ion Collider (RHIC) [3–6]. The ALICE collaboration seeks to understand more about this state of matter by studying the particles produced in heavy ion collisions, specifically in collisions of lead-on-lead ions. ALICE also studies proton-on-proton (pp) and proton-on-lead (p-Pb) collisions. The conditions produced in these collisions are not conducive to producing a quark-gluon plasma, so they provide useful baseline measurements to understand particle production in the absence of the QGP.

In this thesis in particular, the QGP is studied via measurements of beauty quarks. Beauty quarks are the second heaviest quark with a mass of ~ 4.2 GeV/c^2 [7]. Due to their high mass, they are created in the first moments of the collision via hard scatterings of the partons (quarks and gluons) in the colliding lead nuclei. They then experience the full evolution of the QGP medium, interacting with the other quarks and gluons via elastic collisions and inelastic processes (bremsstrahlung-like gluon radiation). In these interactions, beauty quarks lose energy, as discussed in further detail in Section 1.5. After traversing the QGP, beauty quarks combine with other quarks to form bound states known as hadrons. For example, a beauty anti-quark can become bound with an up quark to form a B^+. A selected number of beauty hadrons and their quark content is listed in Table 1.1.

The beauty hadrons then undergo weak decays into final state particles that we ultimately measure in our detectors. Many of these final state particles include electrons; about 20% of beauty hadrons decay into states that include an electron (B→e).

Table 1.1: Quark content of beauty hadrons. Up, down, strange, and beauty are abbreviated as u, d, s, and b respectively.

Hadron species	Quark content
B^+	u, $\overline{b}$
B^0	d, $\overline{b}$
B_s^0	s, $\overline{b}$
Λ_b^0	u, d, b

An example of a beauty hadron decay is shown in Figure 1.1. Because a large fraction of beauty hadrons decay into electrons, it is experimentally convenient to study beauty by measuring their decay electrons ("beauty-decay electrons"). Electrons are easily identified using the ALICE detector, as they produce a clean signal in different subdetectors (see Sections 2.2.2 and 2.2.3).

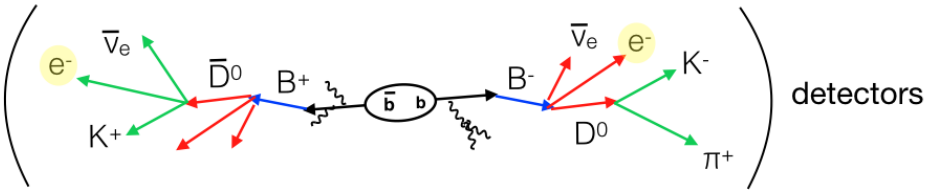

Figure 1.1: A schematic example of the hadronization and decay of a beauty quark pair created in a heavy ion collision. The beauty quarks hadronize to B^+ and B^-, which further decay and produce electrons, which are highlighted in yellow.

In this thesis, beauty-decay electron production as a function of momentum is measured in Pb-Pb collisions at a center-of-mass per nucleon pair of $\sqrt{s_{\mathrm{NN}}} = 5.02$ TeV with the ALICE detector. This yield can be compared with the beauty-decay electron yield in pp collisions to see if the presence of the QGP modifies the momentum distribution of beauty-decay electrons (see Section 1.6). If the beauty quark loses energy via interactions with the QGP constituents, we can expect to see that the momentum distribution of beauty-decay electrons in Pb-Pb collisions is shifted to lower values when compared with pp collisions (where no QGP is produced). In addition, this measurement can be compared with measurements of electrons from charm decays to see if energy loss in the QGP has a mass-dependence. (The charm quark is roughly a quarter of the mass of the beauty quark.)

This measurement is also performed for Pb-Pb collisions with different "centralities." Centrality, discussed in greater detail in Section 2.2.4, provides information about the impact parameter of the colliding lead nuclei and is correlated with the size of the produced QGP. In this thesis, beauty-decay electrons are measured in Pb-Pb collisions with 0-10% and 30-50% centrality. This corresponds to the most head-on collisions and slightly off-center collisions respectively. Comparing these two measurements will allow us to determine how the QGP size affects the beauty quark, and whether it loses more energy in head-on collisions that form a larger and denser QGP. Finally, the results can be compared with theoretical predictions to test our current understanding of energy loss processes and the properties of the QGP.

This thesis is organized as follows. The remainder of this chapter gives necessary background information about the fundamental forces and particles of our universe and the experimental observables and predictions we use to extract physics information. Chapter 2 provides a description of the LHC and the ALICE detector used to measure heavy-ion collisions. Chapter 3 and 4 give the technical details of the measurement and the associated systematic uncertainties. The final results and discussion are presented in Chapter 5. Finally, Chapter 6 summarizes the work and provides an outlook of future beauty measurements.

1.1 Fundamental particles and forces

In the 8th century BCE, the Vedic sage Aruni conjectured that the world is composed of particles too small to be seen by the naked eye. A few centuries later, Greek philosophers Leucippus and Democritus esposed a similar theory of indivisible, fundamental particles [8]. It took scientists a few centuries to dig down to such small scales, first with the discovery of the cell by Robert Hooke in the 17th century [9], then with John Dalton's observations that chemical elements combine in such a manner that suggests they each have a fundamental unit of mass in the early 1800s [10]. After that, things moved relatively quickly (pardon the pun) to smaller and smaller scales, revealing what may be some of the fundamental particles that compose our universe.

As of today, we have observed a short list of fundamental particles (Figure 1.2) which are governed by four forces: electromagnetism, the weak force, the strong force,

and gravity. With the exception of gravity, all these forces can be described by the "Standard Model" of particle physics, which characterizes each force as an exchange of gauge bosons (force carrier particles). For example, electromagnetism, which is no doubt familiar to the reader, is mediated by photons, while the weak force is mediated by W and Z bosons. The weak force and electromagnetism have been successfully described together as different manifestations of the same phenomenon, known as electroweak interactions. The strong force, whose force carrier particles are known as gluons, is described by the theory known as Quantum Chromodynamics (QCD).

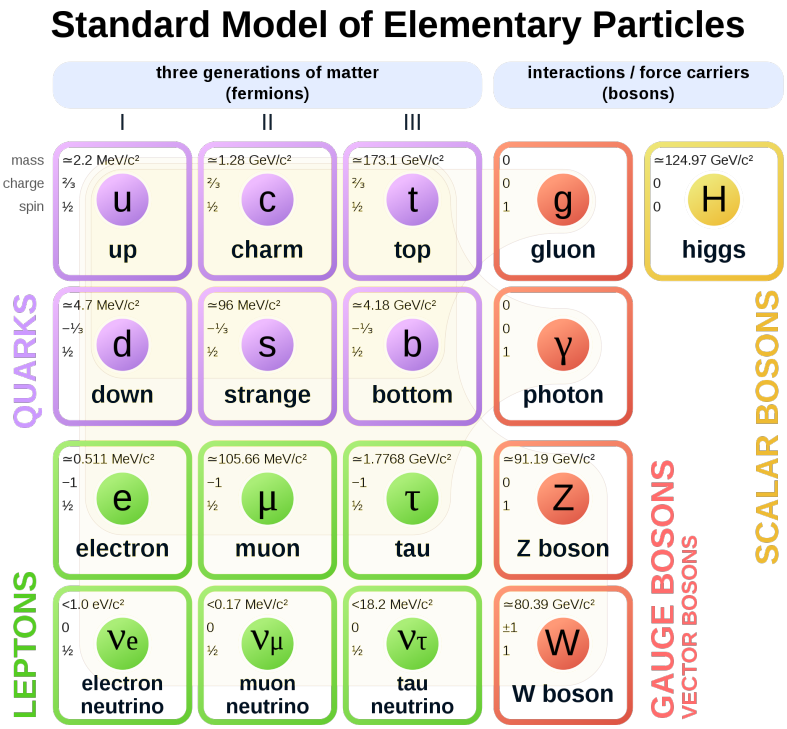

Figure 1.2: The fundamental particles of the standard model.

The strong force is the main phenomenon of interest in this thesis, and acts on particles with color charge. Color charge is an intrinsic property of certain particles (i.e. quarks and gluons); the color charges are red, green, and blue and their anti-charges anti-red, anti-green, and anti-blue[1]. Quarks carry a color charge, anti-quarks

[1]Particles with "color charge" are not colorful in the ordinary sense of the word. Though twisted outside their original meaning, the words of Democritus apply here: "color [exists only] by convention: in reality there is only atoms and void" [8].

carry an anti-color charge, and gluons carry both a color and anti-color charge. Since gluons themselves have color charges, they can self-interact.

The strong force works to create larger color-neutral bound states. Examples of a color-neutral state would be combining a red and anti-red quark to form a meson or combining a red, green, and blue particle to create a baryon. This is somewhat analogous to electromagnetism, which acts to combine positive and negative electric charges to create a neutral overall electric charge. Unlike electromagnetism, however, the effective coupling constant for a strong interaction, α_s, increases with increasing distance. As a consequence, free quarks and gluons are not found in nature. Instead, they are always bound into larger, color-neutral particles: a phenomenon known as confinement.

This poses a problem for experimentalists hoping to study the physics of individual quark and gluon interactions. If one were to attempt to pull apart the quarks bound in a color neutral object, the energy needed to pull them apart would be enough to create new quarks, as a quark and anti-quark pair, which would bind and create new neutral bound states. An illustration of this process is given in the cartoon in Figure 1.3.

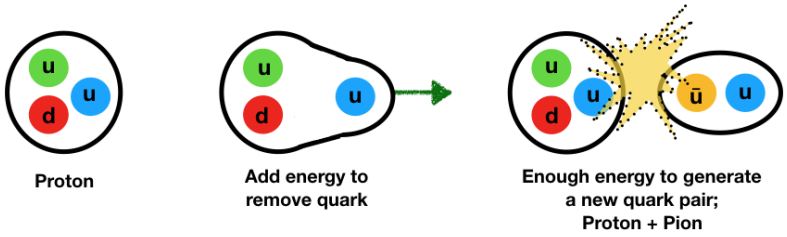

Figure 1.3: Illustration of confinement.

1.2 Quark-Gluon Plasma

The theoretical explanation of confinement came in 1973, when Gross and Wilczek and Politzer independently discovered the property of "asymptotic freedom" in QCD [11, 12]. At short, sub-nucleon distances the effective strong coupling constant α_s is small. However, for interactions with low momentum transfer squared (Q^2), corresponding to large, nuclear, distances, α_s becomes logarithmically large. This is due

to corrections for gluon vacuum polarization, which causes an anti-screening effect in strong force interactions.

Shortly after this discovery, Collins and Perry [13] and Cabibbo and Parisi [14] independently proposed the existence of a new state of matter, arising as a consequence of asymptotic freedom, in which quarks and gluons at high densities and temperatures would be effectively free to interact as though they were unbound. This soup of unbound quarks and gluons is called a Quark-Gluon Plasma (QGP), since it is somewhat analogous to an electromagnetic plasma with color charge instead of electric charge. QCD calculations performed on a discretized lattice in space and time (known as "lattice QCD") predicts that the phase transition from ordinary nuclear matter to a QGP requires energy densities above 0.5-1 GeV/fm^3 and temperatures above 150-170 MeV [15–17] (see Figure 1.4). For reference, the energy density of the nuclear ground state is only $\epsilon_0 \approx 0.15$ GeV/fm^3 [18].

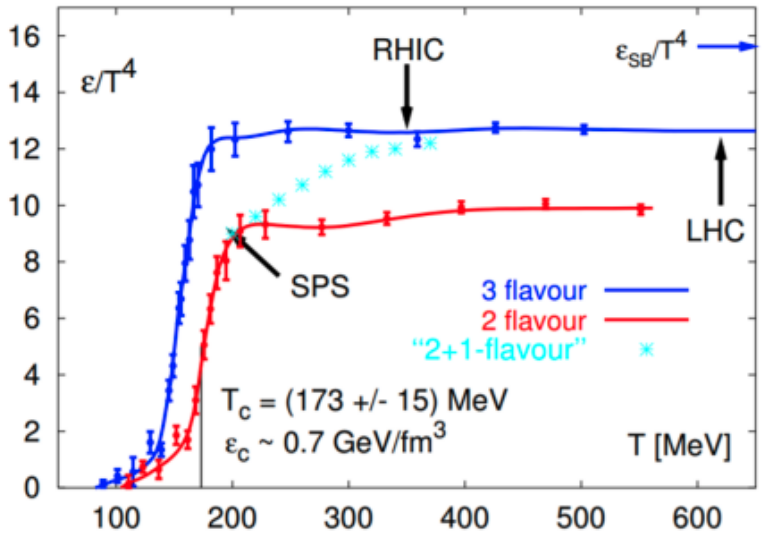

Figure 1.4: Lattice QCD calculations of energy density as a function of temperature (at zero baryon density) [15]. The sharp turn around T = 170 MeV indicates a phase transition.

In 1983, Bjorken proposed that the high energy densities required to produce a QGP might be achieved in relativistic heavy-ion collisions [19]. Several signatures of QGP formation were expected to be seen in subsequent experimental studies: enhancement of strange quark production [20], the "melting" and suppression of J/ψ

due to color screening [21, 22], and the dissipation and energy loss of jets as they traverse the QGP medium [23]. These QGP signatures were later found in heavy-ion collisions (see, for example, [24–27]). In addition, theory predictions that modeled the QGP as an ideal, equilibrated hydrodynamic fluid were successful in describing the azimuthal distributions of produced particles (see Section 1.7) and the hadron spectra and yield ratios [5]. This led to the conclusion that the QGP acts as a perfect liquid.

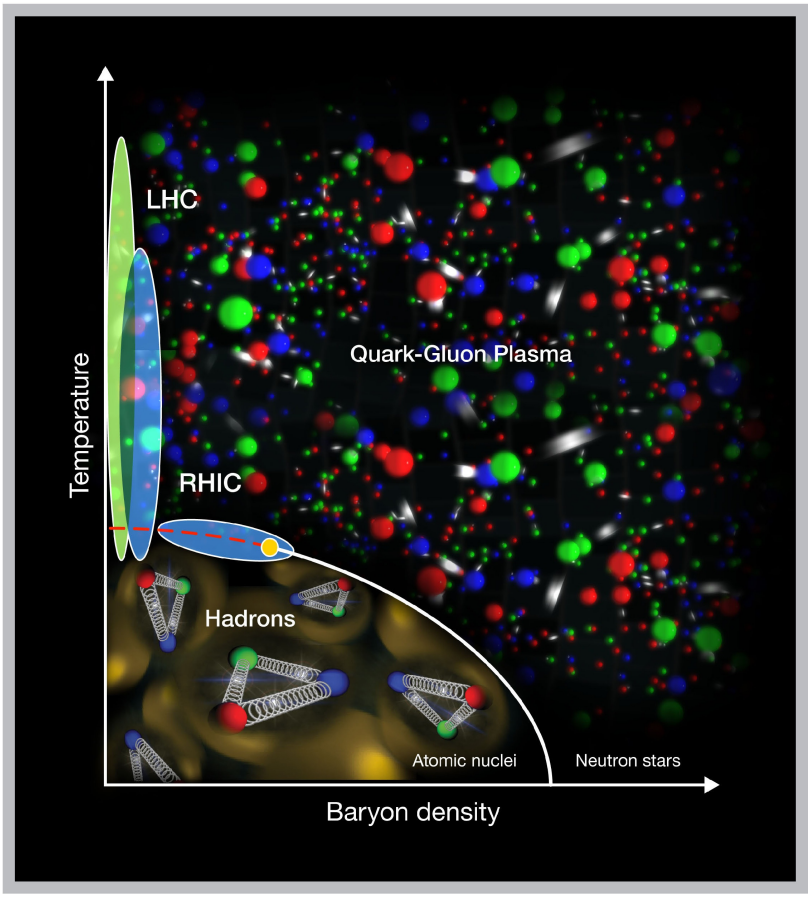

Figure 1.5: Phase diagram of hadronic matter. Collisions at the LHC are expected to cover the area denoted by the green oval at low net baryon density but high temperature. Image from Brookhaven National Laboratory.

Our current understanding of the behavior and phase of strongly-interacting hadronic matter is illustrated in Figure 1.5, which shows a phase diagram of nuclear matter as a function of the baryon density (or proton and neutron density) and

temperature. At low density and temperature, quarks are confined in hadrons and form a hadron gas. At high temperature and density, a phase transition occurs, and a QGP is formed. Collisions at the LHC are expected to cover the area denoted by the green oval at low net baryon density but high temperature. At low baryon density, high temperatures above 1.7×10^{12} K (150 MeV) are required for QGP formation [16, 17]. (For reference, the center of our sun is only about 2.7×10^{7} K [28].) In our current understanding, the universe was composed of a QGP a couple microseconds after the Big Bang. As the universe expanded and cooled, the quarks and gluons underwent a phase transition into the bound states we see in ordinary matter today. This is illustrated in Figure 1.6.

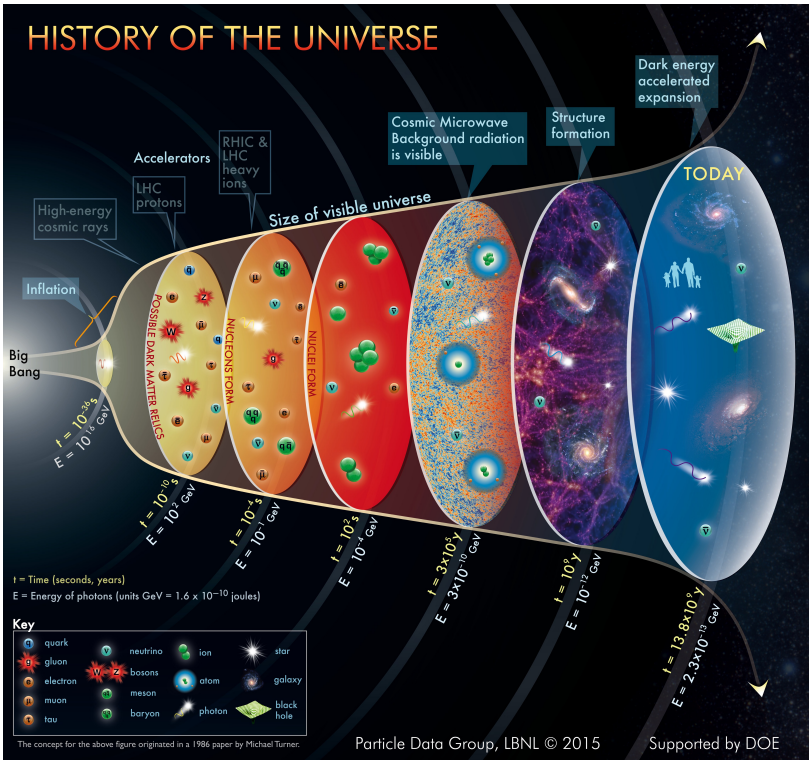

Figure 1.6: Expansion of the universe after the Big Bang. Image from the Particle Data Group at Lawrence Berkeley National Lab.

1.3 Heavy-ion collisions

Currently, the only way to achieve the conditions necessary to create a QGP in a laboratory setting is by colliding together large ions at relativistic energies. (Here, "ions" refer to atomic nuclei, fully stripped of their electrons.) At CERN and Brookhaven National Lab (BNL), heavy ions are accelerated to energies ranging from GeV to TeV beam energies. Depending on the center-of-mass energy of the collision, different sections of the hadronic phase diagram (Figure 1.5) can be investigated. In these collisions, a fraction of the center-of-mass energy is dissipated into a system of strongly interacting quarks and gluons; if the collision energy is high, a small droplet of QGP is formed [29]. In high-energy heavy-ion collisions, we can achieve high energy densities around 15-30 GeV/fm^3, well above the estimated $\sim$1 GeV/fm^3 threshold required for QGP formation [29].

Heavy-ion collisions are often described as a series of subsequent stages [30]. First, there are the initial conditions: two heavy ions (like Au or Pb), relativistically-flattened in the lab frame, collide together. Since these ions are large, they may not collide "head-on"; instead, they may have a non-zero impact parameter. Such collisions would have a smaller overlap between the colliding nuclei, and parts of the lead ions, known as spectators, would not participate in the collision, instead traveling straight down the beam pipe. Such a collision is illustrated in Figure 1.7.

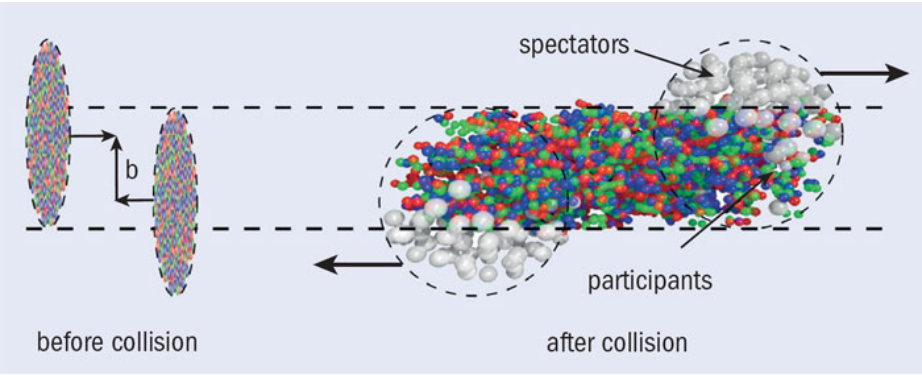

Figure 1.7: Illustration of the spectators and participants in an off-center heavy-ion collision. Image courtesy of the CERN Courier [31].

Many partons (quarks and gluons) are produced in the high-energy environment. These partons rapidly interact via elastic and inelastic collisions, forming a QGP

medium. The QGP is often described as an equilibrated, zero-viscosity fluid due to the success of ideal hydrodynamic models in reproducing azimuthal anisotropy measurements ("elliptic flow") [5, 32], discussed in Section 1.7. From ideal hydrodynamic models, the QGP is estimated to reach thermal equilibrium around 0.3 fm/c after the collision [33], and only lasts a few fm/c before the system has expanded and cooled to a certain critical temperature T_c. This expansion is caused by the large pressure gradient between the surrounding vacuum and the QGP.

At T_c, the partons start to become bound together into larger particles called *hadrons*. (Hadrons that are composed of two quarks are known as mesons, while hadrons with three quarks are known as baryons.) About 95% of the particles produced in heavy-ion collisions are hadrons (mostly pions) with $p_{\mathrm{T}} < 2$ GeV/c [1], where p_{T} is the component of momentum perpendicular to the beam-line axis (see Figure 1.11). Hadronization can be described via two main mechanisms. The first is fragmentation, in which quarks are produced via QCD processes in the strong color field surrounding a free color charge. The newly produced quarks then bind with the original quark. The second process is coalescence [34], in which quarks that are close in phase space within the QGP are bound together. After formation, hadrons may interact further, until a later "kinetic freeze-out," at which point the particle density is low enough that the hadrons can no longer interact. The hadrons then free-stream unimpeded away from the collision site, perhaps undergoing further decay processes and hitting detectors. An illustration of these stages is given in Figure 1.8.

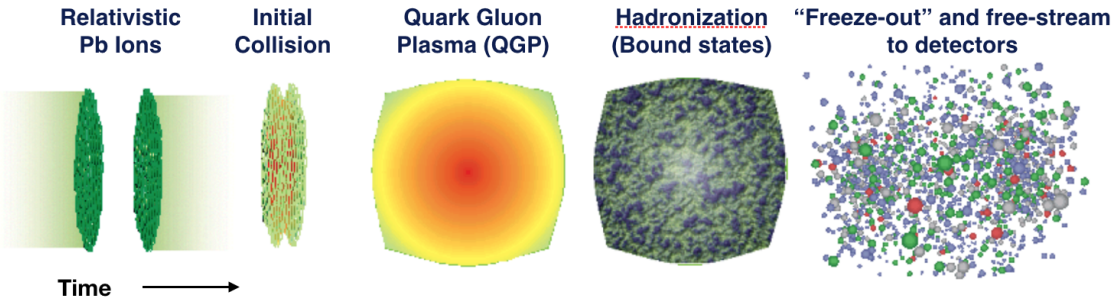

Figure 1.8: The stages of a heavy-ion collision. In this case, the incident nuclei are Pb ions. Image adapted from S.A. Bass.

Given the short time scales of these processes, it is impossible to directly measure the QGP. The physics of the QGP must instead be inferred from the decay particles

that hit detectors well after the QGP has dissipated. In our case, electrons from beauty-hadron decays, often referred to as "beauty-decay electrons" in this thesis, are studied to glean information about the energy loss of beauty quarks as they travel through the QGP.

1.4 Heavy-flavor probes

Beauty-decay electrons fall into the broader category of heavy-flavor studies in high-energy nuclear physics. Here, "heavy-flavor" refers to charm and beauty quarks, since they have large masses ($m_c \approx 1.3$ GeV/c^2 and $m_b \approx 4.2$ GeV/c^2 versus $m_u \approx 2.2$ MeV/c^2 and $m_d \approx 4.7$ MeV/c^2).

In general, heavy-flavor quarks make excellent probes of heavy-ion collisions. Because of their high mass, they are almost exclusively produced via hard parton-parton scattering in the first moments of a heavy-ion collision (~ 0.1 fm/c), and their production can be reliably calculated using pQCD [35]. They then experience the full evolution of the collision while maintaining their flavor identity: a charm or beauty quark will remain a charm or beauty quark for the duration of the QGP phase of the collision (see Section 1.3), which exists for about 10 fm/c. Only after hadronization do charm and beauty quarks undergo weak decays to lighter flavors. As they traverse the QGP, heavy quarks interact with the partons of the QGP and lose energy via elastic collisions and bremsstrahlung-like gluon radiation [1]. They then form bound-state hadrons, forming D or B mesons for example, which consist of a charm or beauty quark, respectively, and one of the light quarks (up, down, and strange):

Heavy-flavor hadronization

$$b \rightarrow B^+(u\bar{b}), B^-(\bar{u}b), B^0(d\bar{b}), \overline{B}^0(\bar{d}b), \ ...$$
$$c \rightarrow D^+(c\bar{d}), D^-(\bar{c}d), D^0(c\bar{u}), \overline{D}^0(\bar{c}u), \ ...$$

The heavy-flavor hadrons decay into other particles before reaching detectors. Some examples of decay processes are listed in Table 1.2, along with their branching ratios. The branching ratio is the fraction of the hadron species that decay via a particular mode. A full list of known decays and their measured branching ratios can be found in Ref. [7].

Table 1.2: Decay modes and branching ratios of heavy-flavor hadrons [7].

Decay mode	Branching ratio
$D^0 \to K^+\pi^-$	$\sim 3.95\%$
$D^0 \to e^+$anything	$\sim 6.49\%$
$D^+ \to K^-\pi^+\pi^+$	$\sim 9.38\%$
$D^+ \to e^+$semileptonic	$\sim 16.07\%$
$B^0 \to D^-\pi^+$	$\sim 0.252\%$
$B^0 \to e^+\nu_e X_c$	$\sim 10.1\%$
$B^+ \to J/\psi K^+$	$\sim 0.1\%$
$B^+ \to e^+\nu_e X_c$	$\sim 10.8\%$

Experimentally, heavy-flavor particles are measured using two main approaches. The first is to reconstruct heavy-flavor hadrons by measuring the products of one of their decay modes. For example, the D^+ ($c\bar{d}$) meson can be reconstructed via its decay into $K^-\pi^+\pi^+$ by calculating the invariant mass of combinations of kaons and pions (π) and selecting combinations that give the mass of the mother D^+ particle [36]. The second approach is to measure the electrons or muons from heavy-flavor decays.

Fully reconstructing beauty hadrons is challenging in heavy-ion collisions. Decay modes with large branching ratios and better statistics often contain many final state particles, making them difficult to reconstruct in the high multiplicity (large particle production) environment. To date, the only beauty hadron that has been measured via reconstruction in heavy-ion collisions is the B^+ ($u\bar{b}$) meson [37], measured via its decay into K^+ and J/ψ, which itself further decays into an electron-positron pair. This decay channel $B^+ \to K^+ J/\psi(\to e^+e^-)$ has a small branching ratio of about 0.006%.

On the other hand, beauty hadron decays that produce an electron have large branching ratios. About 10% of beauty hadrons decay directly into electrons (b→e), and ∼10% decay into charm hadrons, which can further decay into electrons (b→c→e). This makes it advantageous to study beauty by measuring beauty-decay electrons. The combination of the large branching ratio and the electron identification capabilities of the ALICE detector (Chapter 2) gives a large, clean signal that allows for differential measurements with good significance. The disadvantage of this method is that it is not as direct; the correlation between the properties of the decay electron and the original beauty quark is fairly broad.

In this thesis, we take this second approach and study the behavior of beauty quarks in heavy-ion collisions by measuring the electrons from beauty hadron decays as a proxy. In particular, we hope to learn more about the interactions and energy loss of the beauty quark by measuring the nuclear modification factor (R_{AA})), discussed in Section 1.6. Section 1.7 describes the complementary measurement v_2, also known as elliptic flow, which contains information about the azimuthal anisotropy of particle production.

1.5 Energy loss in the QGP

One of the signatures of the formation of a QGP in heavy-ion collisions is the energy loss of "hard probes," particles with a large transverse momentum and/or mass that are produced in the first moments of a heavy-ion collision via hard scatterings of the partons in the colliding nuclei. Included in this category are high-momentum pions (composed of up and down quarks) and heavy-flavor particles, discussed in Section 1.4. These particles can be used as internal probes, traveling through the QGP medium created in a heavy ion collision. This is illustrated on the left of Figure 1.9, where a pair of generated quarks (red arrows) is depicted traveling through the QGP medium created by the collision of two heavy ions (blue ellipses). As they travel, the quarks lose energy to the dense partonic medium. In general, this energy loss is determined by the characteristics of the quark (energy E and mass m), the properties of the QGP (temperature T and thickness L), and the strength of the interaction coupling between the quark and the medium α: $\Delta E(E, m, T, L, \alpha)$ [1].

The total energy loss of a quark traveling through the QGP is due to both collisional and radiative processes [1]. The collisional energy loss is due to elastic scatterings with the QGP parton constituents, while the radiative energy loss is due to gluon bremsstrahlung processes. Example diagrams of these processes are shown in the middle and right of Figure 1.9.

The amount of energy loss expected from these processes depends on the particle traveling through the medium. First, gluons are expected to lose more energy than quarks. Since gluons have two color charges, they have a stronger color coupling to the medium and are more likely to lose energy. This would also have an effect on light quark production; since gluon pair-production is more likely to produce light-flavor

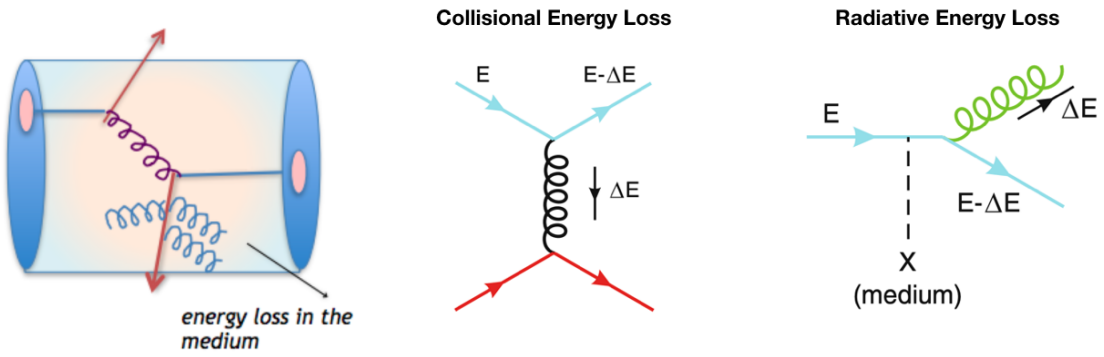

Figure 1.9: Left: an illustration of how quarks travel through the QGP, acting as internal probes of the collision system. Middle and right: Diagrams of collisional and radiative energy loss processes respectively of a quark with energy E as it travels through the QGP. Adapted from [1].

quarks, gluon energy loss might result in the production of lower-energy light-flavor quarks.

Second, the energy loss is expected to be mass-dependent. Collisional energy loss has less of an effect on heavier objects (imagine a bowling ball traveling through ping-pong balls). Energy loss via gluon bremsstrahlung is also dependent on the mass of the quark. This is known as the "dead cone effect" [38]: gluon radiation is suppressed within the opening angle θ, which is dependent on the ratio of the quark's mass and energy $M_{\mathrm{q}}/E_{\mathrm{q}}$. The dead cone effect is illustrated in Figure 1.10. Since heavy-flavor quarks have a larger mass, they would have a larger "dead cone" and therefore lose less energy via radiation.

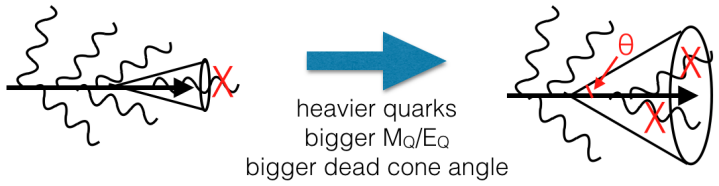

Figure 1.10: Illustration of the dead cone effect.

With the color- and mass-dependent effects in mind, it is expected that gluons would lose the most energy in the QGP, followed by the light quarks (u,d,s), charm

quarks, and beauty quarks in that order:

$$\Delta E_{gluon} > \Delta E_{u,d,s} > \Delta E_c > \Delta E_b \tag{1.1}$$

1.6 Nuclear modification factor

One of the experimental observables used to gain information about energy loss in the QGP phase of heavy-ion collisions is called the nuclear modification factor, or R_{AA}. The R_{AA} compares the momentum distribution of a specific particle in heavy ion collisions (A-A) with the momentum distribution of that same particle in proton-on-proton (pp) collisions:

$$R_{\mathrm{AA}} = \frac{dN_{\mathrm{AA}}/dp_{\mathrm{T}}}{\langle N_{\mathrm{coll}} \rangle \cdot dN_{\mathrm{pp}}/dp_{\mathrm{T}}} = \frac{dN_{\mathrm{AA}}/dp_{\mathrm{T}}}{\langle T_{\mathrm{AA}} \rangle \cdot d\sigma_{\mathrm{pp}}/dp_{\mathrm{T}}} \tag{1.2}$$

Here, p_{T} is the transverse momentum of the particle, i.e. the component of momentum perpendicular to the heavy-ion beam axis, $p_{\mathrm{T}} = \sqrt{p_{\mathrm{x}}^2 + p_{\mathrm{y}}^2}$ (see Figure 1.11). $dN_{\mathrm{AA}}/dp_{\mathrm{T}}$ is the p_{T}-differential yield of a certain particle in heavy-ion collisions and $dN_{\mathrm{pp}}/dp_{\mathrm{T}}$ is the p_{T}-differential yield of the same particle in pp collisions.

The $\langle N_{\mathrm{coll}} \rangle$ term is the average number of binary nucleon-nucleon collisions in a heavy ion collision. This value is dependent on the geometry and impact parameter of the collision, since off-center collisions like the one in Figure 1.7 would have a smaller N_{coll}. It is more common to express the N_{coll} as the product of the nuclear thickness function T_{AA}, which characterizes the density in the overlap region of the incident nuclei for a given impact parameter, and the inelastic cross section for pp collisions $\sigma_{\mathrm{pp}}^{\mathrm{inel}}$: $N_{\mathrm{coll}} = T_{\mathrm{AA}} \cdot \sigma_{\mathrm{pp}}^{\mathrm{inel}}$. The T_{AA} is estimated using the Glauber model [39–41], which is discussed in more detail in Section 2.2.4.1.

If the $R_{\mathrm{AA}} = 1$, this would indicate that a particle's production, on average, is the same in a heavy-ion collision as it would be in a superposition of pp collisions. If, however, the R_{AA} deviates from one, the particle's momentum distribution has been altered by nuclear matter effects. The principle effect of interest in this thesis is the modification of the momentum spectrum due to quark energy loss in the QGP, discussed in Section 1.5. However, this must be disentangled from other phenomenon known as cold nuclear matter (CNM) effects, detailed in the following Section 1.6.1.

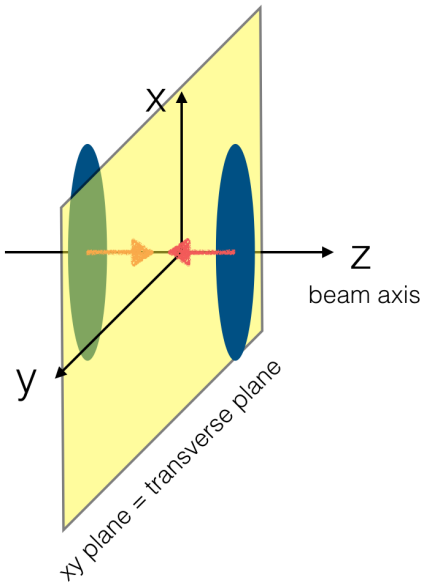

Figure 1.11: The coordinate system used to define the transverse (xy) plane. The heavy-ion beams run parallel to the z-axis.

1.6.1 Cold nuclear matter effects and R_{pA}

There are several phenomena unrelated to the presence of a QGP that might influence the nuclear modification factor of a given particle. These are referred to as "cold nuclear matter" (CNM) effects, and need to be understood and separated from the QGP effects we wish to study. The CNM effects include 1) the modification of the nucleon parton distribution functions in heavy nuclei, 2) interactions among the incoming parent partons when the nuclei penetrate each other, but before the production of the daughter quark of interest, and 3) interactions with the passing-by remnants of the colliding nuclei [35]. For example, a quark can undergo multiple interactions with cold nuclear matter, via coherent and incoherent scattering processes [42]. The size of such effects on the R_{AA} are studied using collisions of protons with heavy ions (p-A collisions), where we assume the "hot" nuclear matter effects are small or negligible. To test this, one can calculate the R_{pA}, calculated in the same manner as R_{AA} by comparing the momentum distribution in p-A collisions with the scaled momentum distribution in pp collisions.

The left panel of Figure 1.12 shows the R_{pPb}, i.e. the nuclear modification factor

in proton-lead collisions, of D mesons measured with ALICE [43]. The measurement is consistent with one within the uncertainties of the measurement, signaling that the CNM effects have a negligible effect on the momentum distribution of D mesons. This is consistent with several model predictions, also shown in Figure 1.12, which include CNM effects. The prediction by Kang et al. [44] has a different trend w.r.t. the other predictions, and primarily focuses on the effects of incoherent scattering processes of the charm quark with the cold nuclear medium. This model is excluded by the data for $p_{\mathrm{T}} < 4$ GeV/c, indicating that perhaps the effect of these scattering processes is overestimated by the model for D mesons in this kinematic range.

Measurements of both heavy-flavor mesons and decay leptons in p-A collisions have also shown that CNM effects are small [35]. For example, the R_{pPb} of beauty-decay electrons [45], the particles of interest in this thesis, is shown in the right panel of Figure 1.12. There, the R_{pPb} is consistent with unity within the uncertainty of the measurement. Similar to the D meson measurement, the beauty-decay electron R_{pPb} is consistent with model predictions that include CNM effects.

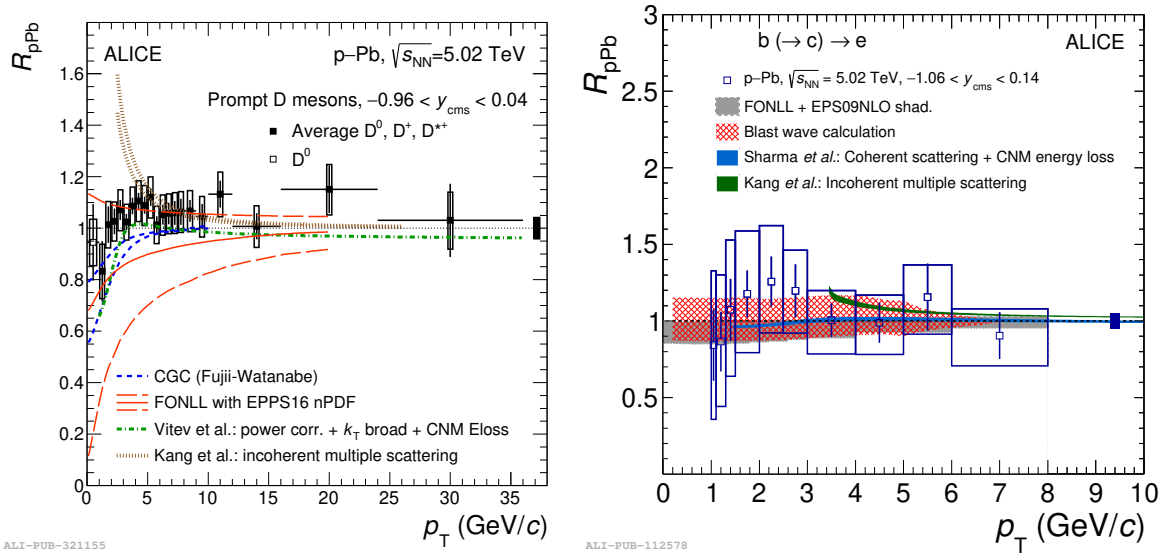

Figure 1.12: The R_{pPb} of D mesons [43] and beauty-decay electrons [45] in $\sqrt{s_{\mathrm{NN}}} =$ 5.02 TeV p-Pb collisions measured with ALICE versus model predictions that include CNM effects.

1.6.2 Energy loss in the QGP and $R_{\rm AA}$

As discussed in Section 1.5, it is expected that the amount of energy lost by quarks as they traverse the QGP depends on their flavor and mass. These expectations of energy loss in the QGP can be tested using the $R_{\rm AA}$ observable. If quarks lose energy in the QGP, their momenta will be shifted to lower values from the energy loss. This would result in an $R_{\rm AA} < 1$, since the p_T-dependent production in heavy-ion collisions would be suppressed with respect to pp collisions. Particles with more suppression due to the QGP medium would have a smaller $R_{\rm AA}$. Thus, it is expected that:

$$\begin{gathered} \Delta E_{gluon} > \Delta E_{u,d,s} > \Delta E_c > \Delta E_b \\ R_{\rm AA}^{u,d,s} < R_{\rm AA}^{c} < R_{\rm AA}^{b} \end{gathered} \tag{1.3}$$

This flavor and mass ordering can be tested by comparing the $R_{\rm AA}$ of light-flavor hadrons (like pions) with heavy-flavor particles. An example is shown in the left panel of Figure 1.13, where $R_{\rm AA}$ of pions and charged particles (largely from light quarks) is compared with the D meson $R_{\rm AA}$ (which contains charm). Both of these measurements were performed with ALICE in head-on Pb-Pb collisions at $\sqrt{s_{\rm NN}} = 5.02$ TeV. It is clear that the D meson $R_{\rm AA}$ is higher than the pion $R_{\rm AA}$ in the range $p_T \lesssim 10$ GeV/c. This supports the hypothesis that light quarks lose more energy in the QGP than charm quarks.

However, due to different production processes for charm and light quarks, the comparison of the two $R_{\rm AA}$ distributions is not straightforward. A better comparison to study the mass-dependence of energy loss is with charm and beauty, since both are produced via the same hard-scattering processes. Such a comparison is shown in the right panel of Figure 1.13. There, the beauty-decay electron (b→e) and heavy-flavor decay electron (c+b→e) $R_{\rm AA}$ measured using the ALICE detector in Pb-Pb collisions at $\sqrt{s_{\rm NN}} = 2.76$ TeV is shown. In the region of overlap between the two measurements ($3 < p_{\rm T} < 8$ GeV/c), the beauty-decay electrons are less suppressed than the electrons from charm- and beauty- decays combined, consistent with the expectation that the beauty quark loses less energy than charm due to its higher mass.

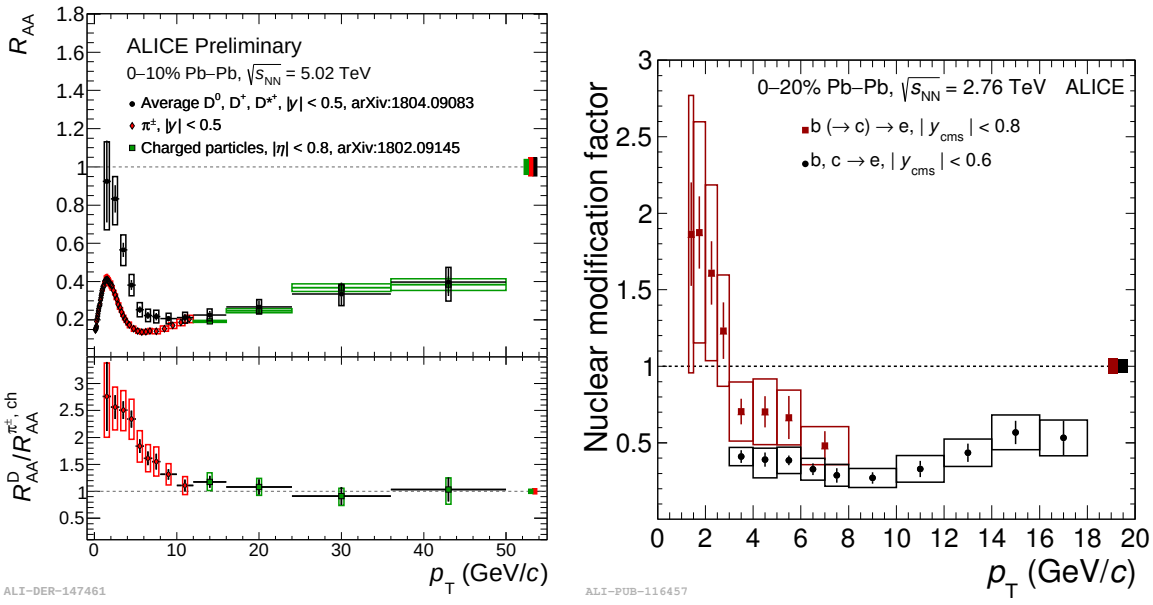

Figure 1.13: Left: The R_{AA} of D mesons (black), pions, (red), and charged particles (green) measured with the ALICE detector in 0-10% Pb-Pb collisions at $\sqrt{s_{\mathrm{NN}}} = 5.02$ TeV [36, 46]. Right: The R_{AA} of beauty-decay electrons (red) and heavy-flavor decay electrons (from both charm and beauty) measured with the ALICE detector in 0-20% Pb-Pb collisions at $\sqrt{s_{\mathrm{NN}}} = 2.76$ TeV [45, 47].

1.6.2.1 Centrality and R_{AA}

Heavy ions are extended objects, and may collide with a non-zero impact parameter b. In other words, heavy-ion collisions can range from being "head-on" to very glancing (see Figure 1.7 for an example of an off-center collision). Head-on collisions have a larger interaction region, forming a larger QGP. Therefore, separating collisions based on their impact parameter would be useful in order to study the effects of different QGP system sizes on experimental observables.

In experiment, it is not possible to directly measure the impact parameter of a given heavy-ion collision. Instead, the collisions are classified according to their "centrality." Centrality is discussed in more detail in Section 2.2.4.1, and is a proxy measurement for the impact parameter. For example, the most head-on collisions with small impact parameters are called "central" collisions and would belong in the 0-10% centrality class. More off-center collisions ("semi-central") would have a higher centrality of around 30-50%. Finally, glancing collisions ("peripheral") would have

very high centralities in the 60-100% range.

The R_{AA} is expected to have a centrality dependence, since the larger QGP formed in more head-on collisions would correspond to an increased path length for particles traversing the QGP. This would lead to increased energy loss and a lower R_{AA}. For example, such a trend is seen in the ALICE measurement of D mesons in Pb-Pb collisions with different centralities (Figure 1.14). The 0-10% measurement of the most head-on collisions has the lowest R_{AA}, while the more peripheral collisions with 60-80% centrality have the highest.

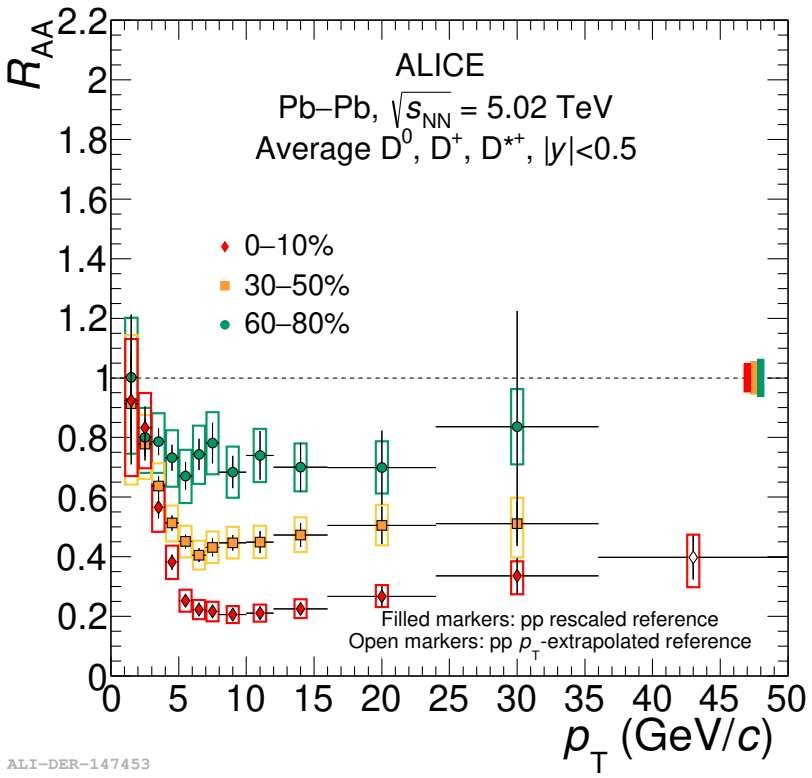

Figure 1.14: The R_{AA} of D mesons measured with the ALICE detector in Pb-Pb collisions with different centralities at $\sqrt{s_{\mathrm{NN}}} = 5.02$ TeV [36].

1.6.2.2 Beauty R_{AA}

Several measurements of the R_{AA} of beauty hadrons and decay particles have been conducted thus far. For example, Figure 1.15 shows the $B^{\pm}$ meson R_{AA} measured by the CMS collaboration in $\sqrt{s_{\mathrm{NN}}} = 5.02$ TeV Pb-Pb collisions [37]. This measurement

includes the full information of the beauty and light quark pair that makes up the $B^{\pm}$ meson, and shows a suppression of about a factor of two.

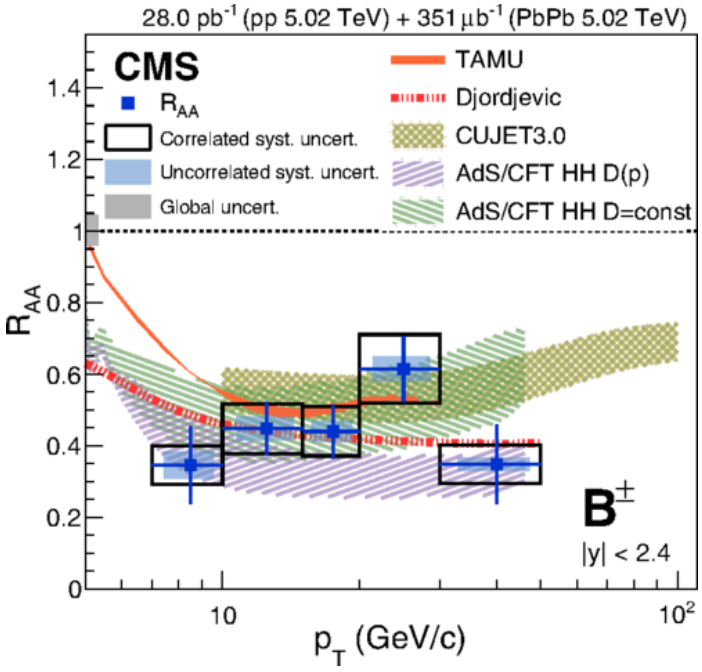

Figure 1.15: Nuclear modification factor of $B^{\pm}$, measured by the CMS collaboration in Pb-Pb collisions [37].

Beauty energy loss in heavy-ion collisions has also been studied via beauty-hadron decay particles. This includes the R_{AA} of non-prompt J/ψ [48, 49], non-prompt D^0 [50], and of electrons from beauty-hadron decays [45, 51, 52]. (Here, "non-prompt" refers to particles produced from beauty hadron decays.) In addition, measurements of muons and electrons from both charm and beauty decays ("heavy-flavor leptons") [47, 53, 54] can give some hint at the energy loss of the beauty quark, though it is combined with information about charm. Each of these measurements show an $R_{\mathrm{AA}} < 1$, compounding the evidence that beauty quarks do indeed lose energy in the QGP. We can further compare these beauty measurements with the R_{AA} of charm-decay particles to see if our expectations of the mass-dependence of energy loss in the QGP are supported. For example, one can compare the R_{AA} of electrons from beauty-hadron decays to that of electrons from both charm- and beauty-decays ("heavy-flavor electrons"). This comparison is shown in Figure 1.13, and was discussed in Section 1.5.

Though the work done thus far to measure the beauty R_{AA} has been extensive, there are still questions that need to be answered and gaps in the current measurements that need to be filled. For example, the CMS measurements of the $B^{\pm}$ meson [37] and non-prompt J/ψ [49] do not extend lower than $p_{\mathrm{T}} \approx 7$ GeV/c. It is important to extend to lower momentum, as we expect the mass-dependence of energy loss to be more apparent in that regime [55].

Measurements of beauty-decay electrons have been performed at low transverse momenta by STAR [51] and PHENIX [52] down to 3 GeV/c and by ALICE down to 1 GeV/c [45]. However, these measurements do not extend to high momentum, stopping at 8 GeV/c. In addition, these beauty-decay electron measurements have not yet been fully studied as a function of centrality; the STAR and PHENIX measurements combined collisions with 0-80% centrality, and the ALICE measurement was only for central collisions with 0-20% centrality.

In this thesis, the measurement of beauty-decay electrons with the ALICE detector will be extended to a transverse momentum of 26 GeV/c. In addition, the measurement will be repeated for collisions with different centralities to see if the nuclear modification factor is affected if we choose more off-center collisions where one expects a smaller QGP medium to be produced. Finally, the measurement will be at a higher center of mass energy per nucleon pair $\sqrt{s_{\mathrm{NN}}}$ than the previous ALICE measurement (5.02 TeV versus 2.76 TeV). This will allow us to build on previous beauty-decay electron measurements and see if the expected trends extend to different momenta, centralities, and collision energies.

1.7 Azimuthal anisotropy

As mentioned briefly in Section 1.6.2.1, off-center collisions are used to understand the effects of varying the QGP size. These collisions are also used to vary the shape of the overlap region between the colliding nuclei. In off-center collisions, this region is almond-shaped as shown in Figure 1.16, introducing spatial anisotropy to the initial conditions of QGP formation. If the matter produced in the overlap region between the two nuclei is a strongly-interacting macroscopic medium, the spatial anisotropy will result in a pressure anisotropy due to the interaction of the medium constituents [56]. The resulting pressure gradient would create a spatial deformation in the dis-

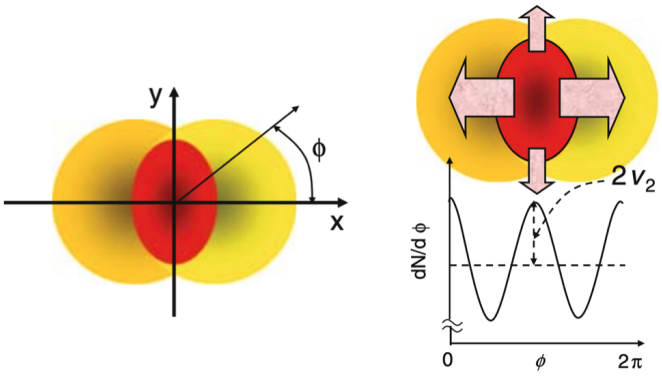

Figure 1.16: Left: Illustration of an off-center collision in the transverse plane. Right: Example azimuthal distribution of particles produced in an off-center collision. Images from [1].

tribution of produced particles; more particles tend to come from the short axis of the almond due to the increased pressure compared to the long axis. This is illustrated on the right in Figure 1.16, where the larger arrows indicate increased particle production along the short axis of the almond.

It is common to measure the azimuthal distribution of produced particles in terms of a Fourier series[2]:

$$\begin{aligned} dN/d\phi &= \frac{N}{2\pi}[1 + 2v_1 cos\phi + 2v_2 cos2\phi + \cdots] \\ v_n &= \langle \cos n(\phi) \rangle \end{aligned} \tag{1.4}$$

where ϕ is the azimuthal angle and v_n are the Fourier coefficients of the harmonics.

The largest coefficient measured in heavy-ion collisions is v_2, or "elliptic flow" [57], which characterizes the ellipticity of the produced particle distribution. Historically, one of the earliest signatures of QGP formation in heavy-ion collisions was the elliptic flow of low-momentum pions ($p_{\mathrm{T}} \lesssim 2$ GeV/c) at RHIC [5, 58]. These pions account for about 95% of the produced particles, and can be assumed to originate from the sea of light particles that principally compose the QGP [58]. The measured v_2 was well-described by hydrodynamic models, which indicated that the material produced

[2]Here, it is assumed that the impact parameter of the collision coincides with the x-axis as in Figure 1.16. If the impact parameter is rotated w.r.t the x-axis by angle Ψ_{RP}, the Fourier coefficients take the form $v_n = \langle \cos n(\phi - \Psi_{\mathrm{RP}}) \rangle$.

in heavy-ion collisions thermalizes at very short time scales (< 1 fm/c), evolves in accordance with the laws of hydrodynamics, and behaves as a perfect fluid with a small shear viscosity close to the quantum limit.

It is also interesting to study the v_2 of heavy-flavor particles, which helps constrain the parameters of theoretical models. For example, model comparisons with the D meson v_2 measured in Pb-Pb collisions with ALICE (Figure 1.17) indicate that the heavy-quark spatial diffusion coefficient D_s near the critical temperature for QGP formation lies in the range $2\pi T D_s = 2 - 4$ (see Ref. [35] for a complete discussion).

Figure 1.17 shows the v_2 of D mesons and beauty-decay electrons measured with the ALICE detector in Pb-Pb collisions at $\sqrt{s_{\rm NN}} = 5.02$ TeV. The D mesons have a non-zero v_2 in the range $2 < p_{\rm T} < 8$ GeV/c, indicating that they participate in the collective behavior of the medium, consistent with the models, despite their large mass [59]. At higher momentum, the positive v_2 is a consequence of the path-length dependence of the charm quark energy loss [60–62]; the particles traveling along the shorter axis of the almond would experience less suppression than those traveling through the long axis.

To understand the interplay of these effects on the beauty quark, the elliptic flow of electrons from beauty-hadron decays was measured in off-center collisions (30-50% centrality) in Pb-Pb collisions at $\sqrt{s_{\rm NN}} = 5.02$ TeV with ALICE [63] (right panel of Figure 1.17). There it was seen that the elliptic flow of the beauty electrons was greater than zero, with a significance of 3.75σ. To help understand the degree to which the non-zero positive v_2 is due to the thermalization of the beauty quark, the measurement was compared with various models. The transport models MC@sHQ+EPOS2, PHSD, and LIDO employ different methods of describing the interactions of beauty quarks with a hydrodynamically expanding medium; all agree with the measurement within experimental uncertainties. The details of these models are discussed in further detail in Section 1.8. The elliptic blast wave model [64], however, agrees with the data for $p_{\rm T} < 2$ GeV/c but then diverges to higher values for higher momentum. The elliptic blast wave model generates momentum spectra assuming the beauty particles radiate from a purely thermal source. In this case, the thermal source was assumed to be elliptic in shape, and the resulting particle production in and out of the reaction plane was compared to generate a prediction for the v_2. This model, unlike the others, treats the beauty quark as if it is fully thermalized with the QGP medium. The electrons shown in this model come mainly

from beauty hadrons below $p_{\mathrm{T}} = 10$ GeV/c, suggesting that the beauty quark does not fully thermalize in this momentum range.

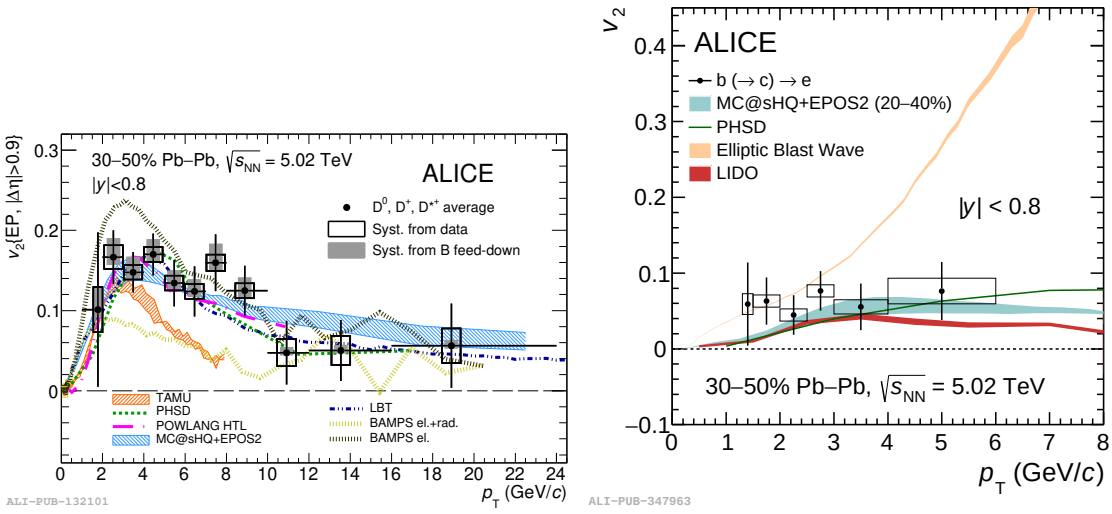

Figure 1.17: The elliptic flow v_2 of D mesons (left) and beauty-decay electrons (right) measured in ALICE in 30-50% Pb-Pb collisions [63, 65].

1.8 Theoretical models

Heavy-ion collisions are complex systems with multiple stages that must be accounted for in theoretical predictions before comparing with data. For instance, one must consider the initial conditions (how to treat the incident partons in the lead atoms), the particle generation mechanisms, the parton interactions, the thermodynamic properties of the QGP, the evolution of the QGP, hadronization mechanisms, and hadron interactions. In light of this, it comes as no surprise that there are multiple theoretical models to generate predictions for heavy-ion collisions. Predictions from the following models are compared with the beauty-decay electron results in Pb-Pb collisions presented in this thesis: Djordjevic [66], PHSD [67], DAB-MOD [68], MC@sHQ+EPOS2 [69], and LIDO [70]. An additional model, FONLL [71, 72], is used to generate predictions for pp collisions.

The PHSD, DAB-MOD, MC@sHQ+EPOS2, and LIDO models are based on heavy-quark transport, i.e. the heavy quarks are embedded in a medium and then

propagated using the Boltzmann or Langevin equations. The medium is generally modeled by a separate framework; in DAB-MOD, MC@sHQ+EPOS2, and LIDO, the QGP medium features a hydrodynamic evolution and is generated on an event-by-event basis to include variations in the initial state. In the case of PHSD, the medium is also modeled on an event-by-event basis using a microscopic dynamical quasiparticle model (DQPM) [73, 74]. These four transport models all include collisional and radiative energy loss with the exception of PHSD, in which the radiative process is suppressed due to the large gluon mass in DQPM [75]. However, the PHSD calculations do not extend higher than $p_{\mathrm{T}} = 17$ GeV/c, where the radiative energy loss is expected to dominate. The PHSD, MC@sHQ+EPOS2, and LIDO models include hadronization via both fragmentation and coalescence (see Section 1.3), while DAB-MOD only includes hadronization via fragmentation in the predictions included in this thesis.

The Djordjevic model is based on pQCD calculations of high-momentum parton energy loss, including both collisional and radiative processes. The QCD medium evolution is modeled using a hydrodynamical 1+1D Bjorken expansion [19], which includes a simple analytical form of temperature dependence. The Djordjevic predictions shown in this thesis are available only for $p_{\mathrm{T}} > 4$ GeV/c because the quark hadronization occurs through fragmentation only. At lower momentum, the coalescence processes are expected to have a greater effect [76].

The table in Figure 1.18 provides an overview of the basic processes considered by each model. A short description of the different models is provided in Sections 1.8.1-1.8.6 along with further references for interested readers. The model comparison of the beauty-decay electron R_{AA} measured in this thesis will be discussed in further detail in Section 5.2.3.

1.8.1 FONLL model

The "Fixed-Order plus Next-to-Leading Log" (FONLL) framework [71, 72] is used to calculate heavy-flavor cross-sections in pp collisions. In FONLL calculations, the perturbative expansion of the cross-section combines terms from a fixed, next-to-leading order approach and a resummation of the next-to-leading logarithm terms (i.e. terms of order $\alpha_{\mathrm{s}}^{\mathrm{n}}\log^{\mathrm{n}}(p_{\mathrm{T}}/m)$ and $\alpha_{\mathrm{s}}^{\mathrm{n}}\log^{\mathrm{n-1}}(p_{\mathrm{T}}/m)$). This perturbative QCD (pQCD) cross-section for heavy quarks is then convoluted with a fragmentation function ($D^{\mathrm{NP}}_{Q\to H_Q}$)

Model	Energy loss		Hadronization		Medium Description
	Collisional	Radiative	Fragmentation	Coalescence	
Djordjevic	✓	✓	✓		Finite-size hydro. medium with *T*-dependence and dynamic scattering centers
PHSD	✓		✓	✓	Dynamical quasiparticle model (no hydrodynamics)
DAB-MOD	✓	✓	✓		Event-by-event viscous hydrodynamic evolution
MC@sHQ+ EPOS2	✓	✓	✓	✓	Event-by-event ideal hydrodynamic evolution
LIDO	✓	✓	✓	✓	Event-by-event viscous hydrodynamic evolution

Figure 1.18: Overview of the theoretical models that provide predictions of beauty-decay electrons in Pb-Pb collisions.

and decay function ($g^{\text{weak}}_{H_Q\to\ell}$) to obtain predictions for leptons from heavy-flavor hadron decays (Equation 1.5). The fragmentation function parameters are determined from e+e- collision data, and the decay functions are also taken from experimental data.

$$d\sigma^{\text{FONLL}}_{\ell} = d\sigma^{\text{FONLL}}_{\text{Q}} \otimes D^{\text{NP}}_{Q\to H_Q} \otimes g^{\text{weak}}_{H_Q\to\ell} \tag{1.5}$$

The uncertainty band includes variations of the renormalization and factorization scales, variations of the heavy quark mass, and the uncertainty from the parton distribution functions.

The FONLL calculations have successfully reproduced many experimental results, including the p_{T}-differential cross section of B^+ mesons measured by CMS in 13 TeV pp collsions [77], and the non-prompt D meson (B→D) spectrum measured by ALICE in 5 TeV pp collisions [78]. It is also in good agreement with ALICE measurements of beauty-decay electrons in pp collisions at 2.76, 5.02, and 7 TeV [79–81]. The 5.02 TeV pp measurement, used in this thesis as a pp reference for the R_{AA}, is compared with FONLL predictions in Figure 1.19. Because of its reliable agreement with pp results, FONLL is used in this analysis to extend the pp reference measurement to higher momenta, where no experimental data is yet available (discussed in further detail in Section 3.7). It is also used to set the initial momentum distributions of heavy quarks in a few of the models detailed in the rest of this section.

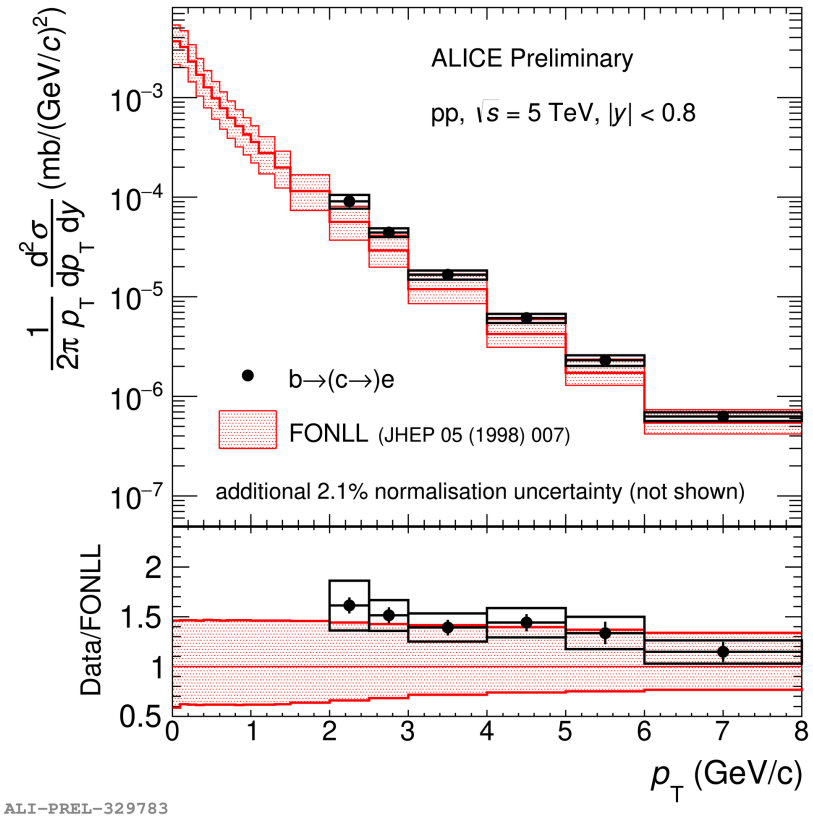

Figure 1.19: The cross section of electrons from beauty-hadron decays measured in ALICE in pp collisions at $\sqrt{s_{\rm NN}} = 5.02$ TeV [80].

1.8.2 Djordjevic model

The "Djordjevic" model, developed by Magdalena Djordjevic and her collaborators [66, 82], is used to describe heavy-flavor $R_{\rm AA}$ in heavy-ion collisions. This framework incorporates a finite-size, dynamical QCD medium with running coupling, and has no free parameters in its model testing. The model uses a pQCD convolution similar to Equation 1.5 to calculate the spectrum of quenched heavy-flavor particles:

$$\frac{E_f d^3\sigma}{dp_f^3} = \frac{E_i d^3\sigma(Q)}{dp_i^3} \otimes P(E_i \to E_f) \otimes D(Q \to H_Q) \otimes f(H_Q \to e) \qquad (1.6)$$

where the subscripts i and f refer to "initial" and "final" respectively. The initial spectrum $\frac{E_i d^3\sigma(Q)}{dp_i^3}$ is extracted from FONLL calculations, and the decay function of hadrons to electrons $f(H_Q \to e)$ is obtained using the same method as FONLL [71,

83]. The KLP fragmentation function [84] is used for the hadronization to B mesons, denoted $D(Q \to H_Q)$. The energy loss probability, $P(E_i \to E_f)$, includes both radiative and collisional energy loss in a finite-size medium with dynamic (i.e. moving) scattering centers. The evolution of the QCD medium is modeled using an ideal hydrodynamical 1+1D Bjorken expansion [19], which includes a simple analytical form of temperature dependence. This is in contrast to some of the other models discussed in this thesis, which use more complex QGP evolution frameworks. However, this model has been successful in predicting heavy-flavor R_{AA} measurements above $p_{\mathrm{T}} = 5$ GeV/c. (See, for example, measurements of D meson R_{AA} in ALICE [36].)

1.8.3 PHSD model

The Parton-Hadron-String Dynamics (PHSD) transport approach [67] can be used for predictions of both R_{AA} and v_2 in heavy-ion collisions. In this approach, the beauty quarks are generated using the PYTHIA event generator [85], tuned such that the beauty quarks' rapidity and transverse momentum distribution matches that of FONLL. The beauty quarks are then elastically scattering (via the relativistic Langevin equation) in the QGP medium, modeled using a dynamical quasiparticle model (DQPM) [73, 74]. In DQPM, the light quarks and gluons are off-shell and have temperature-dependent effective masses and widths given by thermal quantum field theory. The beauty quarks are taken to have fixed mass and no width (on-shell). It was found that including the additional off-shell effect was negligible [86, 87].

With time, the deconfined partonic medium expands and the energy density decreases. Once the local energy density is less than 0.5 GeV/fm^3, the quarks are hadronized either through coalescence or fragmentation. First, all combinations of beauty quarks and light antiquarks (and antibeauty and light quarks) are taken, and the probability of the pairs forming a B or B* meson (via coalescence) is given by

$$f(\boldsymbol{\rho}, \mathbf{k}_\rho) = \frac{8 g_M}{6^2} \exp\left[-\frac{\boldsymbol{\rho}^2}{\delta^2} - \mathbf{k}_\rho^2 \delta^2\right] \tag{1.7}$$

where g_M is the meson's degeneracy and

$$\boldsymbol{\rho} = \frac{1}{\sqrt{2}}(\boldsymbol{r}_1 - \boldsymbol{r}_2), \quad \mathbf{k}_\rho = \sqrt{2}\frac{m_2 \mathbf{k}_1 - m_1 \mathbf{k}_2}{m_1 + m_2} \tag{1.8}$$

with m_i, $\boldsymbol{\rho}_i$, and $\mathbf{k}_i$ being the mass, position, and momentum of the quark or antiquark i. The parameter δ is related to the root mean square of the radius of the produced B meson ($\langle r^2 \rangle = \frac{3}{2}\frac{m_1^2+m_2^2}{m_1+m_2}\delta^2$). Whether the beauty quark then hadronizes via coalescence is decided by Monte Carlo, using the calculated probability. If it is not hadronized via coalescence, the beauty quark instead hadronizes via fragmentation by emitting soft gluons.

Though this model includes energy loss through elastic scattering of the beauty quarks in the QGP as well as hadronic rescattering, it does not take into account radiative energy loss by the beauty quark, which becomes more dominant at high-p_{T}. However, comparisons of PHSD predictions with the D meson R_{AA} measured in 2.76 TeV Pb-Pb collisions in ALICE show that the collisional energy loss alone is sufficient to match data up to $p_{\mathrm{T}} = 15$ GeV/c [88, 89].

1.8.4 DAB-MOD model

The D-And-B MODular simulation code, DAB-MOD [68, 90], embeds heavy-quark energy loss models in event-by-event viscous hydrodynamic backgrounds to study both R_{AA} and v_n of heavy-flavor particles. These backgrounds are generated by v-USPhydro [91] with set viscosity $\eta/s = 0.05$. The initial momentum distribution of the heavy-flavor quarks are set using FONLL calculations, with randomized initial direction. The heavy quarks are then propagated via the relativistic Langevin equation (Brownian motion dynamics) with isotropic diffusion coefficients:

$$d\vec{p} = -\Gamma(\vec{p})\vec{p}dt + \sqrt{dt}\sqrt{\kappa}\vec{\rho} \tag{1.9}$$

Here, Γ is the drag coefficient, κ is the momentum space diffusion coefficient (assumed to be independent of the heavy-quark momentum $\vec{p}$), and $\vec{\rho}$ is the fluctuating force described classically as a white noise. The diffusion coefficients are related by $\kappa = 2E\Gamma T = 2T^2/D$, where D is the spatial diffusion coefficient whose parametrization is taken from Moore and Teaney [92]:

$$D = k_{\mathrm{M\&T}}/(2\pi T) \tag{1.10}$$

where $k_{\mathrm{M\&T}}$ is a free parameter. The heavy quarks are propagated until they reach a cell where the temperature T is less than the decoupling temperature. The decoupling temperature is varied between 120 and 160 MeV to obtain the uncertainty band on the model. Finally, the quarks are hadronized using the Peterson fragmentation function [93]. Though the model has been recently updated to add hadronization via coalescence [90], the results shown here only include hadronization via fragmentation.

1.8.5 MC@sHQ+EPOS2 model

The MC@sHQ+EPOS2 model [69] combines an energy loss model for heavy quarks (MC@sHQ) with EPOS2 [94], which gives the initial conditions of the QGP and describes its further 3+1d ideal hydrodynamical evolution. EPOS2 models the initial hard scatterings of the partons in the colliding nuclei and exchanges of parton ladders as "flux tubes", which break to form quark and anti-quark pairs. This is calculated on an event-by-event basis, giving fluctuating initial conditions for the QGP bulk. The heavy quarks are placed randomly at the original nucleon-nucleon scattering points and in keeping with their p_{T} distribution calculated from FONLL.

The bulk matter extracted from EPOS2 is evolved using a parametrization of the lattice QCD equation of state, while the heavy quarks are propagated using the Boltzmann equation. The heavy quarks scatter with the thermalized partons in the QGP according to the local temperature and velocity fields. The elastic cross-sections are obtained from pQCD matrix elements using the Born approximation and include a running coupling. Once the heavy quarks reach $T_c = 155$ MeV, they hadronize via coalescence (primarily for low-p_T quarks) and fragmentation.

1.8.6 LIDO model

The linearized Boltzmann with diffusion model (LIDO) [70] uses a hybrid approach to describe the interactions of heavy quarks with the QGP medium. The discrete hard scatterings of the heavy quarks with medium partons is described via linearized Boltzmann transport with matrix elements calculated in pQCD. Between the hard scatterings, the Langevin equation with empirically-derived transport coefficients is used to propagate the heavy quarks through the medium. This effectively captures the soft, non-perturbative parts of the interactions. The transport coefficients are

calibrated to D and B meson data at the LHC using a Bayesian analysis [95], which calculates the posterior distribution of the parameters of the model that reproduce the experimental data. This approach takes into account the uncertainties of the experimental measurements.

This transport model is coupled to a 2+1d event-by-event viscous hydrodynamic description of the medium evolution with a lattice equation of state [17, 96]. The initial conditions are also generated on an event-by-event basis using the Reduced Thickness Event-by-event Nuclear Topology model ($\mathrm{T_R}$ENTo) [97]. The heavy quarks themselves are placed according to the $\mathrm{T_R}$ENTo binary collision density (i.e. in "hot spots" of the underlying event), and their initial momenta are sampled from FONLL calculations. At $T_c = 154$ MeV, the heavy quarks are hadronized via fragmentation and coalescence using the ultrarelativistic quantum molecular dynamics model (UrQMD) [98, 99].

Chapter 2: Experimental Set-up

The data in this thesis was collected using the ALICE detector at the LHC. This chapter contains an overview of these facilities and the ALICE apparatus, in some cases summarizing the basic particle and collision information we can gain from the sub-detectors.

2.1 The Large Hadron Collider

The heavy-ion collisions used in this thesis are generated by the Large Hadron Collider (LHC) [100, 101], located on the border of France and Switzerland near Geneva. The LHC is the largest and most powerful particle accelerator in the world, and is part of the accelerator complex at CERN, the European Organization for Nuclear Research. The circular collider is located in underground tunnels, which lie between 50 and 175 meters beneath the surface and have an inner diameter of 3.7 meters. Inside these tunnels are two high-energy particle beams, which travel in opposite directions in two separate beam pipes kept at ultra-high vacuum. Superconducting magnets guide the particles: 1232 dipole magnets bend the beams around the ring, and 392 quadrapole magnets focus the beams. The beams are forced to collide at four intersection points along the accelerator, where different experiments collect data (see Figure 2.1).

The LHC mainly generates three collision systems: proton-proton, proton-lead, and lead-lead collisions. (In 2017, there was also a successful test run of xenon-xenon collisions [103].) The atoms in these collisions are fully stripped of their electrons and accelerated via other accelerators in the CERN complex before being injected into the LHC. At present, the highest center of mass energies achieved for pp collisions is $\sqrt{s} = 13$ TeV, and the highest center of mass per nucleon pair in Pb-Pb collisions has been $\sqrt{s_{\mathrm{NN}}} = 5.02$ TeV.

Seven experiments have taken data at the LHC: ALICE (A Large Ion Collider Experiment) [104], ATLAS (A Toroidal LHC ApparatuS) [105], CMS (Compact Mass Solenoid) [106], LHCb (Large Hadron Collider beauty) [107], LHCf (Large Hadron Collider forward) [108], MoEDAL (Monopole and Exotics Detector At the LHC) [109], and TOTEM (TOTal Elastic and diffractive cross section Measurement) [110].

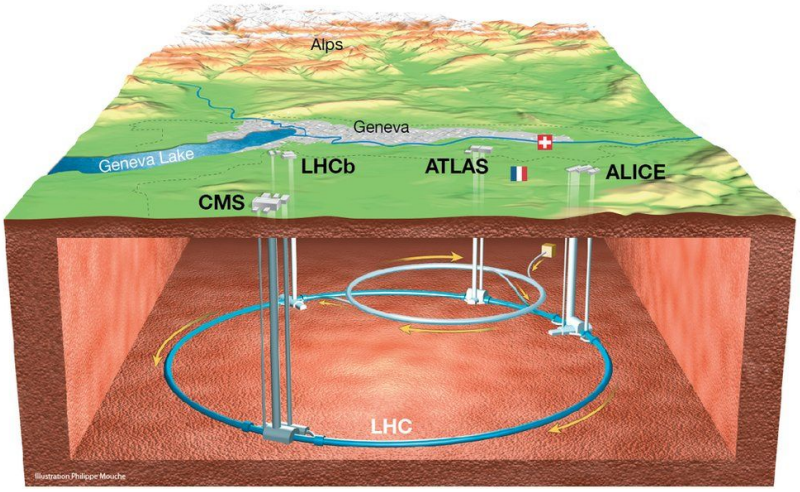

Figure 2.1: Diagram of the LHC. Illustration by Phillipe Mouche, from BBC News [102].

The ALICE detector was used to collect the data in this thesis and will be discussed in greater detail in the next section. The ATLAS and CMS experiments are large, general-purpose detectors that study a wide range of phenomena and are most famous for the discovery of the Higgs boson [111, 112]. LHCb is principally designed to study CP violation through measurements of B mesons at forward rapidity. The other three experiments, LHCf, MoEDAL, and TOTEM, are much smaller collaborations and are dedicated to studying neutral particles at forward rapidity, magnetic monopole searches, and measuring the total pp cross section and elastic and diffractive processes respectively.

2.2 The ALICE Detector

The ALICE (A Large Ion Collider Experiment) detector [104] is designed to address the physics of the strongly interacting QGP created in heavy-ion collisions. It was built by a collaboration of over 1000 people from 105 institutes in 30 different countries, and was completed in time for the first data-taking in 2008. The detector as a whole is approximately $16 \times 16 \times 26$ m^3, weighs about 10,000 tons, and includes 18 different sub-detector systems. A schematic diagram of the detector is given in Figure 2.2, with human figures for scale.

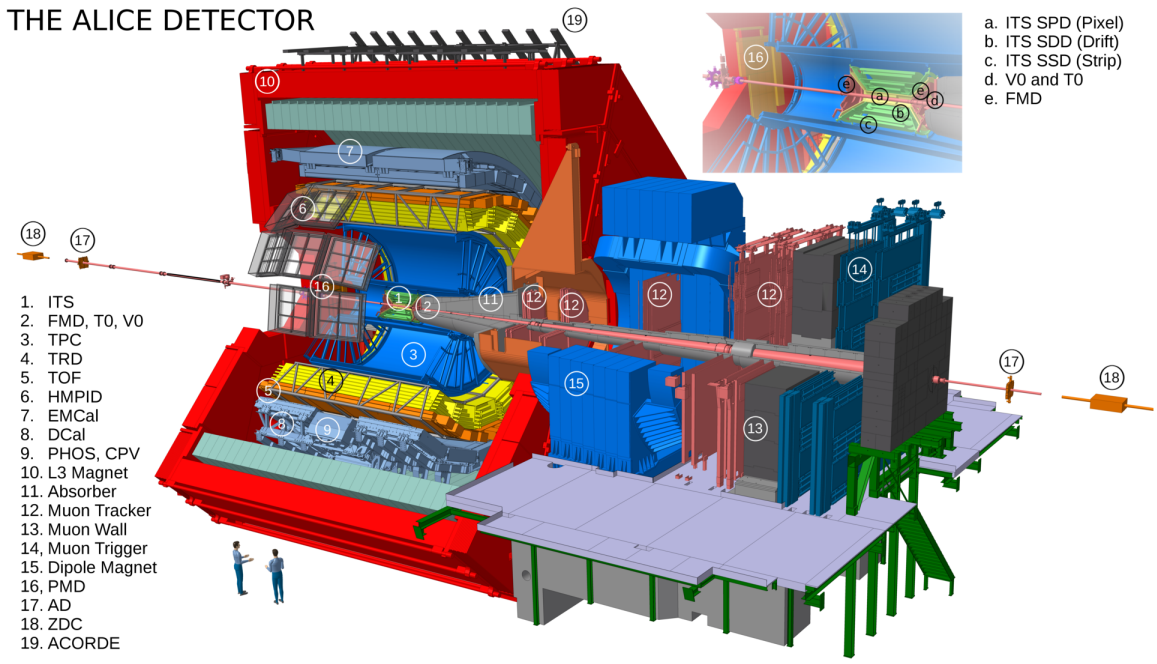

Figure 2.2: Schematic of the ALICE detector. Image from ALICE.

The main design constraint for the ALICE detector was the large multiplicities (particle production) in heavy-ion collisions. To distinguish between different particles, it contains a robust tracking system. The lower interaction rate for Pb beams at the LHC (10 kHz) and the moderate radiation dose of < 3000 Gy allows the use of slower detectors like the Time Projection Chamber (TPC), which offers high-granularity tracking. It is also important for the detector to provide measurements in a wide transverse momentum range. Studies of collective effects require measurements as low as $p_{\mathrm{T}} \sim 10$ MeV/c, while jet physics extend to $p_{\mathrm{T}} > 100$ GeV/c. Thus the detector features low material thickness to minimize rescattering low momentum particles and a large tracking lever arm to increase the resolution of high mometum particles.

The ALICE detector features multiple sub-detectors that employ nearly all the particle identification techniques used in accelerator experiments. This allows reliable identification of photons, muons, hadrons, and electrons. The bulk of these sub-detectors reside in the "central barrel" of the detector, which covers a polar angle of 45°-135°, corresponding to a pseudorapidity range of $|\eta| < 0.9$. The central-barrel detectors are enclosed within a large solenoid magnet recycled from the L3

experiment at LEP with a field strength of 0.5 T. The closest detector to the beam interaction point is the Inner Tracking System (ITS), followed by the Time Projection Chamber (TPC), Transition Radiation Detector (TRD), Time-of-Flight detector (TOF), High-Momentum Particle Identification Detector (HMPID), the Electromagnetic Calorimeter (EMCal), and the PHOton Spectrometer (PHOS). All cover the full azimuth except HMPID and the calorimeters. Outside the L3 magnet is an array of scintillators (ACORDE) that is used to trigger on cosmic rays.

The ITS and TPC are discussed in detail in Sections 2.2.1 and 2.2.2. The TRD [113] is used for electron identification and triggering on high momentum charged particles. It consists of six radial layers of a foam/fiber radiator, drift region, and Xe-CO_2 multi-wire proportional chamber with readout pad. The TOF detector consists of a double-stack of Multigap Resistive Plate Chambers (MRPCs) [114] and is used for particle identification. The HMPID is a ring imaging Cherenkov detector dedicated to identifying high-momentum charged hadrons. Finally, the two calorimeters PHOS and EMCal are used for measurements of photons and electrons respectively. The EMCal is used in this analysis to improve high-momentum electron identification and is discussed in greater detail in Section 2.2.3.

ALICE also has a number of detectors located at small angles along the beam axis: the Zero Degree Calorimeter (ZDC), Photon Multiplicity Detector (PMD), Forward Multiplicity Detector (FMD), and T0 and V0 detectors. They are used for global event characterization and to trigger data-taking. The ZDC measures the spectator protons and neutrons from the incident nuclei that continue to travel along the z-axis after the collision. It includes a neutron detector (ZN) located between the two beam pipes and a proton detector (ZP) placed external to the beam pipe in the direction where the magnetic field tends to deflect positive particles. Both the ZN and ZP include hadronic and electromagnetic sampling calorimeters. The electromagnetic calorimeter is needed to distinguish very glancing collisions (where the spectator nucleons tend to travel down the beam pipe and miss the ZDC) from head-on collisions (where there are very few spectator nucleons). The PMD and FMD measure photons and charged particles respectively at forward rapidity. The PMD consists of a lead and stainless steel converter sandwiched between gas proportional counters, while the FMD is comprised of silicon strip sensors. The Cherenkov counter T0 detector provides the time and position of the collision, providing a start time for the TOF detector and serving as a triggering detector. Finally, the V0 detector,

composed of plastic scintillators, is located on both sides of the collision interaction point (V0A and V0C) and provides trigger information in addition to information about the geometry of the collision (i.e. the centrality). The V0 detector is discussed in greater detail in Section 2.2.4.

In addition to the central-barrel detectors, ALICE also includes a muon spectrometer at forward rapidity $-4.0 < \eta < -2.5$, corresponding to a polar angle of 171°-178°. The spectrometer includes several components: a passive front absorber, a 10-plane tracking system, a large dipole magnet, a passive muon filter wall, 4 trigger chambers, and a shield along the beam pipe. It is used in measurements of quarkonia via the dimuon channel, as well as measurements of muons from heavy-flavor decays.

In the following sections, the specific sub-detectors principally used in this thesis are explained in more detail. The ITS is used for tracking and provides the primary vertex (collision location) resolution needed to perform this analysis. The TPC is also used for tracking as well as electron identification. The EMCal improves electron purity and provides triggering for high energy particles, which extends the momentum reach of the measurement to higher values. Finally, the V0 detector is used to separate heavy-ion collisions with different impact parameters, allowing differential measurements in centrality.

2.2.1 ITS

The Inner Tracking System (ITS) [104, 115] is the closest central barrel detector to the beam pipe. It consists of six concentric cylindrical layers of silicon detectors, ranging from a radius of 3.9 to 43.0 cm from the beam axis (z-axis) and covering a pseudorapidity range of $|\eta| < 0.9$. A schematic of the detector is shown in Figure 2.3. The inner layer lies as close as possible to the beam axis, allowing more precise measurements of the primary vertex (location of the collision) and particle tracks close to the interaction point. The outer layers are pushed to higher radii and closer to the TPC to allow for better track-matching between the two detectors. Since the particle density decreases with increasing radius, the ITS employs different detector technologies in each layer.

The two inner-most layers are made of Silicon Pixel Detectors (SPD), hybrid silicon pixels with a ladder of reverse-biased silicon detector diodes. The SPD layers are located 3.9 cm and 7.6 cm from the beam axis, and are designed to handle

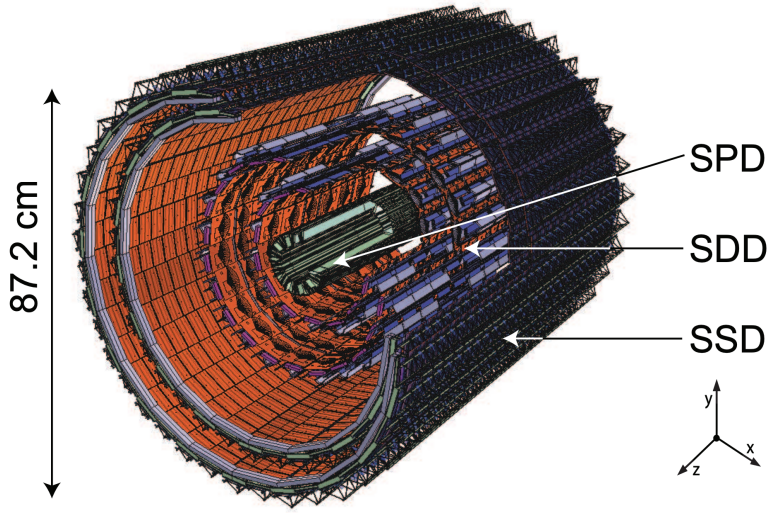

Figure 2.3: Schematic of the Inner Tracking System (ITS) in the ALICE detector. Image from [115].

track densities around 50 particles per cm^2. The middle two layers are Silicon Drift Detectors (SDD), located at r = 15.0 and 23.9 cm from the beam axis where they experience lower particle densities (around 7.2 and 2.5 particles per cm^2 respectively [116]). The SDDs are made with homogenous, high-resistance Neutron Transmutation Doped (NTD) silicon, and are divided into two drift regions by a central cathode strip with a high-voltage bias. The final two layers are double-sided Silicon Strip Detectors (SSD), located at r = 38.0 and 43.0 cm with particle densities around 1/cm^2. Both the SDD and SSD have analog readout, which allows for ionization loss (dE/dx) measurements and identification of low-momentum particles that do not reach the TPC. The resolution of the ITS dE/dx is about 11%.

To aid in measurements of these low-momentum particles, the ITS was designed with minimal material thickness to reduce multiple scattering. The average ITS thickness for a particle traveling in a straight line perpendicular to the beam pipe is only about 7.66% of a radiation length (X_0). Besides the particle identification (PID) and tracking of low-momentum particles, the ITS is also used to determine the primary vertex as well as secondary vertices created by charm and hyperon decays. By extrapolating reconstructed tracks, the primary vertex position is determined with a resolution on the 10 μm level for Pb-Pb collisions and around 110 μm for an average pp event. In tandem with the TPC, it also generally improves particle tracking and

momentum measurements. In particular, it improves the resolution of the distance of closest approach (DCA) of particle tracks to the primary vertex to better than 100 μm. This is important for the studies in this thesis; the DCA is used to separate different sources of electrons, as discussed in Chapter 3.

2.2.2 TPC

The Time Projection Chamber (TPC) is the main central-barrel tracking detector in ALICE [117, 118]. It is cylindrical in shape with a 85 cm inner radius, 250 cm outer radius, and 500 cm length along the beam axis. It covers the full azimuthal angle with the exception of dead zones, and extends in the pseudorapidity range $|\eta| < 0.9$. The TPC is filled with 90 m^3 of a combination of Ne, CO_2, and N_2 gases. When a charged particle passes through the TPC, it ionizes the gas, freeing electrons. An axial electric field of 400 V/cm is applied to the TPC volume by a conducting electrode charged to 100 kV located in the center of the detector. Under the influence of this electric field, the freed electrons drift toward the endplates of the detector with a drift time of $\sim 90\mu$s. These endplates are divided into 18 trapezoidal sectors with multi-wire proportional chambers and two cathode pad readouts. The ionization electron position and time relative to the collision start is recorded by the endplates. With this information, it is possible to reconstruct the path of the original charged particle that passed through the TPC gas. The detector also includes a large cylindrical field cage, isolated from the rest of the experiment by CO_2 filled gaps. This cage minimizes electric field distortions inside the drift volume. A schematic of these components is shown in Figure 2.4.

At the time of design, it was predicted that the charged particle multiplicities generated by the 5.5 TeV Pb-Pb collisions at the LHC could be as high as $dN_{ch}/dy = 8000$. Extensive R&D was needed to account for these multiplicities, which could amount to 20,000 tracks in the TPC acceptance for just one interaction when including secondary particles. To account for this, the TPC features high-granularity with 557,568 separate readout channels. Furthermore, the readout and data-handling was designed to cope with an interaction rate of up to 8 kHz for Pb-Pb collisions, and the specific gas mixture has a high ion mobility to quickly free the drift chamber of positive ions. The gas mixture also discourages multiple scatterings by having a small radiation length.

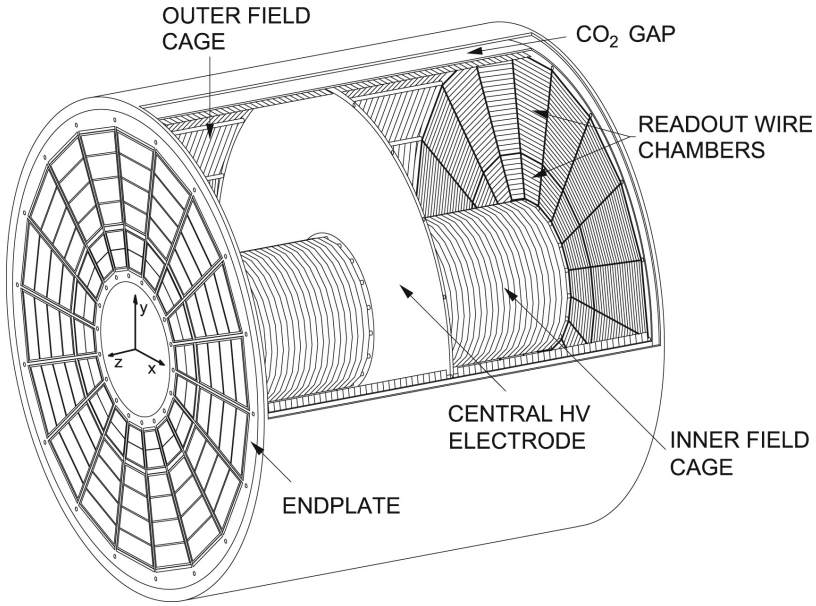

Figure 2.4: Schematic of the Time Projection Chamber (TPC) in the ALICE detector. Image from [117].

With the TPC, we can reconstruct the tracks of charged particles as they pass through the gas of the detector with good two-track separation. Such tracks are shown as lines in Figure 2.7. Since the readout chambers have 159 tangential pad rows, a track can produce up to 159 clusters in the TPC volume. The tracks are reconstructed using a Kalman filter approach [119] using the TPC in conjunction with the ITS. The main steps of this process are as follows [120]:

1. A preliminary primary vertex is found by taking pairs of hits in the first two ITS layers (SPD) and extrapolating them back to the location of the collision.

2. Tracks are "seeded" by taking adjacent clusters in the outer radius of the TPC (where the track density is the smallest) along with the preliminary primary vertex. Tracks are also seeded independently of the preliminary primary vertex by taking three TPC clusters.

3. The track seeds are propagated inward and updated with clusters that fall within a certain proximity range. In some cases, the same physical track can be reconstructed more than once. To avoid this, an algorithm is used to flag

tracks that share a certain number of clusters. The worse track (in terms of number of clusters, for example) is rejected.

4. Once the track has reached the inner radius of the TPC, it is extrapolated to the outer layers of the ITS and propagated inward through the ITS layers, updating with each cluster that falls within a proximity cut. The track is then propagated to its point of closest approach to the preliminary interaction vertex.

5. The tracks are then refitted by the Kalman filter in the outward direction, and an attempt is made to match it to detectors past the TPC (matching to tracklets in the TRD, TOF clusters, and clusters in the EMCal or PHOS calorimeters). The information in detectors past the TPC are not used in the track's kinematic calculations, but any additional information from those detectors is stored in that track's object to aid in particle identification. For example, in this thesis the track's energy lost in the EMCal is used to identify electrons.

6. Finally, all the tracks are propagated inwards again, starting from the outer radius of the TPC. At this point, the track's position, direction, and curvature are set, and the primary vertex is recalculated with these "global" tracks.

Since particles traveling through the central-barrel detectors are exposed to a magnetic field from the L3 magnet, the particle momentum is taken from the curvature of the track. Using information from both the TPC and ITS, the transverse momentum resolution is better than 5% for $2 < p_{\mathrm{T}} < 10$ GeV/c (see Figure 2.5).

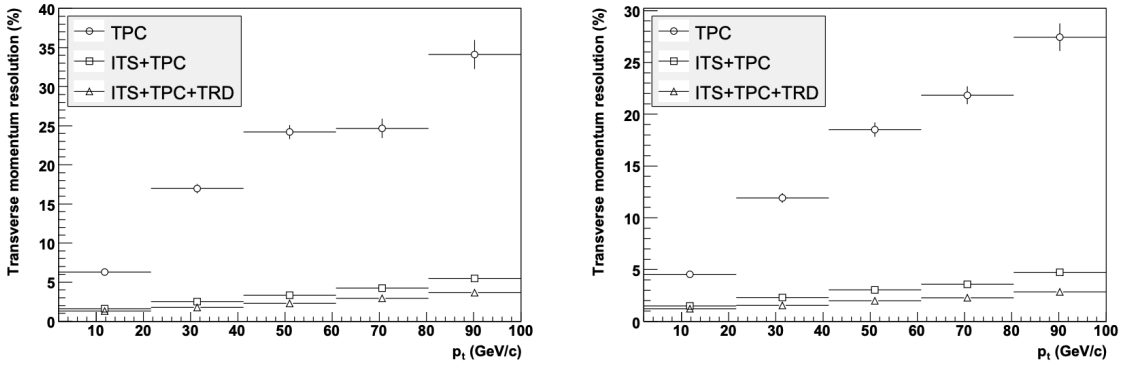

Figure 2.5: Transverse momentum resolution (%) for Pb-Pb collisions with $dN_{\mathrm{ch}}/d\eta = 6000$ (left) and for pp collisions (right). Image from [117].

Finally, the energy loss (dE/dx) in the TPC gas is used in this analysis for particle identification of electrons. Particles of different mass have a characteristic ionization energy loss in a gas, described by the Bethe-Bloch equation. Therefore, the energy loss information in the TPC can be used to isolate different charged particle species. The TPC provides an energy loss resolution of about 5.2% for pp events and 6.5% for central (head-on) Pb-Pb collisions. The use of TPC energy loss is described in more detail in Section 3.3.1, where electron identification is discussed.

2.2.3 EMCal

In this analysis, one of the main detectors used for electron identification is the electromagnetic calorimeter, or EMCal [121, 122]. The EMCal is a sampling calorimeter, with alternating layers of lead and polystyrene scintillator. The EMCal is composed of towers: sandwiches of 76 layers of 1.44 mm Pb and 77 layers of 1.76 mm polystyrene. Each tower measures approximately $6.0 \times 6.0 \times 24.6$ cm^3, and can be read out individually. These towers are grouped into 2×2 groups called modules, the smallest building block of the detector. These modules are further organized into larger supermodules (12×24 modules), each of which weighs about 7.7 metric tons. In total, the EMCal has 10 full-size supermodules and 2 one-third size supermodules, corresponding to 3072 modules and 12,288 towers. It covers a pseudorapidity of $|\eta| < 0.7$ and an azimuthal angle of $\Delta\phi = 107°$. It is located at $r \approx 450$ cm from the beam line, between the space-frame support structure and the L3 magnet coils. See Figure 2.6 for a depiction of the detector components.

The interaction of different particles with the EMCal detector material is determined by the nuclear interaction length (λ_{int}) and the radiation length (X_0). Electron interaction is mostly governed by X_0, while hadron interaction is determined by λ_{int} [125]. The lead absorber in the ALICE EMCal has an effective $X_0 = 12.3$mm (the tower length is $\sim$20 X_0) and a larger λ_{int}, which is approximately equal to the length of the detector towers [120]. As a consequence, electrons are more disposed to interact with the detector material, electromagnetically shower, and lose energy, while hadrons must travel further in the material before they are likely to interact. Unfortunately, the ALICE EMCal detector does not have depth information, so we cannot know how far each particle travels into an EMCal tower before it begins to shower. However, the integrated energy deposited along the length of each tower (cell) can

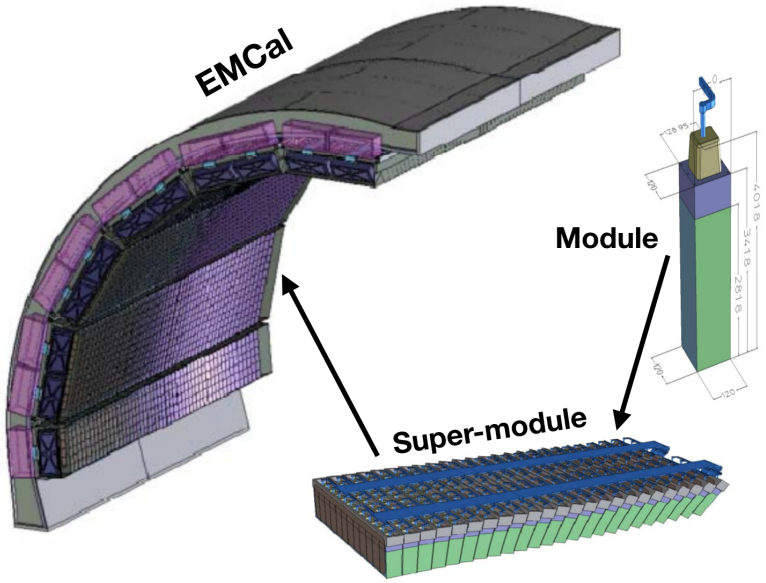

Figure 2.6: A schematic of the components of the EMCal detector. Images taken from [123] and [124].

still be used to help distinguish electrons from hadrons.

Since electrons tend to lose all their energy in the EMCal, the ratio of the electron's energy loss in the EMCal (E) divided by the electron's momentum (p) is

$$E/p = \frac{\sqrt{m^2 + p^2}}{p} \approx \frac{\sqrt{p^2}}{p} = 1 \tag{2.1}$$

for electrons

This is not the case for hadrons, whose E/p ratio would tend to be < 1 since they do not deposit much of their energy in the EMCal. (This can be seen in Figure 3.2.) Thus, we can select particles based on their E/p value to select electrons versus hadrons. The energy resolution of the EMCal is dependent on the energy of the cluster and can be parametrized: $\sigma_E/E = \sqrt{A^2 + \frac{B^2}{E} + \frac{C^2}{E^2}}$ with $A = 1.7 \pm 0.3$, $B = 11.3 \pm 0.5$, and $C = 4.8 \pm 0.8$ with E in units of GeV [122].

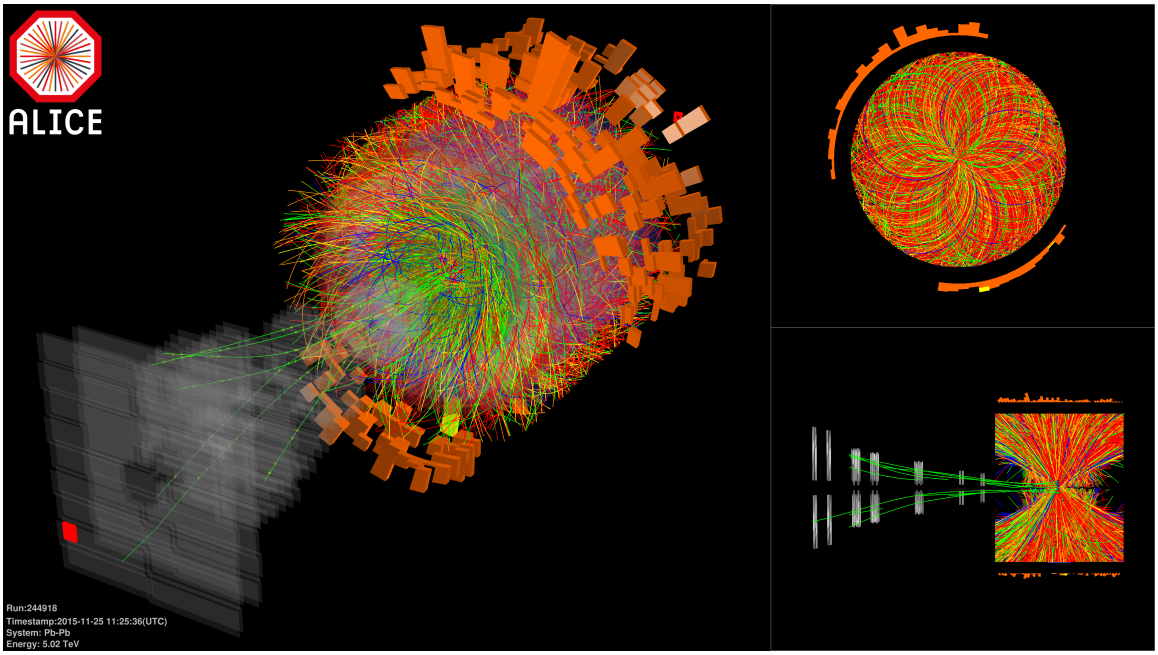

Figure 2.7: A Pb-Pb event display from ALICE. The lines show tracks reconstructed in the TPC and ITS, while the orange blocks show a "heat map" of energy deposited in the towers of the EMCal. Image courtesy of CERN.

2.2.3.1 Clustering and Shower shape

When a particle travels through the EMCal, it may electromagnetically shower and interact with multiple towers/cells. The "spread" of the shower is related to the detector material; the effective Molière radius of the EMCal (i.e. the radius of a cylinder containing 90% of the shower energy) is $R_M = 3.20$ cm. In reconstruction and analysis, the cells included in the shower are combined into a single "cluster" which is then associated with the particle track from the TPC and ITS. This cluster contains the energy distribution left by the particle in the towers (cells) of the EMCal. This analysis uses a V2 clusterizer [126] to create the clusters. This clusterizer loops through the cells until a "seed" cell with a certain threshold energy (500 MeV) is found. The algorithm then loops through the neighboring cells around the seed cell, adding adjacent cells if they meet the minimum energy threshold (100 MeV). The process continues, looking for neighbors of the cells already added to the cluster, until the cells no longer meet the energy requirement. Once a cluster has been found, the clusterizer loops through the remaining cells, looking for a new seed cell.

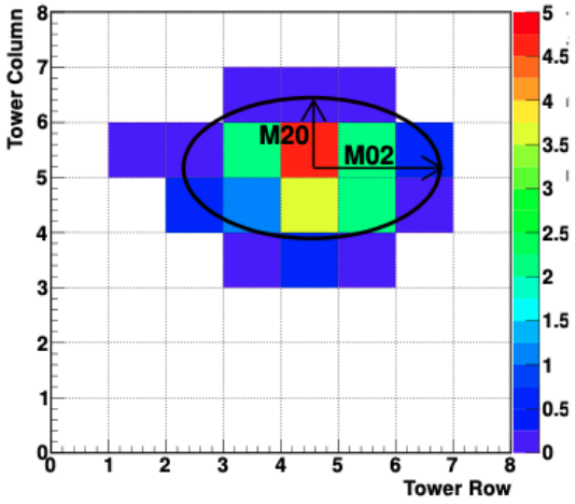

Figure 2.8: An illustration of a cluster in the EMCal and the ellipse parametrization. Image from Tomas Aronsson's thesis [125].

Each cluster is then parametrized by an ellipse, which has a short axis called M20 (or λ_1^2) and a long axis called M02 (or λ_0^2) [125]. See Figure 2.8 for a cartoon example. The method used to get this ellipse is as follows. Each cell in the cluster is given a weight w_i with a logarithmic dependence on the cell's energy. This logarithmic weighting scheme is used because the shower energy tends to decrease exponentially; a linear energy weight would make just one or two cells dominate the calculation (especially considering the large granularity of the ALICE EMCal). The parameter W_0 is a constant, chosen to suppress cells with an energy lower than 1.1% of the total energy of the cluster. For the ALICE EMCal, $W_0 = 4.5$. For a more thorough explanation of this weighting scheme, see [127].

$$w_i = max\left[0, W_0 + ln\left(\frac{E_i}{E_T}\right)\right] \tag{2.2}$$

After applying the energy weighting, the shower dispersion (i.e. the second moment

about the mean shower position coordinate) is calculated in the ϕ and η directions.

$$D_{\eta\eta} = \frac{\Sigma w_i \eta_i^2}{\Sigma w_i} - \left(\frac{\Sigma w_i \eta_i}{\Sigma w_i} \right)^2$$

$$D_{\phi\phi} = \frac{\Sigma w_i \phi_i^2}{\Sigma w_i} - \left(\frac{\Sigma w_i \phi_i}{\Sigma w_i} \right)^2$$

$$D_{\eta\phi} = \frac{\Sigma w_i \eta_i \phi_i}{\Sigma w_i} - \left(\frac{\left(\Sigma w_i \eta_i\right)\left(\Sigma w_i \phi_i\right)}{\left(\Sigma w_i\right)^2} \right)$$

The ellipse axes (M02 and M20) are then defined as follows:

$$M02 = \frac{D_{\eta\eta} + D_{\phi\phi}}{2} + \sqrt{\frac{\left(D_{\eta\eta} - D_{\phi\phi}\right)^2}{4} + D_{\eta\phi}^2}$$

$$M20 = \frac{D_{\eta\eta} + D_{\phi\phi}}{2} - \sqrt{\frac{\left(D_{\eta\eta} - D_{\phi\phi}\right)^2}{4} + D_{\eta\phi}^2}$$

Since electrons and hadrons have different interactions with the EMCal material, their showers in the detector tend to have slightly different short (M20) and long axes (M02) on average. In this thesis, particles with $0.01 < \text{M20} < 0.35$ are selected, which increases the electron purity by about 5-10%. This is shown in Figure 3.3.

2.2.3.2 EG1 Trigger

Finally, the EMCal detector information is used as a "trigger" during data-taking to signal that a particular event should be recorded. In this thesis, the EMCal L1 gamma trigger known as `EG1` [128, 129] was used to select events with high energy depositions in the EMCal detector (which tend to be high-momentum electrons or photons). This is accomplished using a sliding 2x2 window algorithm that sums the analog charge in patches of 4x4 towers. When a certain threshold is met, the information is passed on to a Central Trigger Processor (CTP) [130], which combines trigger information from other detectors (discussed in Section 2.2.4 below). During the Pb-Pb data taking period used in this thesis (`LHC15o`), the analog charge threshold was equivalent to an energy deposition of ~ 10 GeV.

The EG1 trigger increases the recording of events that include high-momentum electrons (> 10 GeV/c), allowing us to measure beauty-decay electrons to higher momentum than previous measurements with ALICE. The previous ALICE R_{AA}

measurement only extended to $p_{\mathrm{T}} = 8$ GeV/c [45]; this thesis measurement reaches 26 GeV/c.

2.2.4 V0 detector

The V0 detector [131] consists of two disks installed on either end of the ALICE collision interaction point (IP) called V0A ($2.8 < \eta < 5.1$) and V0C ($-3.7 < \eta < -1.7$). V0A is on the side opposite of the muon spectrometer, 340 cm away from the IP. V0C is on the front face of the passive absorber of the muon spectrometer, 90 cm from the IP. Each disk consists of 8 segments of plastic scintillator read out by optical fibers.

The V0 detector, like the EMCal, is used for triggering during data-taking. In the data-taking period used in this thesis, it provided what is known as a "minimum bias" (MB) trigger, a loose requirement for selecting events to record. In this case, the MB trigger required the coincidence of a signal above a certain threshold in both the V0A and V0C.

2.2.4.1 Centrality

In Pb-Pb collisions, the two ions are often off-center when they collide, i.e. they have a non-zero impact parameter b, defined as the distance between the centers of the Pb nuclei in the plane transverse to the beam axis. An example of such a collision is shown in Figure 1.7. In such cases, some fraction of the nucleons do not participate in the collision, and continue on down the beam pipe. These are known as "spectators." Their counter-parts are the "participants," the nucleons that experience at least one binary collision with a nucleon in the other Pb ion. The number of spectators and participants are related:

$$N_{spec} = 2A - N_{part} \tag{2.3}$$

where N_{spec} is the number of spectators, N_{part} is the number of participants, and A is the number of nucleons in a Pb ion.

It is interesting (and important) to be able to separate collisions with different b and/or N_{part}, since the volume of the interacting region might have an effect on

our experimental observables. (For example, we might see less energy loss in our R_{AA} measurements since the quarks have less QGP medium to travel through.) It is not possible to directly determine the b or N_{part} in experiment. Instead, collisions are classified according to their *centrality*. The centrality of a collision with impact parameter b can be expressed as a percentile of the total nuclear interaction cross section σ [132]:

$$c = \frac{\int_0^b d\sigma/db'\ db'}{\int_0^\infty d\sigma/db'\ db'} = \frac{1}{\sigma_{\mathrm{AA}}} \int_0^b \frac{d\sigma}{db'}\ db' \tag{2.4}$$

The basic assumption in the experimental determination of centrality is that the impact parameter is monotonically related to the particle multiplicity [39]. In ALICE, the more specific assumption is that the signal amplitude in the V0 (the mean value measured by V0A and V0C) is related to b. For example, a collision with small impact parameter would produce a large number of charged particles, which would translate to a large signal in the V0. Thus, we experimentally determine the centrality as the percentile of the total number of events corresponding to a V0 signal amplitude. This is illustrated by Figure 2.9, where a plot of the V0 signal amplitude is divided into different centrality classes (ranges).

The experimental determination of centrality can be tied to specific values of b, N_{coll}, and N_{part} using a Monte Carlo implementation of the Glauber model [134–136]. The Glauber model [39] is a geometric model that treats a heavy-ion collision as the sum of the binary nucleon-nucleon scatterings in the overlap region of the incoming heavy ions. The Monte Carlo implementation can be described in three main steps. First, the nucleon positions in the lead ions are randomly set based on the nuclear density function, measured in electron-nucleus experiments [137]. The ions are then collided, modeled as a series of independent binary nucleon-nucleon collisions with an inelastic nucleon-nucleon cross section extracted from pp collision data. Finally, the result is coupled to a simple particle production model that uses a negative binomial distribution (NBD) for the charged particle multiplicity. The final result is fitted to the V0 data (see Figure 2.9), and a direct comparison between the model and data can be made to infer, for example, the N_{part} in a given centrality range. For example, in Pb-Pb collisions at $\sqrt{s_{\mathrm{NN}}} = 5.02$ TeV, the 0-10% collision class (head-on collisions) corresponds to $\langle N_{part} \rangle = 357.3$, with an RMS of 32.1 and a systematic uncertainty of

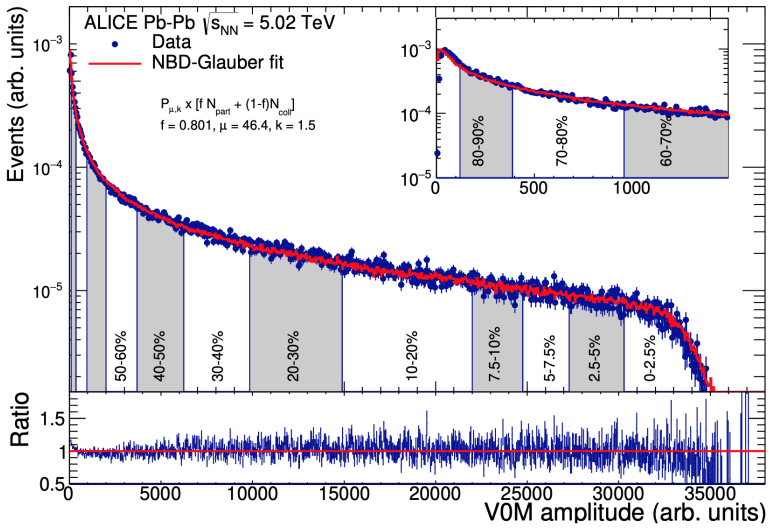

Figure 2.9: The V0 signal amplitude in Pb-Pb collisions at $\sqrt{s_{\rm NN}} = 2.76$ TeV measured with ALICE, divided into centrality classes. Image from [133].

0.753 [133]. In the 30-50% class, $\langle N_{part} \rangle = 109$, with an RMS of 26.6 and a systematic uncertainty of 1.11 [133].

The centrality resolution is 0.5% in central collisions (near 0% centrality), and increases to 2% in peripheral collisions (around 60-80% centrality) [132].

Chapter 3: Analysis Details

In this chapter, the analysis procedure used to measure the beauty-decay electron yield is laid out in detail. The general strategy is as follows. First, quality collision events and tracks are selected in the data sample. Among these tracks, electrons are identified using information from the TPC and EMCal detectors. Any remaining hadron contamination is estimated and removed using a data-driven procedure. This leaves us with a high-purity electron sample.

Next, the beauty-decay electrons must be separated from electrons from other sources. In the momentum range considered in this thesis, the other main sources of electrons are charm hadron decays, Dalitz decays of light neutral mesons (π^0 and η), and photon conversions in the detector material. The electrons from the latter two sources, "photonic electrons," are identified and removed using an invariant mass procedure. After photonic electrons are subtracted, the remaining electrons are from charm and beauty hadron decays. To differentiate between the two sources, we take advantage of the fact that beauty hadrons have a longer lifetime than charm hadrons. This causes the electrons from beauty hadron decays to have a larger distance-of-closest-approach (DCA) to the primary vertex. The DCA distribution of the heavy-flavor electrons is fitted with two templates, one for charm-decay electrons and one for beauty-decay electrons. From the fit, the yield of beauty-decay electrons is extracted.

Each of these steps is laid out in further detail in the following sections. The first two sections describe the requirements used to select the proper events and particle tracks reconstructed in the ALICE detector. In Section 3.3, the procedure for identifying electron tracks and the data-driven methods used to obtain a sample of heavy-flavor electrons are described in detail. Section 3.4 includes the template fit procedure used to separate charm- and beauty-decay electrons. Finally, Section 3.5 details the efficiency corrections needed to obtain the fully-corrected beauty-decay electron yield, and Section 3.7 gives details about the pp reference used to calculate the R_{AA}. This basic procedure was repeated and conducted separately for collisions with 0-10% and 30-50% centrality.

3.1 Dataset and Event selection

The measurement of beauty-decay electrons in this thesis was performed in Pb-Pb collisions at $\sqrt{s_{\rm NN}}$ = 5.02 TeV. The data was recorded by the ALICE detector in 2015 (known as the `LHC15o` dataset).

Within this dataset, the events were recorded using a minimum bias and EG1 EMCal trigger. Details of these two triggering systems are included in Sections 2.2.3.2 and 2.2.4. The EG1 trigger selects events that include a large energy deposition in the EMCal > 10 GeV. Since these energy depositions are produced by the electromagnetic showers of high-energy electrons, the EG1 trigger improves the statistics of electrons at high-momentum.

To select "good" physics events, additional requirements were imposed on the events in the data sample. Events caused by interactions between the accelerated lead ions and the beam gas were removed. The primary vertex of the collision events were required to be centered within the ALICE detector (i.e. primary vertex with a z-axis position $|{\rm Vtx_z}| < 10$ cm).

The number of minimum bias (EMCal-triggered) events passing these selection cuts is 4.84×10^6 (5.80×10^5) for 0-10% central Pb-Pb events. For the 30-50% centrality class, the number of minimum bias events is 9.5×10^6 and the number of EG1 events is 3.0×10^5.

3.1.1 Monte-Carlo sample

Monte Carlo (MC) simulations are used to calculate the efficiency of selecting photonic electrons using an invariant mass method (see Section 3.3.3.2), to estimate the overall reconstruction efficiency of beauty-decay electrons (Section 3.5), and to make the distance-of-closest approach (d_0 or DCA) templates used to separate charm- and beauty-decay electrons (Section 3.4). The Monte Carlo samples were produced using Hijing [138], a MC event generator. This generator combines a pQCD-based model of jet production with a Lund-type model of soft interactions, and accounts for nuclear shadowing and energy-loss processes of partons traveling through the produced medium. Additional heavy-flavor electron decays were generated with Pythia 6 with Perugia tune 2011 (350) [139] and embedded in the sample. The number of π^0 and η particles in the sample was increased to improve statistics for the photonic elec-

tron tagging efficiency calculation. The specific response of the ALICE detector was implemented using GEANT 3 [140].

Two separate MC productions were used in this thesis: `LHC16i3a` was used for 0-10% central collisions and `LHC16i3b` was used for 30-50%. The number of simulated events passing the selection cuts was 3.0×10^5 (3.7×10^5) for 0-10% (30-50%) collisions.

3.2 Track selection

As discussed in Section 2.2.2, particle tracks are reconstructed using the TPC and ITS detectors. To ensure that the tracks used in this analysis are of good quality, several selection criteria were required, and are listed in Table 3.1. For example, a track is required to cross a certain number of rows and generate a certain number of clusters in the TPC. This aids the track-finding algorithm and ensures good resolution and a proper fit to the TPC clusters. Another notable example is the requirement that the track includes at least one "hit" in the SPD (the first two layers of the ITS). This requirement helps reject electrons that are produced deeper in the detector material via photon conversion processes.

In addition to these requirements, the particle tracks are required to "match" with an EMCal cluster. In other words, when the particle track is extrapolated to the EMCal detector, it must align with an EMCal cluster so that the energy deposit information of the particle can be obtained. The difference in both ϕ and η between the track and EMCal cluster are required to be < 0.05 to ensure good cluster-track matching.

3.3 Heavy-flavor electron identification

3.3.1 Electron identification

After applying the track selection cuts, the electrons must be separated from other charged particles in the sample like pions, protons, and kaons. This is done using information from both the TPC and EMCal detectors.

As discussed in Section 2.2.2, particles ionize the TPC gas and lose energy as they travel through the detector. Different particle species have a characteristic mean

Table 3.1: Track selection cuts

Track property	Cut applied
Minimum Number of Crossed Rows in the TPC	70
Minimum No. of Crossed Rows / Findable Clusters in TPC	0.8
Maximum χ^2 per TPC cluster	4
Minimum number of TPC clusters	80
Minimum number of ITS cluster	3
Reject kink candidates	On
ITS and TPC refit	On
Hit on SPD layer	1 hit on any layer
Maximum χ^2 per ITS cluster	36
Maximum DCA_{xy}	0.25 cm
Maximum DCA_{z}	1 cm
Track η	$\lvert\eta\rvert < 0.6$

energy loss in the TPC ($\langle \mathrm{d}E/\mathrm{d}x \rangle_{\mathrm{TPC}}$) that can be described by a parametrization of the Bethe-Bloch equation (Equation 3.1):

$$f(\beta\gamma) = \frac{P_1}{\beta^{P_4}} \left(P_2 - \beta^{P_4} - \ln(P_3 + \frac{1}{(\beta\gamma)^{P_5}}) \right) \tag{3.1}$$

where β is the velocity of the particle, γ the Lorentz factor, and P_i are the fit parameters. This parametrization was originally proposed by the ALEPH experiment [141]. Examples of $\langle \mathrm{d}E/\mathrm{d}x \rangle_{\mathrm{TPC}}$ for different particle species can be found in Figure 3.1, where they are plotted as a function of momentum and compared to data. It is clear in this image that the electron signal lies near its expected $\langle \mathrm{d}E/\mathrm{d}x \rangle_{\mathrm{TPC}}$ curve. We select these particles using the variable $\mathrm{n}\sigma_{\mathrm{TPC-dE/dx}}$, the difference between the measured and expected energy loss in terms of the energy loss resolution (Equation 3.2). In this analysis, an asymmetric cut of $-1 < \mathrm{n}\sigma_{\mathrm{TPC-dE/dx}} < 3$ is applied. This is to reduce contamination from pions, whose $\langle \mathrm{d}E/\mathrm{d}x \rangle_{\mathrm{TPC}}$ begins to encroach on the electron signal as the momentum increases.

$$\mathrm{n}\sigma_{\mathrm{TPC-dE/dx}} = \frac{\langle \mathrm{d}E/\mathrm{d}x \rangle_{\mathrm{TPC}}^{\mathrm{measured}} - \langle \mathrm{d}E/\mathrm{d}x \rangle_{\mathrm{TPC}}^{\mathrm{expected}}}{\sigma_{\mathrm{TPC}}^{\mathrm{res}}} \tag{3.2}$$

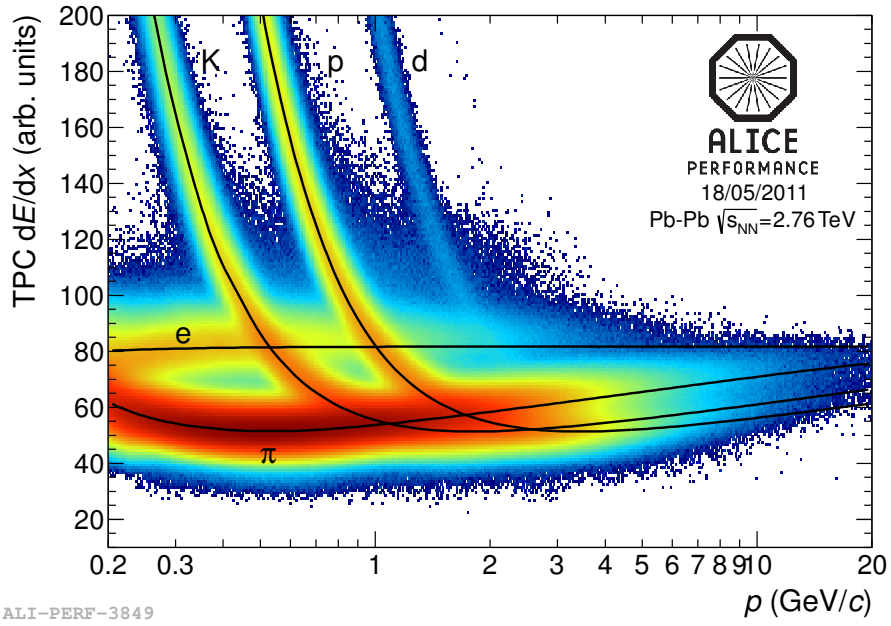

Figure 3.1: ALICE performance plot showing energy loss in the TPC as a function of momentum. Note different particle species follow characteristic curves described by a Bethe-Bloch parametrization.

After applying the $n\sigma_{\mathrm{TPC-dE/dx}}$ selection, the electron purity of the sample is further improved by using information from the EMCal detector. Because electrons have a relatively low mass (511 keV) compared to their momentum (> 3 GeV/c for this analysis), we expect that their energy divided by their momentum will be close to unity:

$$E/p = \frac{\sqrt{m^2 + p^2}}{p} \approx \frac{\sqrt{p^2}}{p} = 1 \quad \text{for electrons} \tag{3.3}$$

The EMCal detector has a small radiation length, so, by design, electrons tend to interact with the detector material and lose all of their energy via electromagnetic shower (see Section 2.2.3). Therefore, we can use the particle energy loss in the EMCal as the total energy. In Figure 3.2, the ratio of the energy lost in the EMCal over the track momentum is plotted, revealing a clear electron peak around unity. Thus, we only select particles which satisfy the requirement that $0.8 < E/p < 1.2$.

The remaining non-electron contamination, mostly from pions, has a small E/p, since the EMCal captures only a fraction of their energy. (Recall that the EMCal material has a large nuclear interaction length, discouraging hadronic interaction and energy loss.) However, as can be seen in Figure 3.2, the distinction between the electron signal and hadron background is less clear as one goes to higher transverse momentum. As a result, the purity of the electron sample begins to suffer at high momenta, because both the $n\sigma_{\mathrm{TPC-dE/dx}}$ and E/p criteria are less effective in distinguishing electrons and hadrons.

Fortunately, one can compensate for some of the loss in purity at high momentum by applying an additional requirement on the shape of the electromagnetic shower in the EMCal. As mentioned in Section 2.2.3.1, the electromagnetic showers in the EMCal are described by an ellipse with short axis M20 and long axis M02. After the $n\sigma_{\mathrm{TPC-dE/dx}}$ and E/p selections, we require that the shower produced by the electron candidates have a short axis M20 between 0.01 and 0.35. The M20 selection improves the electron purity by ∼5-10%, depending on the p_{T} and centrality. This can be seen in Figure 3.3, where the electron purity of the sample has been calculated with and without the M20 selection applied. The purity was obtained by estimating the remaining hadron contamination as detailed in Section 3.3.2. Further discussion of the EMCal shower shape can be found in Section 2.2.3.1.

Table 3.2: Electron identification (eID) cuts

Track property	Cut applied
Energy deposited in EMCAL/momentum	$0.8 < E/p < 1.2$
Sigma of electron energy loss in TPC	$-1 < n\sigma_{\mathrm{TPC-dE/dx}} < 3$
Shower shape, short axis	$0.01 < \mathrm{M20} < 0.35$

3.3.2 Removing hadron contamination

After applying the electron identification cuts, some hadrons remain in the sample. This contamination is estimated and removed from the electron candidates using a data-driven method.

First, a sample of hadrons is obtained using the selections $n\sigma_{\mathrm{TPC-dE/dx}} < -4$ and $0.01 < M20 < 0.35$ m. The E/p distribution of these hadrons is then scaled to match the electron candidate E/p distribution at low E/p, where the majority of particles

are hadrons. An example of this can be seen in Figure 3.2, where the red hadron E/p distribution has been scaled to match the black electron candidate E/p. The exact region of scaling varies with p_{T}, since the hadron contamination peak moves to higher E/p as the p_{T} increases (also seen in Figure 3.2). The scaling region for $10 < p_{\mathrm{T}} < 12$ GeV/c and $p_{\mathrm{T}} > 14$ GeV/c in 30-50% centrality is slightly larger to compensate for lower statistics; the larger range ensures that statistical fluctuations do not have an undue influence on the scaling. The scaling regions are listed in Table 3.3.

Table 3.3: E/p scaling region for hadron contamination estimation

p_{T} (GeV/c)	0-10%	30-50%
< 8	$0.2 < E/p < 0.4$	$0.2 < E/p < 0.4$
$8 - 10$	$0.2 < E/p < 0.4$	$0.4 < E/p < 0.6$
$10 - 12$	$0.4 < E/p < 0.6$	$0.2 < E/p < 0.6$
$12 - 14$	$0.4 < E/p < 0.6$	$0.4 < E/p < 0.6$
> 14	$0.4 < E/p < 0.6$	$0.5 < E/p < 0.7$

Once this is done, the amount of hadron contamination (N_{hadrons}) is estimated by taking the integral of the scaled hadron E/p distribution in the region $0.8 < E/p < 1.2$. For the future steps in the analysis, the distance of closest approach (DCA) of the electrons to the primary vertex is needed. To subtract the hadron contamination from the DCA distribution, we first obtain the hadron DCA by applying the selection $\mathrm{n}\sigma_{\mathrm{TPC-dE/dx}} < -4$. The DCA distribution of these hadrons is then scaled to N_{hadrons} and can subtracted from the DCA of the electron candidates. Figure 3.4 shows the DCA distribution of the electron candidates in black and the estimated hadron DCA after scaling in red. In this plot and throughout this thesis, the DCA is shown after being multiplied by the sign of the charge of the particle and the sign of the magnetic field provided by the L3 magnet.

3.3.3 Non-HF electron background subtraction

Once the hadron contamination is removed, we are left with a sample of electrons from a number of sources. These include [53]:

1. heavy-flavor hadron decays (from charm and beauty)
2. Dalitz decays of light neutral mesons (π^0 and η) and photon conversions in the detector material

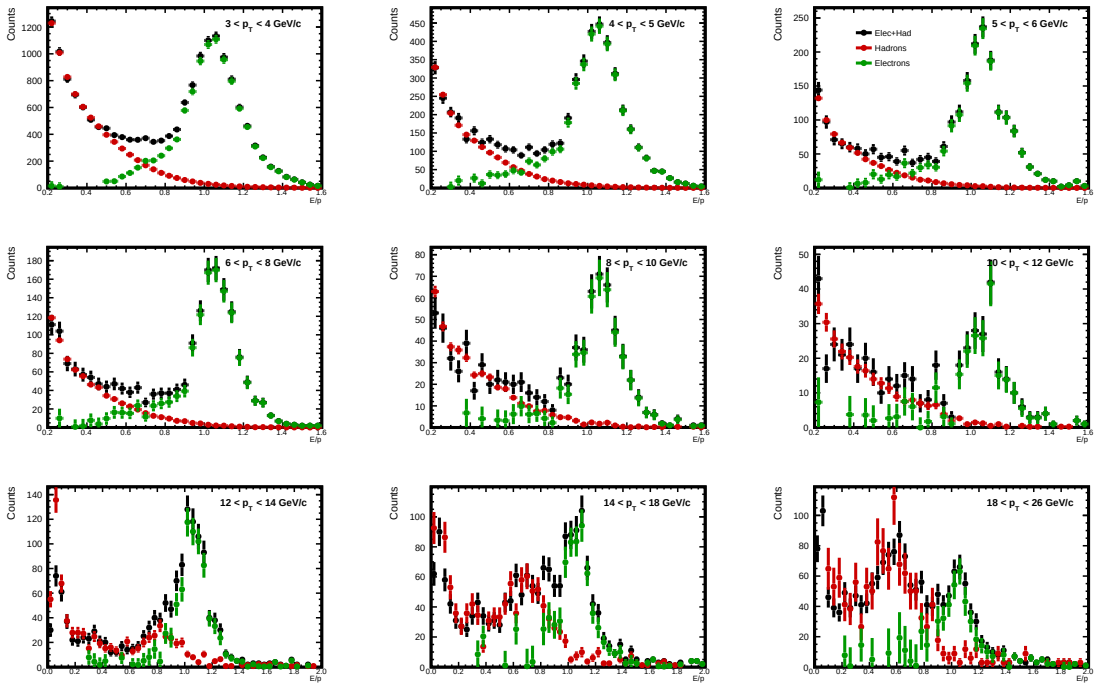

Figure 3.2: The E/p distributions after electron identification selections (black), shown in different momentum ranges. The estimated hadron contamination is shown in red. The green distribution shows the electron signal after the hadron contamination has been subtracted. The data shown here is from 0-10% collisions.

3. dielectron decays of quarkonia (J/ψ and Υ)

4. weak decays of kaons: $K^{0/\pm} \rightarrow e^{\pm}\pi^{\mp/0}\overline{\nu}_e$ (K_{e3} decays)

5. dielectron decays of light vector mesons (ω, η', ϕ)

6. W and Z/γ^* decays

The particles of interest in this thesis, beauty-decay electrons, belong in the first category along with electrons from charm-hadron decays. Charm- and beauty-decay electrons are separated using their DCA, as explained later on in Section 3.4. However, before that step in the analysis, we must first remove or account for the electrons from sources 2-6.

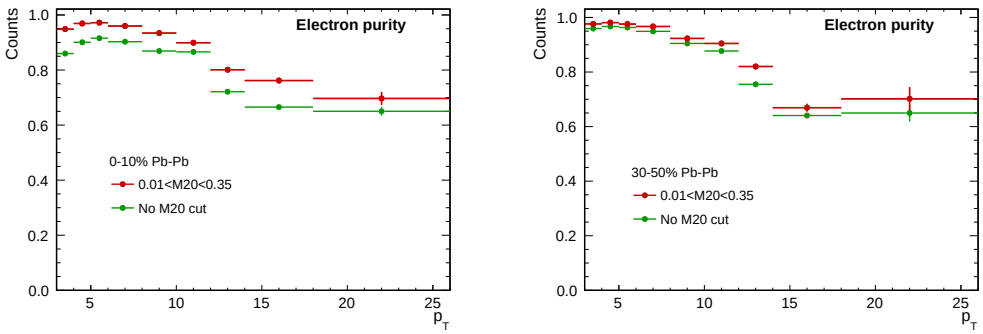

Figure 3.3: The estimated purity of the electron sample with all eID cuts (red) compared to the purity without the M20 cut (green). The left plot shows the results for 0-10% centrality, while the right shows the results for 30-50%.

3.3.3.1 Photonic electrons

The largest source of non-heavy-flavor background electrons are Dalitz decays and photonic conversions in the detector material. In this thesis, the electrons from such decays are referred to as "photonic electrons." Photonic electrons are produced in electron-positron pairs with a small opening angle. Because their mother particles have small masses ($M_\gamma = 0$ and $M_{\pi^0} = 0.135$ GeV/c^2), the electron-positron pairs from these sources will have a small invariant mass (Equation 3.4) with a peak near zero (Figure 3.5). This property can be used to "tag" and remove photonic electrons.

$$M_{e1e2} = \sqrt{(E_1 + E_2)^2 - (p_1 + p_2)^2} \tag{3.4}$$

The procedure used to tag photonic electrons is as follows. First, the DCA distribution of electrons that form electron-positron (unlike-sign) pairs with small invariant mass (< 0.1 GeV/c^2) is obtained. To eliminate combinatorial background, the DCA of electrons that form like-sign pairs with invariant mass < 0.1 MeV is then subtracted from this distribution (see Figure 3.6). Both the like-sign and unlike-sign electron pairs are obtained by taking the electrons passing the electron selection criteria and matching them with electrons that pass the less-strict criteria listed in Table 3.4. The looser criteria is to improve the efficiency of finding the partner electron.

After applying the photonic electron tagging efficiency (see Section 3.3.3.2), the photonic electron DCA is subtracted from the inclusive electron DCA to get the heavy-flavor decay electron DCA.

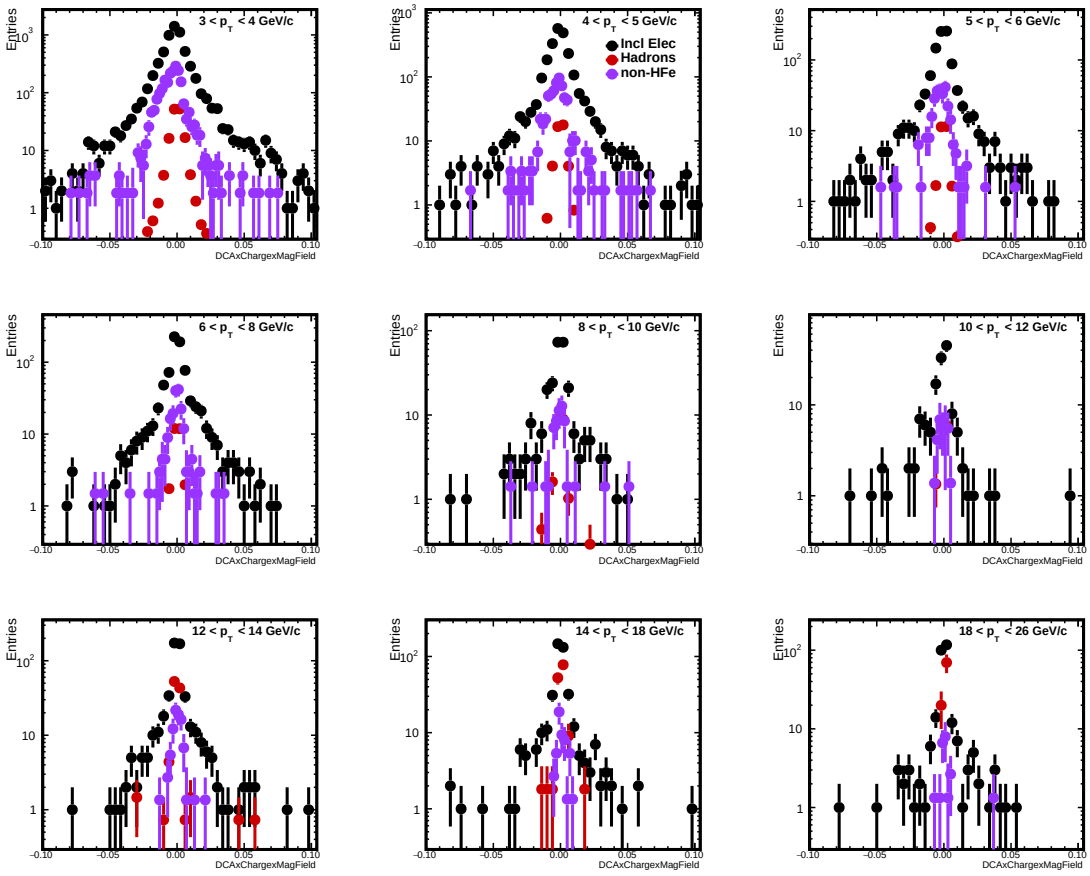

Figure 3.4: The DCA of electron candidates (black), the estimated hadron contamination (red), and the photonic electrons (purple) in 30-50% centrality.

Table 3.4: Partner electron requirements

Track property	Cut applied
Min number of TPC clusters	80
Maximum χ^2 per TPC cluster	4
Reject kink candidates	yes
Maximum $\mathrm{DCA_{xy}}$	0.25 cm
Maximum $\mathrm{DCA_z}$	1 cm
Min p_{T} (GeV/c)	0.3
Pseudorapidity	$-0.9 < \eta < 0.9$
Sigma of electron energy loss in TPC	$-3 < n\sigma_{\mathrm{TPC-dE/dx}} < 3$

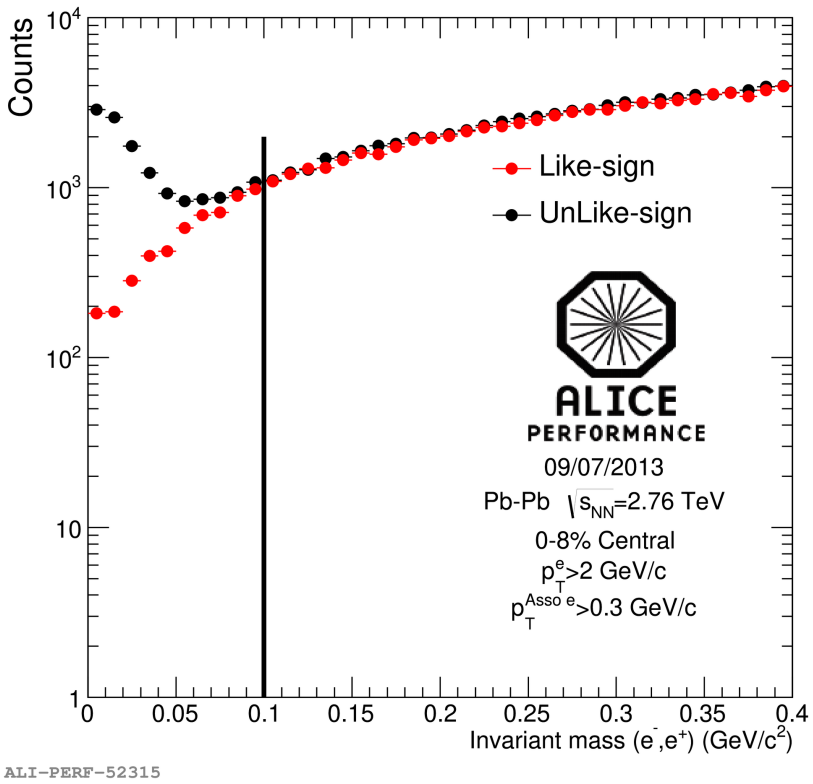

Figure 3.5: Invariant mass of electron pairs in 2.76 TeV Pb-Pb collisions measured with ALICE.

3.3.3.2 Photonic electron tagging efficiency

The invariant mass analysis to identify photonic electrons is not completely efficient. Our detectors only cover a limited area, and we reject some electron-positron pairs due to the partner electron selection requirements. Therefore, we must apply a reconstruction or "tagging" efficiency before the photonic electron DCA can be subtracted from the inclusive electron DCA. This photonic electron tagging efficiency is calculated using MC simulations; within the simulation, the same invariant mass analysis is performed to identify photonic electrons. The efficiency is then just the ratio of these "tagged" photonic electrons to the true number of photonic electrons generated in the MC sample that pass the basic track quality selections.

As mentioned in Section 3.1.1, the MC sample includes enhanced η and π_0 production. This means that each MC event is enriched with additional (embedded) η and π_0 mesons. These added η and π_0 mesons improve the statistics of the efficiency

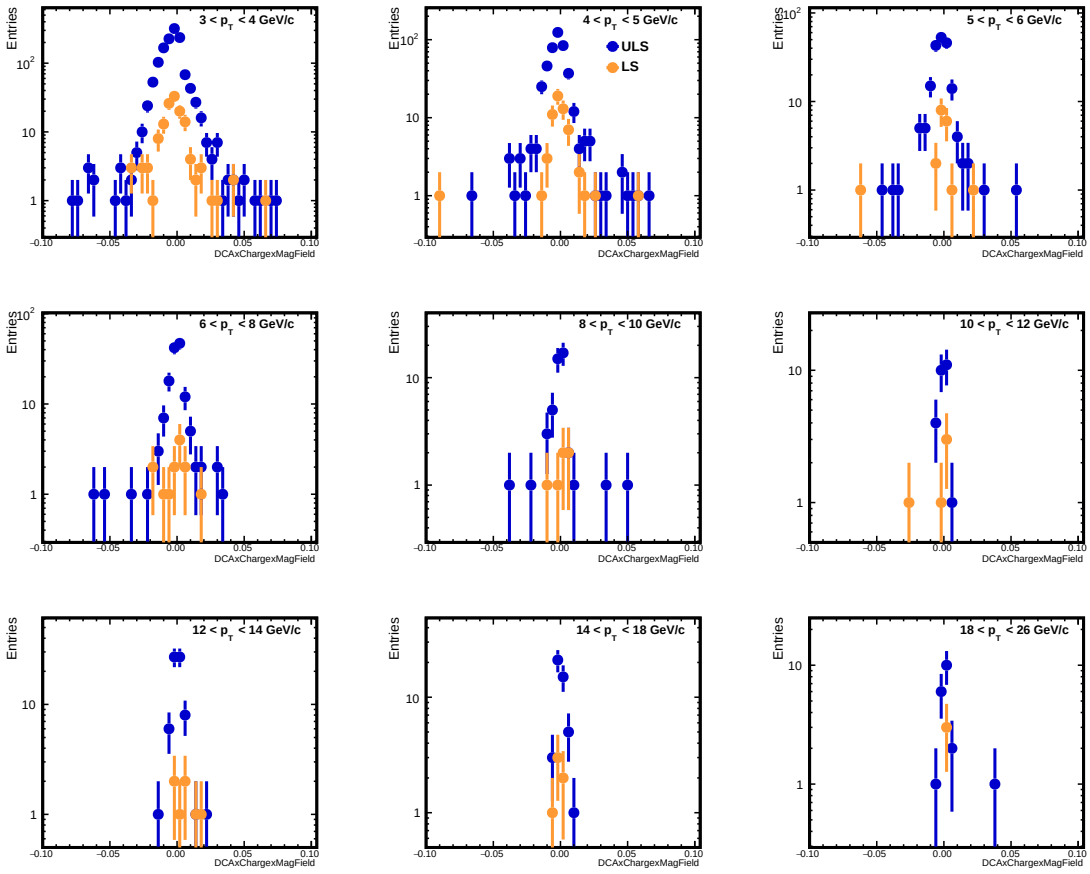

Figure 3.6: The DCA distributions of electrons that form an unlike-sign (like-sign) pair with $M_{ee} < 0.1$ GeV/c^2 in blue (orange) in 30-50% centrality.

calculation, but have a flat momentum distribution. This is shown in the red distribution in Figure 3.7. Unfortunately, this causes the p_{T} spectra of the photonic electrons to be artificially hard with respect to data, causing a bias in the efficiency calculation.

We correct this bias by applying a weight to electrons from the enhanced η and π_0. The η weight (as a function of p_{T}^{η}) is calculated by taking the ratio of the enhanced η spectrum to the non-enhanced Hijing η spectrum (see Figure 3.7). This ratio is then fitted with a parametrization of a modified Hagedorn function [142] which describes the p_{T} distribution of hadrons. The weight for π_0 is calculated in the same manner. Each weight is applied to the daughter electrons according to the p_{T} of the enhanced η or π_0 mother. The Hagedorn equation is given in Equation 3.5 below:

$$f = p_0 \times \left(\frac{e^{-p_1 x - p_2 x^2}}{p_3} \right)^{-p_4} \tag{3.5}$$

where x is the p_{T} of the mother η or π_0.

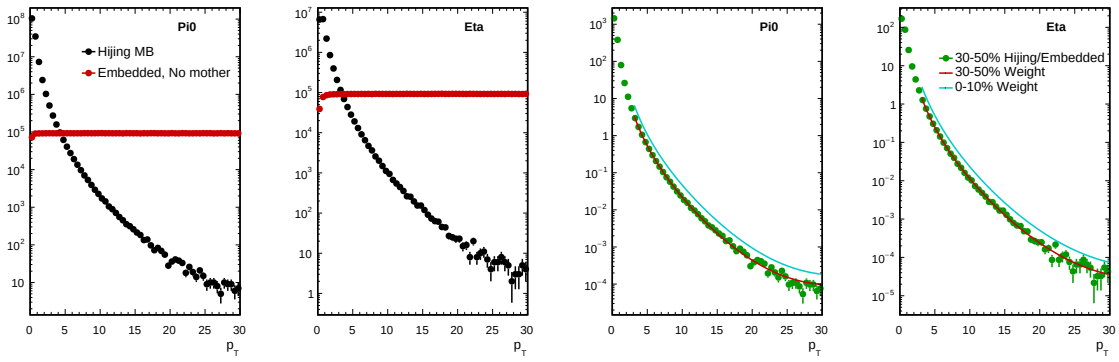

Figure 3.7: Left: The spectra of π^0 and η in the 30-50% MC sample (embedded in red, non-enhanced Hijing in black). Right: The weight functions applied to electrons from π^0 and η decays in MC (0-10% centrality in blue, 30-50% in red).

After applying the weight, the resulting tagging efficiency is fitted with Equation 3.6 to smooth the distribution and reject statistical fluctuations. The fit is shown in Figure 3.8. This figure also shows the tagging efficiency with and without applying the weight to the electrons from the enhanced η and π_0. Here, one sees that the η and π_0 weights cause the tagging efficiency to decrease at low momentum. At $p_{\mathrm{T}} = 3$ GeV/c, the tagging efficiency is reduced from $\sim 70\%$ to $\sim$50% when the weights are applied.

$$f = p_0 - p_1 \times e^{-x \times p_2} \tag{3.6}$$

3.3.3.3 Other background sources of electrons

The remaining background sources listed at the beginning of Section 3.3.3 have a relatively small contribution to electrons in the p_{T} range considered in this analysis. For example, in previous measurements, the contribution of electrons from J/ψ was estimated to be, at its maximum, $\sim$5% in the range $2 < p_{\mathrm{T}} < 3$ GeV/c for central Pb-Pb collisions at $\sqrt{s_{\mathrm{NN}}} = 2.76$ TeV [143]. The contribution decreases quickly at higher

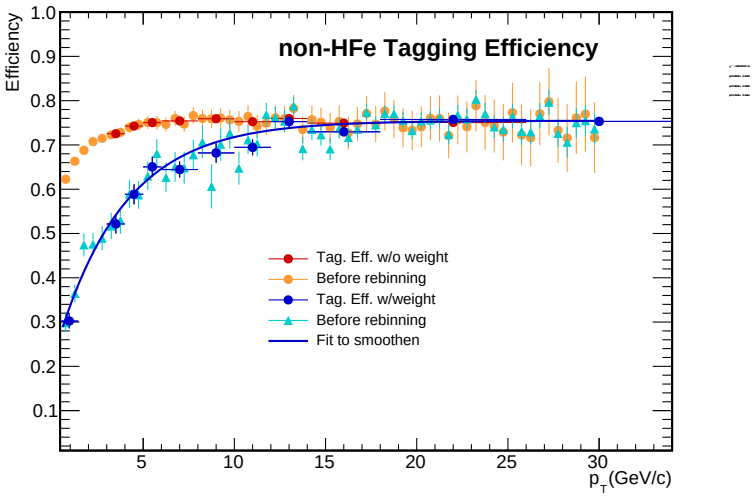

Figure 3.8: Tagging efficiency of photonic electrons before and after applying the weight to electrons from η and π_0 in the MC sample. The example shown here is in 30-50% centrality.

p_{T} and in more peripheral collisions. Thus, in this thesis analysis, as in previous measurements of heavy-flavor electrons [53], electrons from J/ψ are not explicitly subtracted from the sample. Other quarkonia sources produce even fewer electrons than J/ψ, and are considered negligible.

Background electrons from W decays and $\mathrm{Z}/\gamma^* \rightarrow \mathrm{e}^+\mathrm{e}^-$ decays only become significant at high momentum: the contribution from W decays increases from 1% to 20% between $p_{\mathrm{T}} = 10$ GeV/c and 25 GeV/c, while the Z contribution reaches 10% at 25 GeV/c [53]. In previous studies of heavy-flavor electrons [53], the electrons from W and Z were estimated using POWHEG [144] and subtracted from the final HFe spectrum. This method cannot be employed for this analysis, as it is unclear how the contribution from W and Z electrons affect the DCA distribution and fitting procedure. Instead, an additional systematic uncertainty is added to the measurement at high transverse momentum. Details on how this uncertainty is estimated can be found in Chapter 4.

The remaining sources of background electrons from K_{e3} decays and light vector mesons (ω, η', and ϕ) are negligible [143, 145].

3.4 Separating charm- and beauty-decay electrons

After subtracting the hadron background and photonic electrons, we are left with a sample of heavy-flavor electrons from both charm and beauty decays. We still need to separate these two sources. This can be done by exploiting the difference in decay-length of charm and beauty hadrons (see Table 3.5). Because beauty hadrons have a long lifetime before decay, their decay electrons are produced at a larger radius from the primary vertex. Thus, when the electron track is extrapolated backward, it will have a larger distance-of-closest-approach (DCA) to the primary vertex [45, 63]. As the name suggests, the DCA is the closest distance between an extrapolated particle track and the primary vertex. The idea that a longer mother particle lifetime results in a larger daughter DCA is best understood by looking at Figure 3.9, where a schematic illustration of a beauty-decay and charm-decay electron is provided.

Table 3.5: Decay lengths of beauty and charm hadrons [7]

Particle species	Quark content	Decay length (μm)
D^+	$c\bar{d}$	311.8
D^0	$c\bar{u}$	122.9
D_s^+	$c\bar{s}$	151.1
Λ_c^+	udc	60.68
B^+	$u\bar{b}$	491.1
B^0	$d\bar{b}$	455.4
B_s^0	$s\bar{b}$	454.2
Λ_b^0	udb	441

When we plot the DCA of the beauty-decay electrons, its distribution will be wider than charm-decay electrons due to its large DCA. This can be seen in the MC simulation plot in Figure 3.10. Because the charm- and beauty-decay electron distributions have different shapes, we can attempt to fit the two shapes to the combined heavy-flavor decay electron DCA distribution, extracting the fraction of each source of electrons from the combined heavy-flavor electrons.

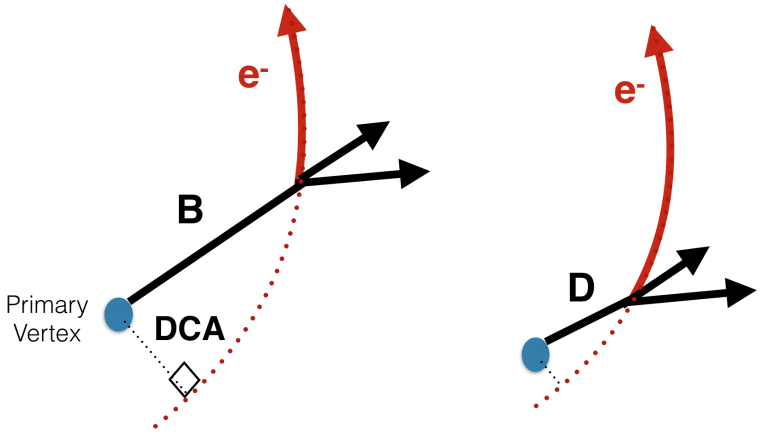

Figure 3.9: Illustration of how the meson decay length affects the DCA of the decay electrons.

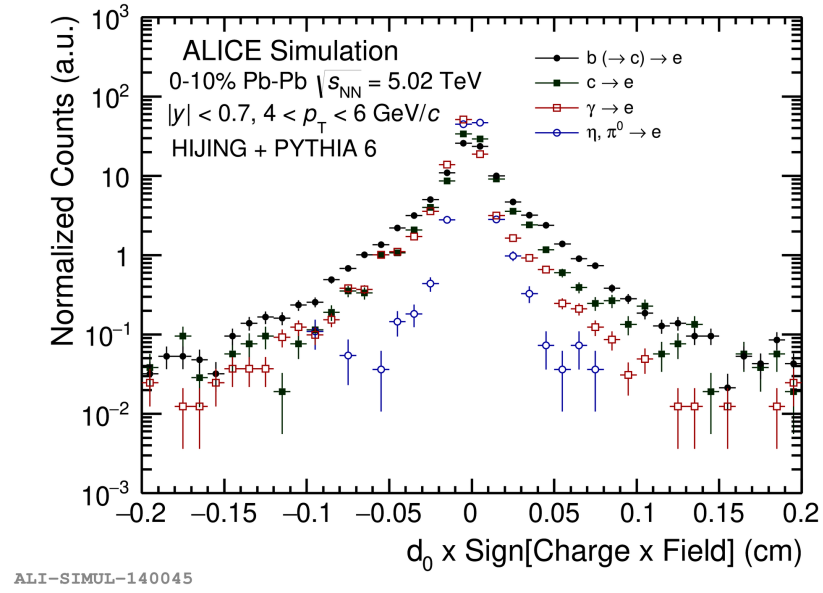

Figure 3.10: The DCA distributions of electrons from different sources, generated using MC simulations. Here, d_0 is used to denote distance-of-closest approach (DCA).

3.4.1 Fitting procedure

The shapes, or templates, of the DCA distributions of charm- and beauty-decay electrons are obtained from Monte Carlo simulation. Tracks in MC are selected with the same criteria used in data (Table 3.1). Electrons are selected and sorted into two templates according to the decay chain that produced them. The decay processes

considered and added to the templates are listed below:

Charm Template

$D^0, D^{\pm}, D_s^{\pm} \rightarrow e$

$\Lambda_c \rightarrow e$

Beauty Template

B mesons $\rightarrow$ e

B mesons $\rightarrow$ D mesons $\rightarrow$ e

B mesons $\rightarrow$ c Baryons $\rightarrow$ e

B mesons $\rightarrow$ ... $\rightarrow$ D mesons $\rightarrow$ e

B mesons $\rightarrow$ ... $\rightarrow$ c baryons $\rightarrow$ e

where the ellipses indicate several generations of decays. (The decay chain of electrons from charm hadrons are checked back 100 generations to look for a B meson mother.)

One may notice that, with the exception of electrons from Λ_c in the charm template, the two templates only include electrons from D or B meson decays. It is important to include the Λ_c contribution because its decay length, $c\tau = 60.68$ μm, is much shorter than the decay lengths of D mesons, which range from about 150-300 μm [7]. Thus its contribution can alter the charm template shape by making it narrower. Other charm baryons are not included because they have a small contribution to charm-decay electrons. Beauty baryons are not included because they have a very similar lifetime to the B mesons ($c\tau = 441$ μm for Λ_b) and have a negligible effect on the beauty template. (See Table 3.5 for a list of relevant decay lengths.)

These templates require some altering before they can be used to fit data. This is because there are several known ways in which the MC simulation does not match data that can affect the shapes of the templates. Because the MC sample is a heavy-flavor enhanced sample, the D and B meson p_{T} spectra are artificially high at high momentum (i.e. harder spectra). Also, the relative fraction of different charm species (i.e. the $D^{\pm}/D^0$, $D_s^{\pm}/D^0$, and Λ_c/D^0 ratios) do not match data measurements. It is important that these ratios are correct in the charm template, since these particles have different decay lengths and can affect the template shape. The relative fraction of different beauty species are not corrected in the beauty template, as they have similar decay lengths. Finally, the DCA mean and resolution is different in data and MC. The corrections made to compensate for these differences are in Section 3.4.2.

Once the template corrections are applied, the templates are normalized so their integral is one. They are then fitted to the heavy-flavor electron DCA using a weighted log-likelihood fit based on a method by Frederick James [146]. This fit procedure is for cases in which the fitted histogram has been filled with weighted counts that are different than one. In such cases, the parameter errors produced from a standard log-likelihood fit must be corrected to account for the weighted entries. This method was chosen because the heavy-flavor electron DCA distributions in general contain non-integer counts due to the hadron and photonic electron subtraction. To ensure the weighted log-likelihood fit was appropriate for this measurement, several closure test studies were performed and are detailed in Section 4.7.

The fit function is a simple combination of the two normalized templates:

$$fit = p_0 \times Template_{b\to e} + (N_{HFe} - p_0) \times Template_{c\to e} \tag{3.7}$$

where N_{HFe} is the integral of the fitted heavy-flavor DCA distribution. Since the templates are normalized so their integrals are one, the free parameter p_0 corresponds to the raw beauty yield extracted from the fit. Figure 3.11 shows a few examples of the template fit in different momentum ranges.

In the final step of this analysis, the raw beauty-decay electron yield is corrected for the acceptance and efficiency of the ALICE detector and the efficiency of the electron selection criteria (Section 3.5).

3.4.2 Template Corrections

As previously mentioned, there are a number of corrections that must be applied to the templates because the MC sample does not match data. The first is that the D meson, B meson, and Λ_c momentum spectra in MC do not match data. This is due, in part, to the fact that additional charm and beauty quarks were embedded in the MC sample, which artificially increased the number of high-p_{T} charm and beauty hadrons. This affects the shape of the templates because the DCA shape has a p_{T} dependence: higher p_{T} particles have a narrower DCA distribution. The correction for this issue is described in Sections 3.4.2.1 and 3.4.2.2.

Another difference between data and MC is the relative fraction of different charm species. This means, for example, that the D^+/D^0, D_s/D^0, and Λ_c/D^0 ratios measured in data do not match MC. This affects the templates because different charm

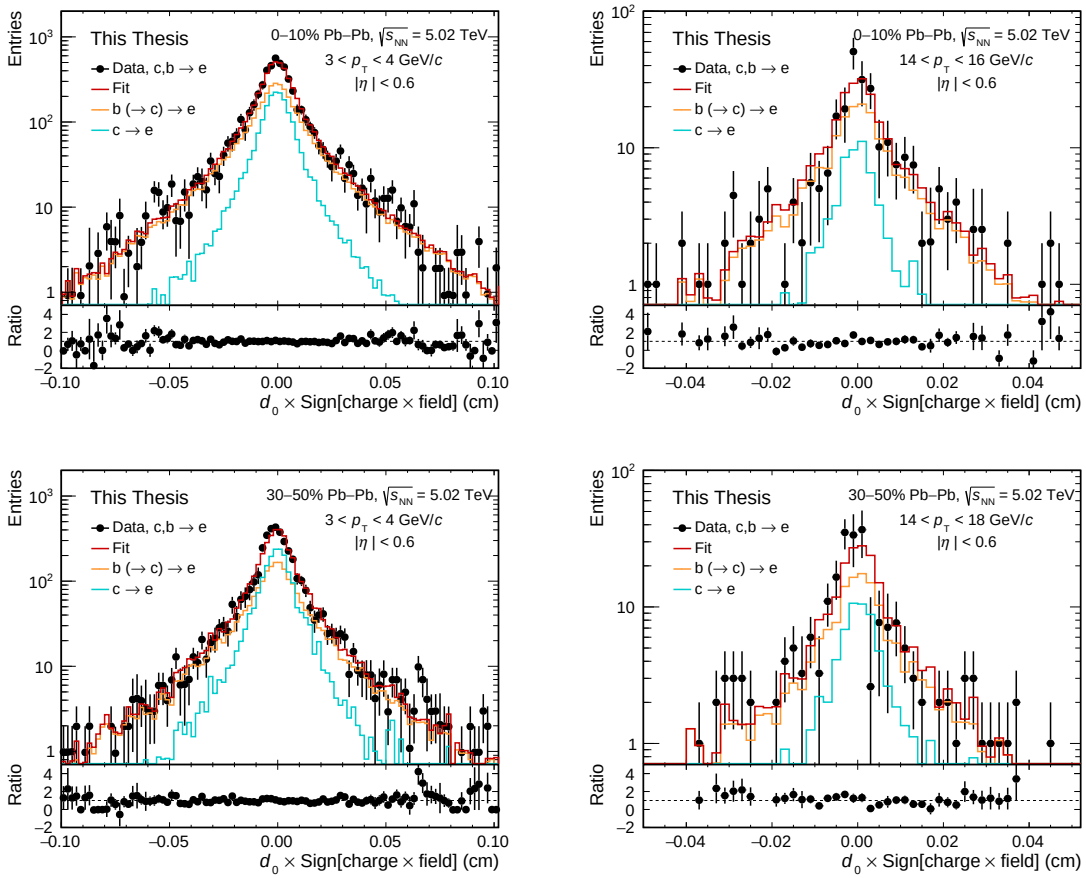

Figure 3.11: Examples of template fits in 0-10% and 30-50% centrality in different p_{T} bins.

species have different decay lengths, and thus their decay electrons have different DCA shapes. If the wrong fraction of electrons from a particular species is included in the template, it could alter the template shape.

Finally, there is a small difference in the mean and resolution of the DCA in data and MC. In data, the DCA mean is reduced about 5-10 μm, likely due to a misalignment of some of the SPD modules during the `LHC15o` data-taking period. The mean shift and resolution difference between the MC and data DCA distributions is corrected using an online central ALICE code known as the "Improver Task". The Improver Task goes track by track in the MC to correct the mean shift and difference in resolution to match data.

Examples of the templates before and after the B meson weight, D meson weight,

and the D^0 ratio corrections are applied can be seen in Figure 3.12. Taken together, the corrections make the templates narrower.

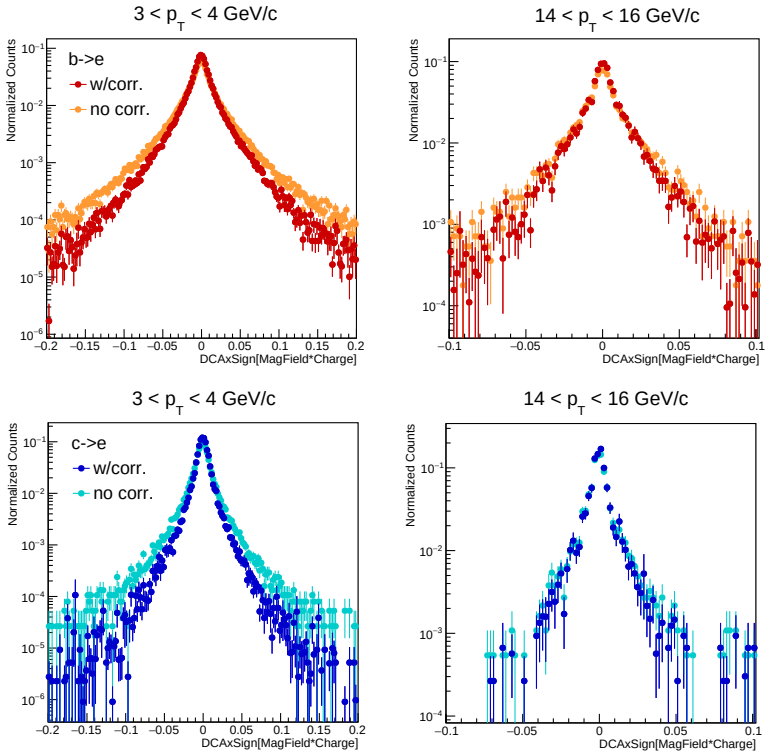

Figure 3.12: The beauty (top) and charm (bottom) templates before and after the B meson weight, D meson weight, and the D^0 ratio corrections are applied in 0-10% centrality.

3.4.2.1 D meson spectrum

The D meson spectrum in MC is corrected to match data using a p_{T}-dependent weight. This weight is simply the D^0 p_{T} distribution measured in 5.02 TeV Pb-Pb collisions by the ALICE detector [36] divided by the p_{T} spectrum of D^0 mesons in the MC sample. The same weight is used for all D meson species since their p_{T} distributions have the same shape in both data and MC (see Figure 3.13 and 3.16). This weight mainly serves to correct the spectrum shape; the relative contribution of the electrons from different D meson species is corrected in a later step (Section 3.4.2.3).

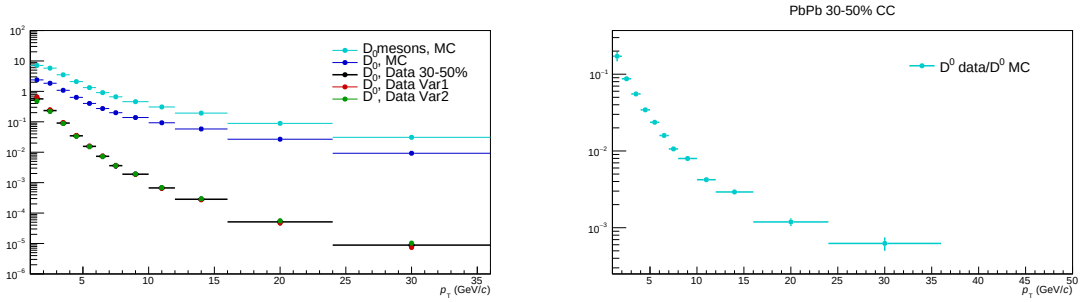

Figure 3.13: Left: the MC spectra of D^0 (blue) and all D mesons (cyan) and the data spectra of D^0 (black) in 30-50% Pb-Pb collisions. The two variations used for systematic uncertainty estimation are shown in red and green. Right: the weight applied to the electrons from D mesons, according to the D meson p_{T} (cyan).

Once this weight distribution is obtained, the p_{T} of electrons from D mesons are weighted according to the mother D meson p_{T}.

3.4.2.2 B meson spectrum

The B meson spectrum in MC was also corrected using a p_{T}-dependent weight. In this case, however, the B meson measurement available in Pb-Pb collisions from CMS [37] only extends in the range $7 < p_{\mathrm{T}} < 50$ GeV/c and combines collisions of all centralities. This is not sufficient to calculate the B meson weight using the same method employed for the D meson weight.

Instead, the correction relies on theoretical predictions. The expected B meson p_{T} spectrum shape in 0-10% (30-50%) was obtained by multiplying a fit to the 0-10% (20-40%) B meson R_{AA} from the TAMU model [147] with the pp B meson cross section from FONLL. This product is shown in the numerator of Equation 3.8. One might notice that the constant factor from the T_{AA} is still present, but this is not a concern: we wish to correct the shape of the p_{T} distribution, not the absolute value. The fit function of the TAMU prediction is given in Equation 3.9.

$$Weight = \frac{\frac{N_B^{PbPb}/dp_{\mathrm{T}}}{T_{\mathrm{AA}} \times \sigma_B^{pp}/dp_{\mathrm{T}}}\Big|_{TAMU} \times \sigma_B^{pp}/dp_{\mathrm{T}}\Big|_{FONLL}}{N_B^{PbPb}/dp_{\mathrm{T}}\Big|_{MC}} \tag{3.8}$$

$$\text{TAMU } R_{\mathrm{AA}} \text{ fit} = p_0 + \frac{p_{\mathrm{T}} - p_1}{p_2} + \frac{p_3}{1 + e^{p_4 \cdot (p_{\mathrm{T}} - p_5)}} \tag{3.9}$$

The TAMU model was chosen because its shape is reasonable compared with other model predictions and the measurement of the B meson R_{AA} (see [37]). However, in the systematic uncertainty determination, the model R_{AA} used in the weight calculation was varied to account for a wide range of possible predictions. See Chapter 4 for more information.

All of the ingredients for this weight calculation are shown in Figure 3.14. Once the weight is calculated (Figure 3.15), the electrons from B mesons are weighted according to their B parent p_{T}.

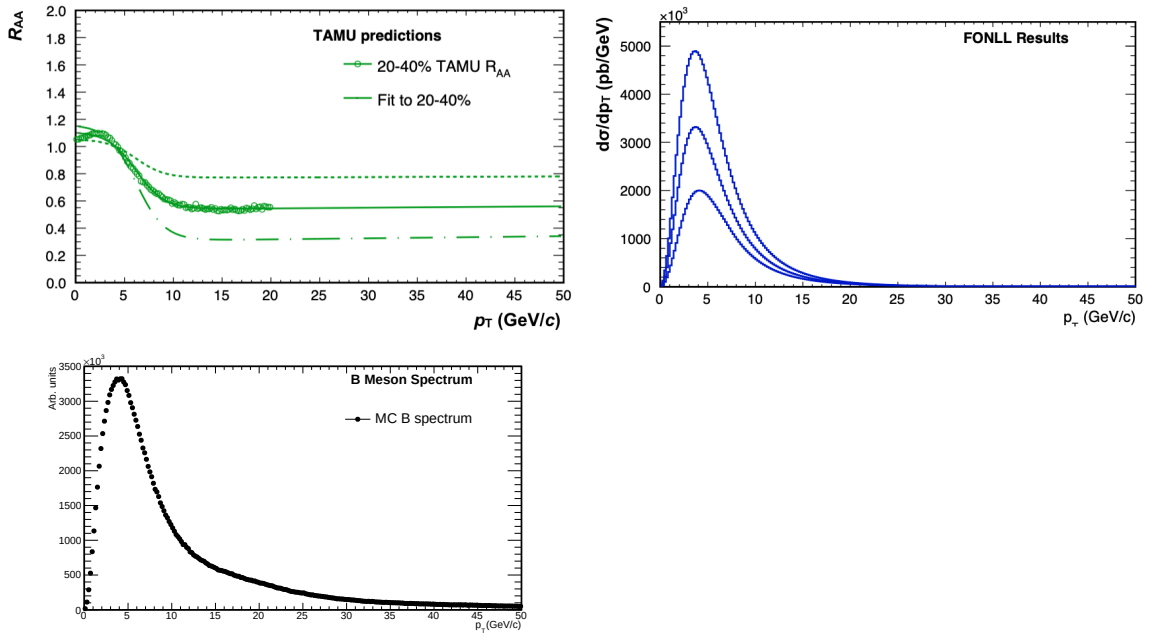

Figure 3.14: Top left: the TAMU R_{AA} of B mesons in 20-40% (green). The variations for systematics are shown by the dashed lines. Top right: the FONLL cross section of B mesons in pp 5.02 TeV. Bottom: the MC B meson spectrum in 30-50% centrality.

3.4.2.3 Relative fraction of different D meson species

The relative fraction of different D mesons is corrected by scaling the contribution of the D^+ and D_s^+ electrons in the charm template by a constant factor (see Equation 3.10). The scale factor (c_1 and c_2) is informed by the $\frac{D^+}{D^0}$ and $\frac{D_s^+}{D^0}$ measured in 5.02 TeV Pb-Pb data [36] and the branching ratios (BR) of D^+ and D_s^+ to electrons [7]. The last term in the scale factors is the ratio of the number of electrons from D^+ or

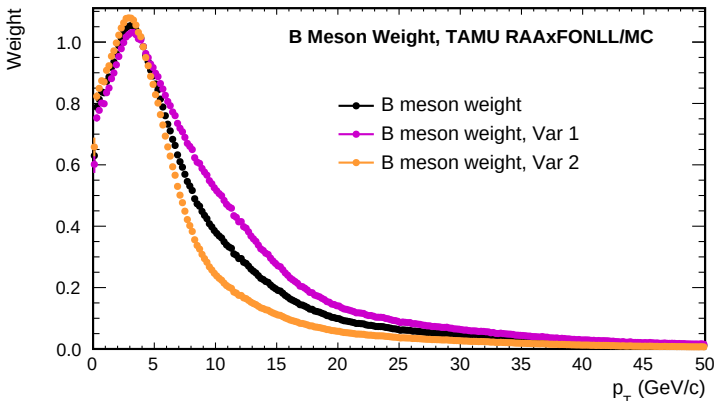

Figure 3.15: The weight applied to electrons according to their mother B meson p_{T} (black) in the 30-50% MC sample. The variations for systematics are shown in magenta and orange.

D_s^+ to the number of electrons from D^0 in the MC sample.

$$\mathrm{Template_c} = DCA(D^0 \to e) + c_1 \cdot DCA(D^+ \to e) + c_2 \cdot DCA(D_s \to e) + DCA(\Lambda_c \to e)$$

$$\text{where} \quad c_1 = \left(\frac{D^+}{D^0}\right)_{data} \times \frac{BR(D^+ \to e)}{BR(D^0 \to e)} \times \left(\frac{N_{D^0 \to e}}{N_{D^+ \to e}}\right)_{MC}$$

$$c_2 = \left(\frac{D_s}{D^0}\right)_{data} \times \frac{BR(D_s \to e)}{BR(D^0 \to e)} \times \left(\frac{N_{D^0 \to e}}{N_{D_s \to e}}\right)_{MC} \tag{3.10}$$

The D^0 ratios measured in data can be seen in Figure 3.16. The value of these ratios used in the c_1 and c_2 equations is constant in p_{T} and is obtained by a simple fit line to the data.

3.4.2.4 Λ_c spectrum and Λ_c/D^0 correction

Recent results in 2018 data [148] have shown that the Λ_c spectrum has a difference in shape from the D^0 spectrum. Consequently, the Λ_c/D^0 ratio in data (Figure 3.16) has a p_{T}-dependence and must be corrected according to the p_{T} of the electron mother. This is accomplished by applying a separate weight to the electrons from Λ_c, described by Equation 3.11. It is the Λ_c/D^0 in data [148] times the D^0 p_{T} distribution from data [36] and divided by the Λ_c p_{T} distribution in the MC sample.

$$Weight = \frac{\Lambda_c}{D^0}\Big|_{data} \times \frac{(dN_{D^0}/dp_T)_{data}}{(dN_{\Lambda_c}/dp_T)_{MC}} \tag{3.11}$$

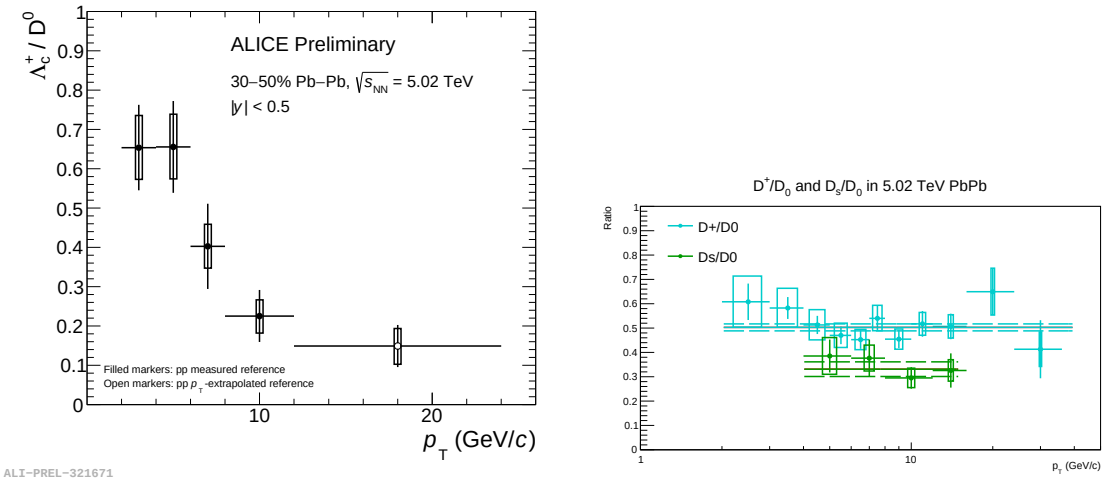

Figure 3.16: Ratios of different D mesons and Λ_c to the number of D^0 in 30-50% data [36, 148]. The lines on the right plot show the fit to determine the value of the D^+/D^0 and D_s/D^0 ratio correction. The dashed lines show the systematic variations.

Figure 3.16 shows the Λ_c/D^0 in data, Figure 3.13 gives the D^0 p_{T} distribution in data, and Figure 3.17 provides the Λ_c p_{T} distribution in MC and the final weight applied to the Λ_c electrons.

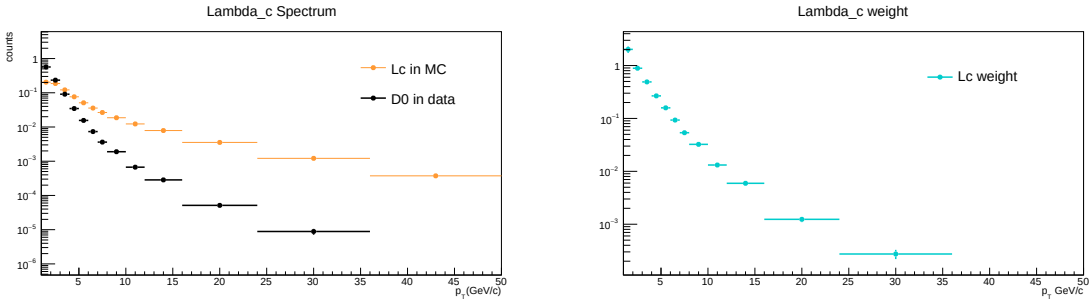

Figure 3.17: Left: The Λ_c spectrum in MC (yellow) and the D^0 spectrum from data (black) in 30-50%. Right: The weight applied to electrons from Λ_c according to the mother Λ_c p_{T} for 30-50% centrality.

3.5 Acceptance and reconstruction efficiency

The raw beauty yield, extracted from the template fit procedure, needs to be corrected for the acceptance of the ALICE detector and the efficiency of the methods used in this analysis. This includes the efficiency corrections for the track quality selections, the track matching with EMCal clusters, and the selections used to identify electrons (the E/p, M20, and $n\sigma_{\mathrm{TPC-dE/dx}}$ requirements). These corrections are estimated using MC simulations, with the exception of the $\mathrm{n}\sigma_{\mathrm{TPC-dE/dx}}$ and M20 electron selection efficiencies. This is done by comparing the number of beauty-decay electrons in the MC sample before and after a selection is applied. For example, the track selection efficiency would be calculated by dividing the total number of beauty-decay electrons in the MC sample after the track quality selections ($N_{passTrackCuts}$) by the total number beforehand (N_{all}). The total efficiency is described by Equation 3.12.

$$\begin{aligned}\varepsilon_{total} &= \varepsilon_{TrackCuts} \times \varepsilon_{EMClusterMatch} \times \varepsilon_{EoPeID} \times \varepsilon_{M20eID} \times \varepsilon_{TPCeID} \\ &= \frac{N_{trackCuts}}{N_{all}} \times \frac{N_{matchEMCcluster}}{N_{trackCuts}} \times \frac{N_{passE/pCut}}{N_{matchEMCcluster}} \times \frac{N_{passM20cut}}{N_{passE/pCut}} \times \frac{N_{passTPCeIDcut}}{N_{passM20cut}}\end{aligned} \tag{3.12}$$

The first term describes the efficiency of the track selection criteria, and the second describes the efficiency of matching tracks to clusters in the EMCal. The third term is the efficiency of the E/p criterion for electron identification ($0.8 < E/p < 1.2$), and the fourth the efficiency of the M20 selection ($0.01 < M20 < 0.35$). The final term is the efficiency of the $\mathrm{n}\sigma_{\mathrm{TPC-dE/dx}}$ selection for identifying electrons ($-1 < \mathrm{n}\sigma_{\mathrm{TPC-dE/dx}} < 3$). The M20 and $\mathrm{n}\sigma_{\mathrm{TPC-dE/dx}}$ selection efficiencies are discussed in further detail in Sections 3.5.1 and 3.5.2.

It should be noted that the total efficiency does not correct for the limited pseudorapidity range used in this analysis; N_{all} already includes the requirement that the beauty-decay electrons lie in the range $|\eta| < 0.6$. However, the EMCal acceptance is indirectly considered in the second term of the efficiency, since $N_{matchEMCcluster}$ is limited by the η and ϕ range of the EMCal detector. The efficiency as a whole also accounts for detector acceptance "holes," such as gaps between the TPC modules or dead pixels.

3.5.1 Data-driven $n\sigma_{\mathrm{TPC-dE/dx}}$ Selection Efficiency

The MC sample does not accurately reproduce the $n\sigma_{\mathrm{TPC-dE/dx}}$ distribution we see in data due to differences in the parameter values of the Bethe-Bloch equation and the mean and sigma of the TPC dE/dx. Therefore, the efficiency of the $n\sigma_{\mathrm{TPC-dE/dx}}$ selection ($-1 < n\sigma_{TPC-dE/dx} < 3$) is not accurately described by MC, and must be calculated using a data-driven method. This is achieved by plotting the $n\sigma_{TPC-dE/dx}$ distributions of electrons passing the $0.8 < E/p < 1.2$ selection in different p_{T} ranges. These distributions are then fitted with three gaussians, as seen in Figure 3.18. The blue gaussian describes the electron contribution, the black describes the pions, and the green describes the remaining protons and kaons. The $n\sigma_{\mathrm{TPC-dE/dx}}$ electron selection efficiency is then simply the integral of the blue electron gaussian in the selection region ($-1 < n\sigma_{TPC-dE/dx} < 3$) divided by the total integral of the gaussian.

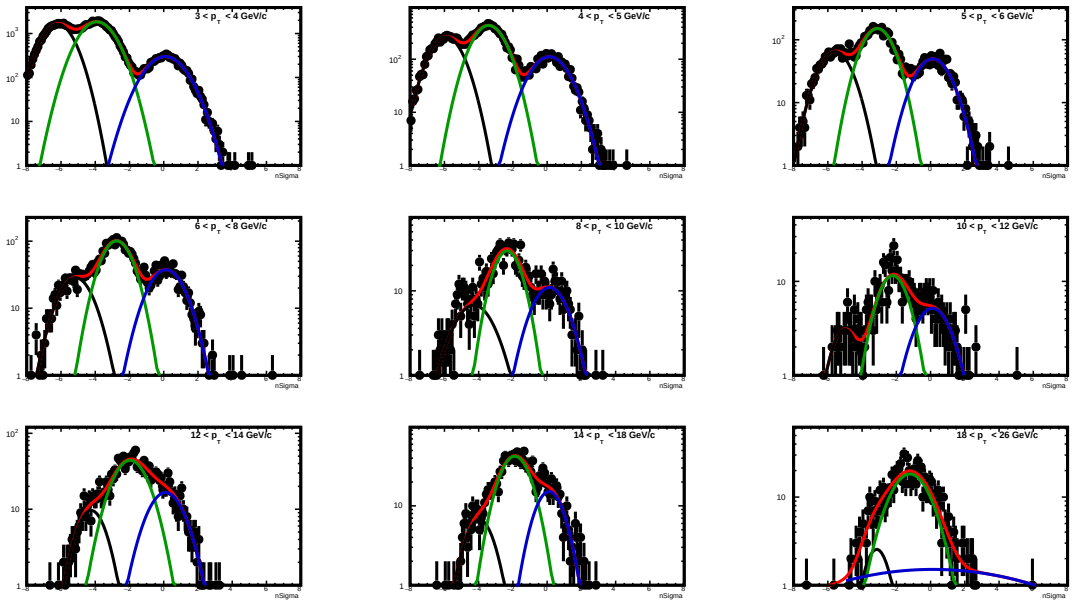

Figure 3.18: $n\sigma_{TPC-dE/dx}$ distributions after applying the eID cut $0.8 < E/p < 1.2$ in different p_{T} bins in 30-50% centrality. Three gaussians were fitted to estimate the true electrons and background. The TPC eID efficiency was estimated by integrating the blue electron gaussian in the cut region ($-1 < n\sigma_{TPC-dE/dx} < 3$) and dividing by the total integral of the gaussian.

This method of estimating the $n\sigma_{\mathrm{TPC-dE/dx}}$ electron selection efficiency is not as reliable at higher p_{T} because the peaks begin to merge together and the statistics

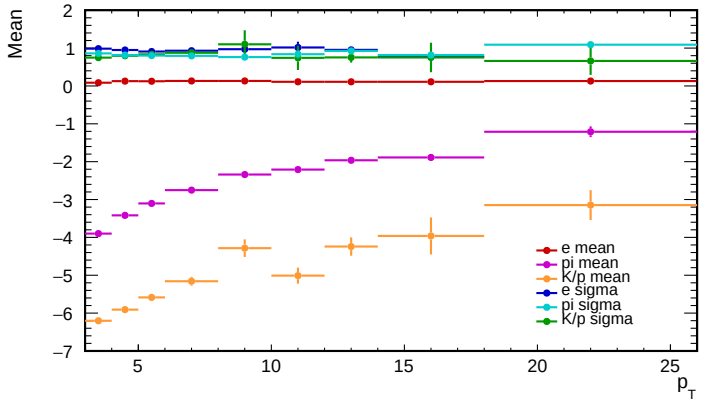

Figure 3.19: The means and sigmas of the gaussians used to fit the $n\sigma_{TPC-dE/dx}$ distributions for the TPC $n\sigma_{TPC-dE/dx}$ cut efficiency. Note the π_0 and K/p gaussian means creep toward the electron mean as the p_{T} increases.

are lower. This is particularly true in the range from 8-12 GeV/c, where the minimum bias trigger statistics are low, and the very high momentum ranges where the EG1-triggered events also begin to lose statistics. To account for this, the efficiency distribution is smoothed by fitting a straight line to the points from 5-26 GeV/c. The value of the fit line is used for the TPC efficiency for $p_{\mathrm{T}} > 8$ GeV/c (see Figure 3.20).

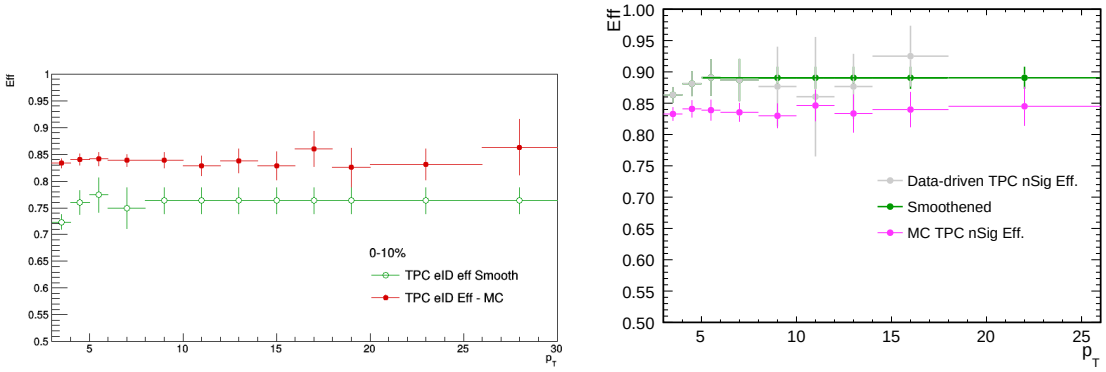

Figure 3.20: The data-driven n$\sigma_{\mathrm{TPC-dE/dx}}$ electron selection efficiency using the data-driven method (gray) and the n$\sigma_{\mathrm{TPC-dE/dx}}$ electron selection efficiency using MC. The left plot is in 0-10% centrality, the right is in 30-50%.

In Figure 3.20, one can see that the data-driven method gives an efficiency that is about 5-10 percentage points lower than the MC method in the 0-10% measurement.

In the 30-50% measurement, the reverse is true: the data-driven method gives a higher efficiency by about 5 percentage points.

3.5.2 Data-driven M20 Electron Selection Efficiency

The efficiency of the M20 selection for electrons ($0.01 < M20 < 0.35$) was calculated using a data-driven method to see if the MC M20 efficiency was reasonable. (It is known that the MC simulation does not reproduce the shower shape in the EMCal with complete accuracy.) To calculate this efficiency, the E/p distributions of electrons were generated with and without the M20 selection applied. The data-driven efficiency is then the integral of the electron signal in the region $0.8 < E/p < 1.2$ with the M20 selection applied, divided by the same integral when the M20 selection is not applied. The E/p distributions without the M20 selection applied can be seen in Figure 3.21. The results of the data-driven method are reasonably consistent with the MC efficiency (see Figure 3.22) in 30-50% centrality, but differ in 0-10% by about 2-8% depending on the momentum considered. The data-driven M20 efficiency is used in the 0-10% analysis as a result. However, to avoid fluctuations due to the hadron subtraction in both the numerator and denominator of the data-driven efficiency, the MC efficiency is used in 30-50%.

3.6 Rejection Factor

As explained in Section 2.2.3.2, the EMCal detector can be used to trigger on events with large energy depositions > 10 GeV. This ultimately increases the statistics of high-momentum electrons in the data sample. However, it also artificially increases events with high-energy particles when compared with the minimum bias trigger. This can be seen on the left in Figure 3.24, where the cluster energy distribution is plotted for minimum bias data (open circles) and EMCal-triggered EG1 data (closed circles).

To correct for this, the number of EG1 events is multiplied by a "rejection factor" (RF). This factor increases the number of EG1 events so that it matches the equivalent number of minimum bias events needed to produce the same number of high-energy particles. The beauty-decay electron yield obtained in EG1 data is then divided by both the number of EG1 events and the RF. (The beauty-decay electron yield in

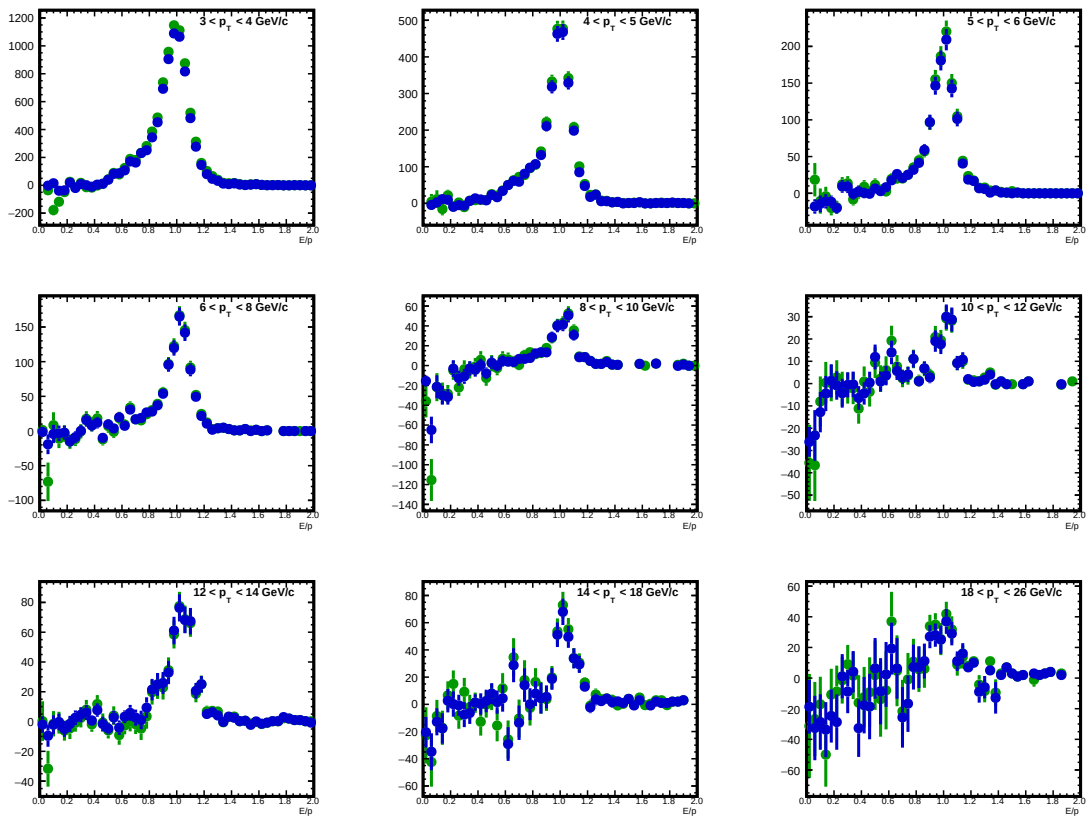

Figure 3.21: The E/p distributions used to calculate the data-driven M20 efficiency in 30-50%. Both distributions have the cut $-1 < n\sigma_{TPC-dE/dx} < 3$ applied, but the blue distribution has an additional cut of $0.01 < M20 < 0.35$.

minimum bias data, on the other hand, is only divided by the number of minimum-bias triggered events.)

The RF is calculated by taking the ratio of the cluster energy distribution in EG1 events divided by the cluster energy in minimum bias events (on the right in Figure 3.24). This ratio is then fitted with the function in Equation 3.13.

$$f_{RF} = p_0 + \frac{p_1}{1 + e^{\frac{-x+p_2}{p_3}}} \tag{3.13}$$

In this analysis, the rejection factor is the value of the fit function at 15 GeV, where the distribution is a stable plateau. This factor is only valid at high energies where the "trigger plateau" is present, above 12 GeV. Thus, EMCal-triggered data is only

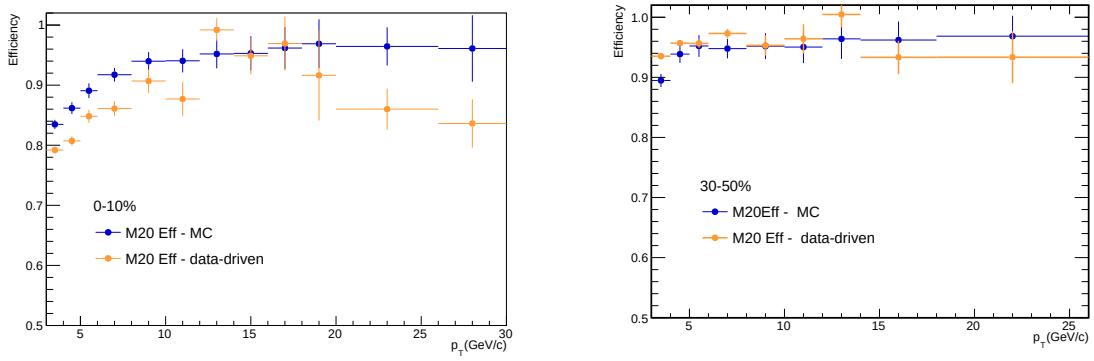

Figure 3.22: The data-driven M20 electron selection efficiency using the data-driven method (gold) and the M20 electron selection efficiency using MC (blue). The left plot is in 0-10% centrality, the right is in 30-50%.

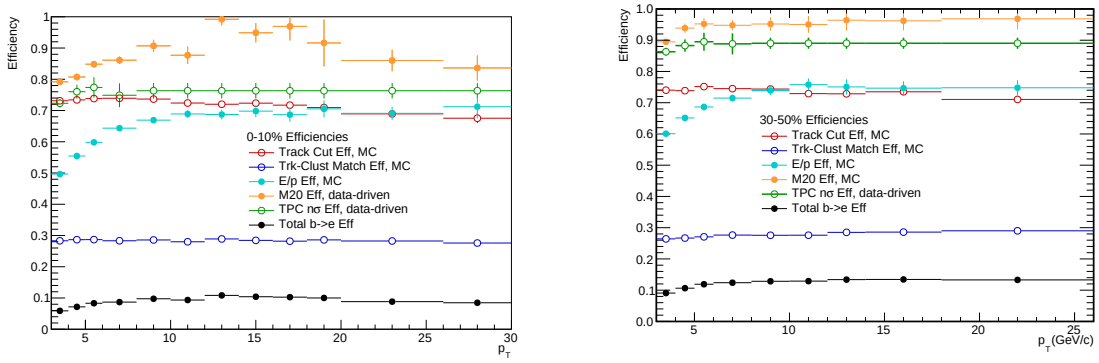

Figure 3.23: A summary of the efficiencies in 0-10% (left) and 30-50% (right).

used in this analysis when measuring beauty-decay electrons with $p_{\mathrm{T}} > 12$ GeV/c. The rejection factor value for 0-10% is 61.282, and for 30-50% it is 229.572.

3.7 pp Reference

In this section, the cross-section of beauty-decay electrons in pp collisions, needed as the "pp reference" for the nuclear modification factor (Equation 5.1), is discussed. For $p_{\mathrm{T}} < 8$ GeV/c, the pp reference is the measurement of beauty-decay electrons in pp collisions at $\sqrt{s} = 5.02$ TeV measured with ALICE [80]. Currently, beauty-decay electrons have not been measured for $p_{\mathrm{T}} > 8$ GeV/c in pp collisions with any detector

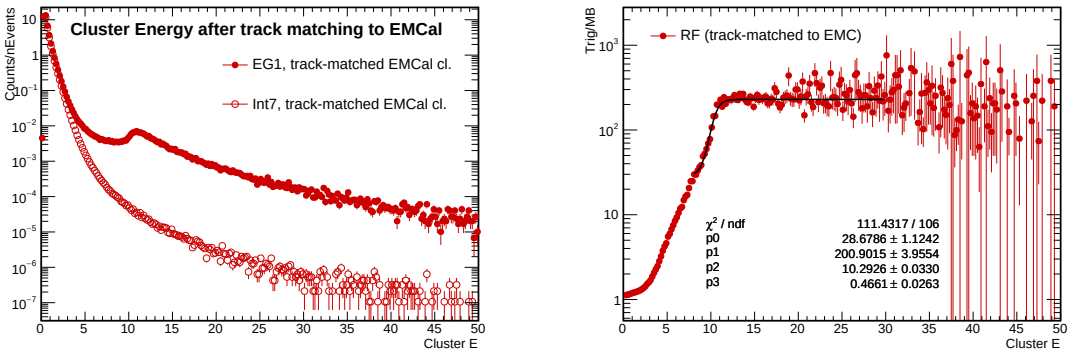

Figure 3.24: Left: the cluster energy of the min bias triggered data (open circle) and the EMCal-triggered data (closed circle). Right: the ratio of the triggered and min bias data. The fit line to get the RF value is shown in black. Update with 0-10% plot as well.

at any energy. Thus, FONLL predictions are used as a reference at high-p_{T}. The settings used to generate the predictions are listed in Table 3.6.

Table 3.6: FONLL settings

Option	Selection
Collider and System	LHC (pp, 5.03 TeV), ptmax $\leq$ 300 GeV
Heavy quark	bottom
Cross Section Type	$d\sigma/dp_{\mathrm{T}}$ (pb/GeV)
η min, max	-0.6, 0.6
Hadronic final state	B hadron
Further decay	$B \to e, \quad B \to D \to e$
Uncertainties	Uncertainty range from scales and masses
Include PDFs uncertainties	Yes
Other options	Default

This FONLL prediction cannot be used directly as a pp reference, however. Looking at Figure 3.25, one sees that the data measurement at low-p_T lies on the upper edge of the FONLL uncertainty band. Thus, if FONLL is used as a reference at higher momentum, we risk underestimating the pp reference.

To remedy this issue, the FONLL spectrum is scaled to match the low-p_{T} data reference. To do this, the ratio of the FONLL distribution to the data reference is fitted with the function in Equation 3.14. The ratio and fit results can be seen in

Figure 3.26. The FONLL points are then divided by the value of this fit function at the p_{T} bin center. The resulting scaled FONLL spectrum can be seen in Figure 3.27.

$$f = -p_0 + \frac{p_1}{1 + e^{\frac{-x+p_2}{p_3}}} \tag{3.14}$$

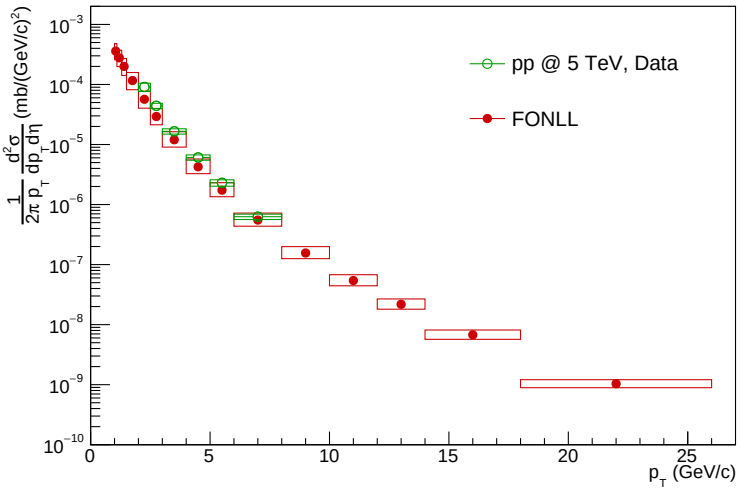

Figure 3.25: The pp reference in data for the $p_{\mathrm{T}} < 8$ GeV/c (green) and the FONLL cross-section. [The prefactor $1/(2\pi p_{\mathrm{T}})$ is present in the measured cross section in data, so it is also applied here to the FONLL cross section for comparison.]

The error assigned to the scaled FONLL is calculated by taking the sum in quadrature of the error from the original FONLL prediction and the systematic error of the scaling. This scaling systematic is estimated by first fitting a straight line to the ratio plot shown in Figure 3.26 in the momentum region where it is relatively flat (4-8 GeV/c). The two variations are obtained by varying the straight line fit within its parameter errors, shown in cyan and red in Figure 3.26.

Since there is a chance that the data points would be in better agreement with FONLL predictions at high momentum, it was ensured that the error on the scaled FONLL distribution was large enough to include the original FONLL prediction. This was true for all $p_T > 8$ GeV/c, with the exception of the last momentum bin. There, the error was increased by a small amount to include the central FONLL point.

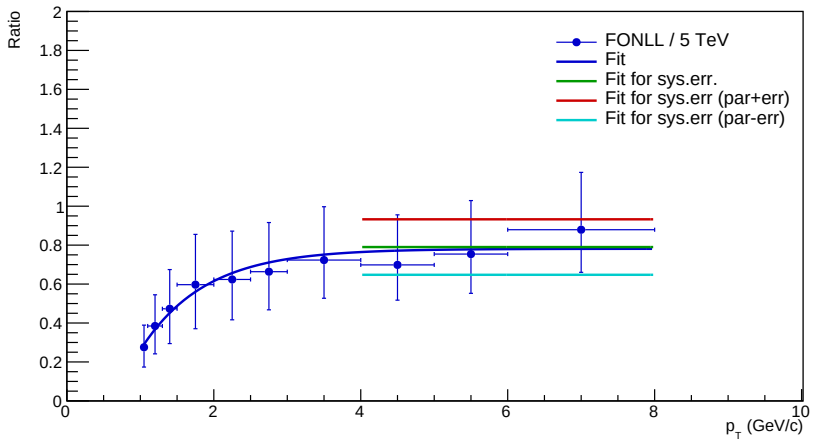

Figure 3.26: The ratio between the FONLL cross section and the low-p_{T} data reference. The blue fit line is used to scale the FONLL results to create the reference at high-p_{T}. The green line is a straight line fit to the data points between 4-8 GeV/c. The cyan and red lines are used to calculate the systematic error of this scaling procedure, and are the result of varying the green line within its parameter errors.

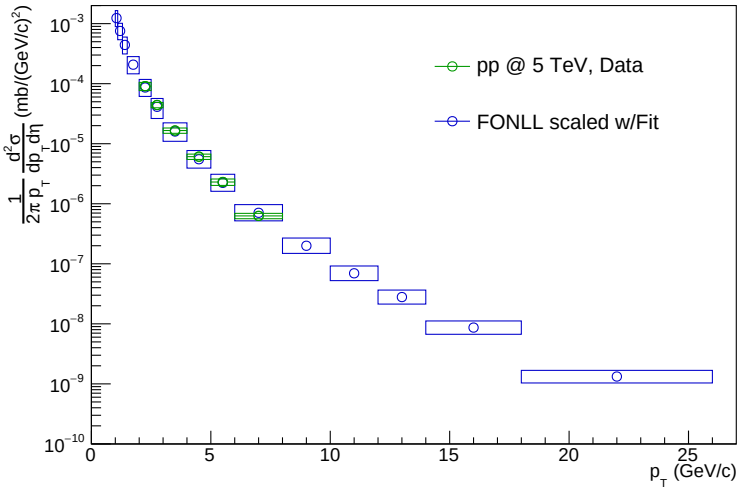

Figure 3.27: The data pp reference for low-p_{T} (green) and the FONLL cross-section scaled to match the low-p_{T} reference.

Chapter 4: Systematics and MC Closure Tests

In this chapter, the procedures and tests used to estimate the systematic uncertainties of the analysis methods are discussed. For many of the potential sources of uncertainty, the cut variation method was used; the selection criteria were varied by a reasonable amount and the effect on the final yield of beauty-decay electrons was examined. When this course of action was impossible, MC closure tests were used instead to estimate the uncertainty.

The checks done to look for systematic uncertainties are organized into seven sections. Section 4.1 details the potential uncertainty from the track reconstruction. Sections 4.2 and 4.3 include the uncertainties due to the data-driven hadron and photonic electron removal. Section 4.4 discusses the uncertainty from the W decay electron background. Section 4.5 details the potential uncertainties introduced by the corrections to the MC templates. Finally, Sections 4.6 and 4.7 detail the variations and closure tests used to make sure the fitting routine is robust and produces reasonable errors. From these studies, a p_{T}-dependent systematic uncertainty of 24-16% (18-14%) was assigned for the beauty electron yield in 0-10% (30-50%) Pb-Pb collisions. See Table 4.1 for a summary of the systematic uncertainties. The uncertainty on the pp reference used to calculate the R_{AA} is discussed in Section 3.7.

4.1 Track reconstruction

The systematic uncertainty due to track reconstruction was estimated by varying the required number of TPC clusters for the tracks. The variations tested were 70, 90, and 100 clusters (the number used in this analysis is 80). For each variation, the analysis was repeated and the beauty-decay electron yield compared to the yield with the default TPC cluster requirement. The differences are shown in Figure 4.2 for the 30-50% centrality results. The systematic uncertainty assigned from this procedure was 2% in semi-central collisions. In central collisions, the variation was negligible.

Source	0-10%		30-50%	
D weight	1% (p_T<20 GeV/c)	5% (p_T>20 GeV/c)	1%	
B weight	10% (p_T<6 GeV/c)	3% (p_T>6 GeV/c)	10% (p_T<6 GeV/c)	5% (6<p_T<8 GeV/c)
D^0 ratio correction	5%		2%	
PID	7% (p_T<12 GeV/c)	10% (p_T>12 GeV/c)	5% (p_T<6 GeV/c)	8% (p_T>6 GeV/c)
TPC nClusters	negligible		2%	
Hadron E/p scaling region	1% (p_T<12 GeV/c)	3% (p_T>12 GeV/c)	2% (p_T>8 GeV/c)	
Hadron scale factor error	4% (p_T>8 GeV/c)		4% (p_T>8 GeV/c)	
non-HFe subtraction	Partner e cuts: 2% (3<p_T<4 GeV/c)		Partner e cuts: 6%	
	Tagging efficiency: 2%		Tagging efficiency: 2%	
Fitting consistency	negligible		5%	
non-HFe Closure Test	20% decreasing to 6% with p_T		10% decreasing to 2% with p_T	
W contribution	5% (18<p_T<26 GeV/c)		5% (18<p_T<26 GeV/c)	
Total	24% decreasing to 16% with p_T		18% decreasing to 14% with p_T	

Figure 4.1: A summary of the systematic uncertainties of the beauty-decay electron yield in Pb-Pb collisions.

4.2 Hadron background removal

In this section, the systematic checks on the hadron background estimation are discussed. The hadron contamination estimation was tested by 1) varying the electron identification cuts and 2) varying the E/p scaling factor used to normalize the hadron DCA distribution.

Varying the electron identification selections increases and decreases the hadron contamination to be subtracted from the sample, providing a good stress test of the hadron subtraction method. It also tests the procedure used to calculate the efficiency of the electron identification selections. In this case, the E/p, M20, and $n\sigma_{TPC-dE/dx}$ selections used to identify electrons were varied. With these variations, it was challenging to separate true systematic shifts from statistical fluctuations and decide which variations to take into account. Thus, only the variations which resulted in differences greater than $\sim 1.5\sigma$ were included in the systematic uncertainty estimation. Here, σ was approximated as $\sqrt{\sigma_{var}^2 - \sigma_{default}^2}$, where $\sigma_{default}$ and σ_{var} are the statistical uncertainties of the beauty-decay electron yield with the default and varied electron selections. The different variations considered are listed in Table 4.2.

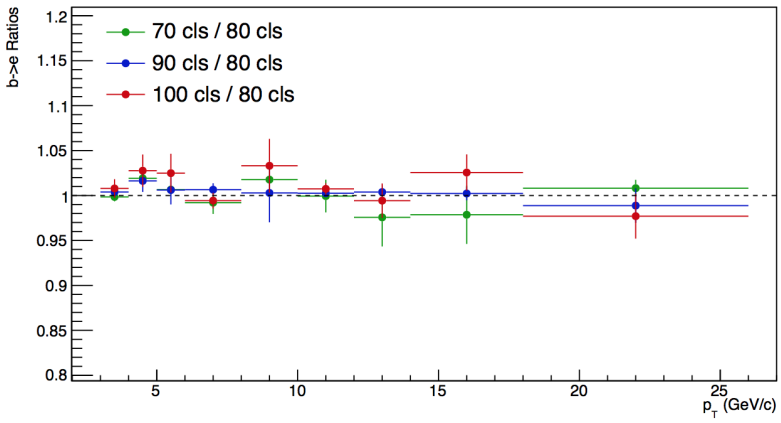

Figure 4.2: The ratio of the beauty-decay electron yield obtained after varying the number of TPC clusters compared to the default (80 clusters).

The uncertainty related to the electron selection variations in 0-10% centrality were 7% for $p_{\mathrm{T}} < 12$ GeV/c and 10% above. In 30-50% centrality, the uncertainty was 5% for $p_{\mathrm{T}} < 6$ GeV/c and 8% above. An example of the effect of these variations for 30-50% semi-central collisions is shown in Figure 4.3.

Table 4.1: Variations of the electron identification requirements, 0-10%

min E/p	min $n\sigma_{\mathrm{TPC-dE/dx}}$	max M20, 0-10%
0.9	-1	0.35
0.8	-0.5	0.35
0.8	-1	0.3
0.8	-1	0.4
0.9	-1	0.4

Table 4.2: Variations of the electron identification requirements, 30-50%

min E/p	min $n\sigma_{\mathrm{TPC-dE/dx}}$	max M20
0.8	-1	0.3
0.8	-1	0.4
0.8	-1.5	0.35
0.9	-1	0.35
0.9	-1	0.4

The procedure to estimate the amount of hadron contamination using the hadron and electron candidate E/p distributions was also varied to estimate systematic un-

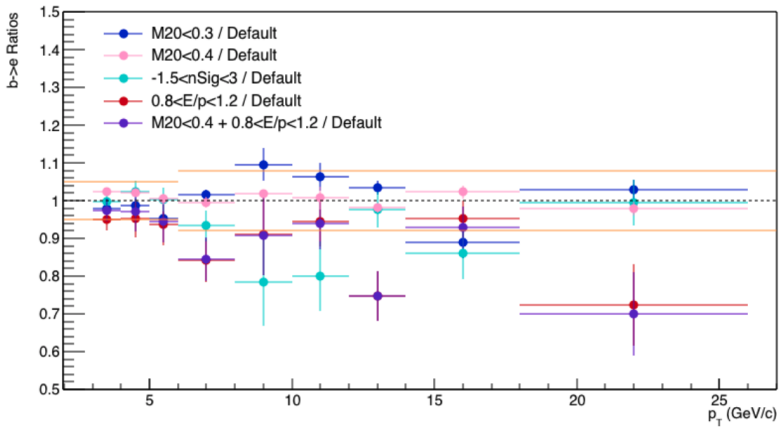

Figure 4.3: The ratio of the beauty-decay electron yields in 30-50% centrality with different variations of the E/p, $n\sigma_{TPC-dE/dx}$, and M20 electron selection criteria to the default values.

certainty. The hadron E/p distribution is scaled so that its integral in a specific E/p range matches that of the electron candidates. This range, referred to as the "E/p scaling region," was shifted by ± 0.1 and the full analysis was repeated to see the effect on the final beauty electron yield. An illustration of this scaling region shift is shown in Figure 4.4. From this variation, a systematic uncertainty of 1-3% was assigned, depending on the centrality and p_{T}.

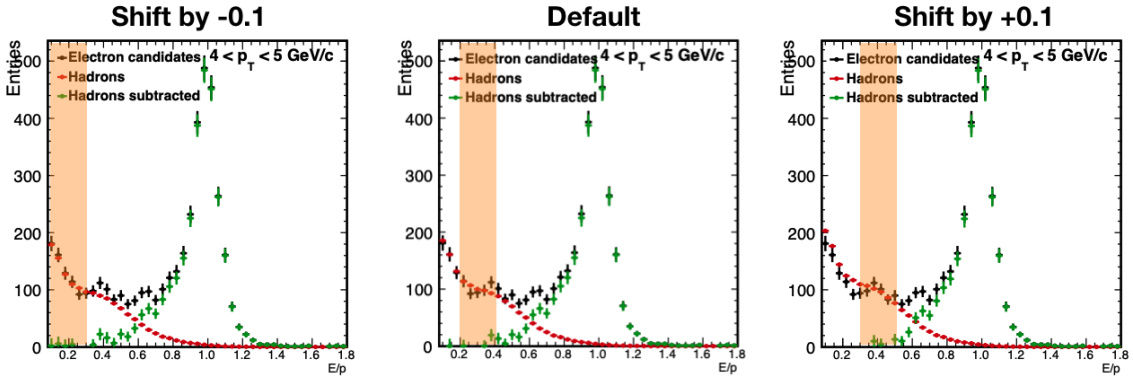

Figure 4.4: Illustration of shifting the scaling region for $4 < p_{\mathrm{T}} < 5$ GeV/c in 30-50% centrality. The scaling region is highlighted in yellow.

The factor used to scale the hadron E/p ("scaling factor") can be expressed as

follows:

$$\text{Scaling factor} = \frac{\text{Integral of electron candidate } E/p \text{ in scaling region}}{\text{Integral of hadron } E/p \text{ in scaling region}} \tag{4.1}$$

To further test the hadron scaling factor procedure, this scaling factor was varied according to its statistical uncertainty, propagating the errors of both the numerator and denominator of the equation. An example of the effect of this variation on the beauty-decay electron yield is shown in Figure 4.5 for 30-50% centrality. The low-p_{T} results are not affected by the variation, as the hadron contamination in that region is very low. Two straight lines were fitted to the data for low- and high-momentum separately to see the general trend. From the fit lines, a 4% systematic uncertainty was assigned for the high-momentum range $p_{\mathrm{T}} > 8$ GeV/c (Table 4.1, "Hadron scaling factor").

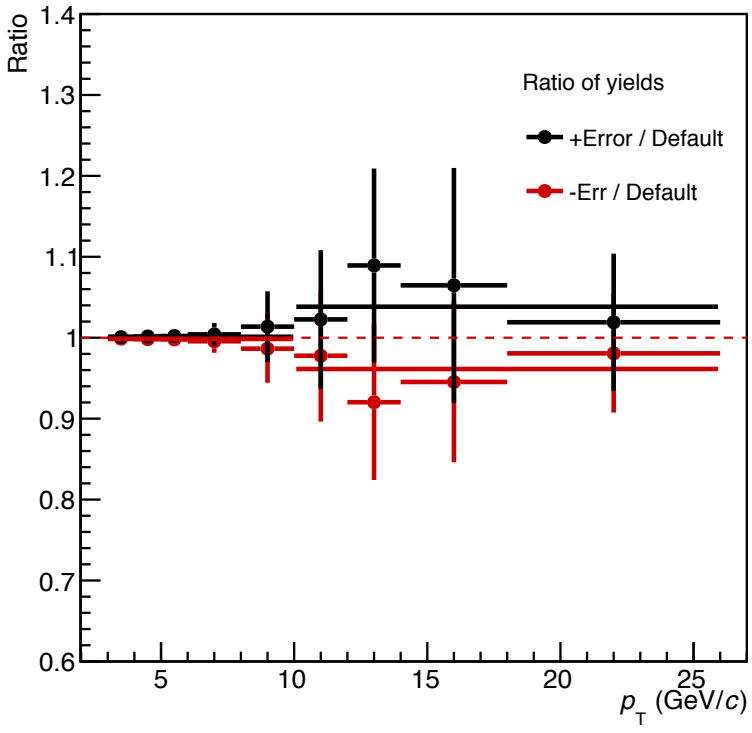

Figure 4.5: The beauty-decay electron yield results after varying the hadron E/p scaling factor within its statistical uncertainty. Lines have been fitted to the ratio for $p_{\mathrm{T}} < 10$ GeV/c and $p_{\mathrm{T}} > 10$ GeV/c.

Finally, variations of the hadron $n\sigma_{\mathrm{TPC}} < -4$ selection were performed to see if it has a systematic effect on the final results. The concern was that this selection

contains protons and kaons as well as pions, when the true contamination in the electron sample is mostly pions (see Figure 3.18). It may be that the E/p and DCA of the pions contaminating the electron sample has a different shape than the combination of hadrons selected with the $n\sigma_{\mathrm{TPC}} < -4$ criterion. The alternative $n\sigma_{\mathrm{TPC}}$ selections tested are listed in Table 4.3. The effect on the beauty electron yield was negligible, so no systematic uncertainty was assigned based on the hadron selection criteria.

Table 4.3: Hadron $n\sigma_{\mathrm{TPC}}$ selection variations

Variation	$n\sigma_{\mathrm{TPC}}$ cut
Default	$n\sigma_{\mathrm{TPC}} < -4$
Widened cut	$n\sigma_{\mathrm{TPC}} < -3.5$
Pion-rich	$-4.5 < n\sigma_{\mathrm{TPC}} < -3.5$
Proton/kaon rich	$-6.5 < n\sigma_{\mathrm{TPC}} < -4.5$

4.3 Photonic Electron Subtraction

The invariant mass method of estimating the photonic electron contribution was varied by 1) changing the partner electron selection criteria and 2) recalculating the tagging efficiency for the individual sources of photonic electrons (γ, π^0, and η). Finally, the invariant mass method was tested using a closure test, described in Section 4.3.1.

First, the partner electron criteria used in the invariant mass method of identifying photonic electrons were varied. The default criteria are $p_{\mathrm{T}} > 0.3$ GeV/c and $n\sigma_{\mathrm{TPC-dE/dx}} > -3$, and the variations increase and decrease the minimum p_{T} and $n\sigma_{\mathrm{TPC-dE/dx}}$. The ratio of the beauty electron yield with the variations divided by the default yield is shown in Figure 4.6. Based on the mean and spread of values obtained with the partner electron variations, a systematic of 2% (6%) was assigned in central (semi-central collisions).

In addition to varying the partner electron criteria, the photonic electron tagging efficiency calculation was repeated to see whether it is different for different sources of photonic electrons (γ, π^0, and η). Their individual tagging efficiencies vary slightly, as can be seen in Figure 4.7. To account for this difference, the final beauty-decay electron yield was recalculated using the three tagging efficiencies (from each source).

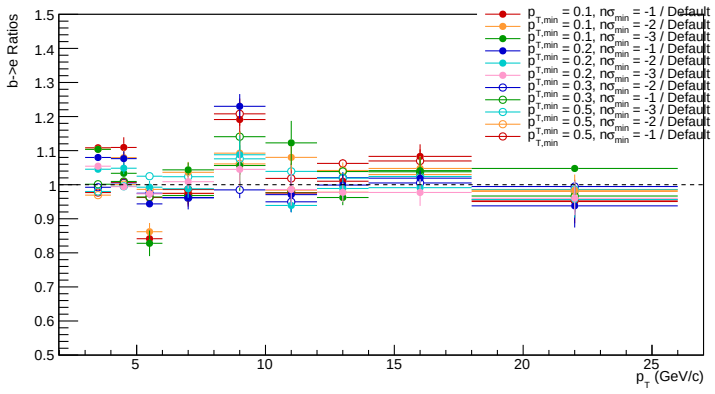

Figure 4.6: The difference in beauty-decay electron yield when the min p_{T} and $n\sigma_{\mathrm{TPC-dE/dx}}$ requirement for the partner electron are varied in 30-50% centrality.

The effect can be seen in Figure 4.8; a 2% systematic was assigned to account for the tagging efficiency variation.

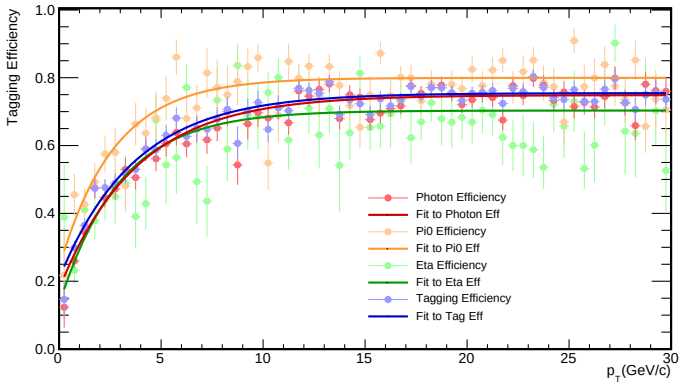

Figure 4.7: The tagging efficiencies of electrons from the different photonic electron sources: γ (red), π_0 (gold), and η (green). The total (default) tagging efficiency is in blue.

4.3.1 Photonic electron closure test

Photonic electrons can be produced via conversion processes in the detector medium, so their production radii from the primary vertex can vary over a relatively wide

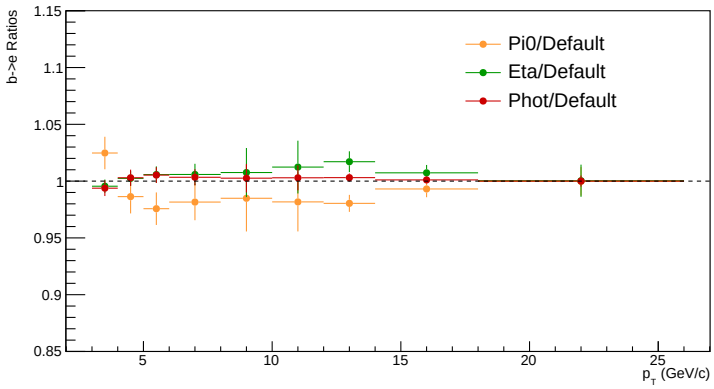

Figure 4.8: The variation in the beauty yield when the tagging efficiency of the individual sources of photonic electrons are used. The gold distribution corresponds to considering only the π^0 electrons, the green to η electrons, and the red to γ electrons.

range. This can be seen in Figure 4.9, where the production radius distribution of photonic electrons in MC simulations is shown. The peak at r = 0 corresponds to photonic electrons from Dalitz decays, since the mother π^0 and η mesons are short-lived. The other peaks correspond to the position of the beam pipe and ITS detector layers, where photonic electrons from conversion processes are produced.

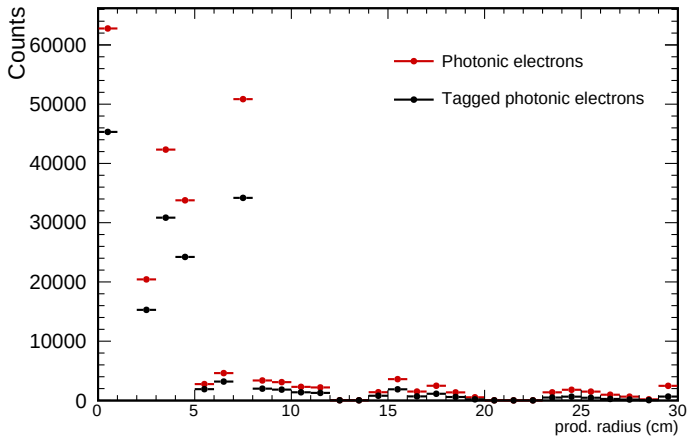

Figure 4.9: The production radius (in cm) of photonic electrons in 0-10% MC simulations. All photonic electrons are in red, photonic electrons "tagged" using the invariant mass method are in black.

Photonic electrons with small production radii tend to have a small DCA, while

those produced deeper in the detector material have a large DCA. Thus, it is important to check whether the method of obtaining the photonic electron DCA preferentially selects photonic electrons based on their production radius. This could cause a bias in the shape of the photonic electron DCA.

To check this, the photonic electron tagging efficiency was calculated as a function of the production radius (Figure 4.10). There is a large dependence; the efficiency decreases from around 70% at small production radii to almost 20% at r = 30 cm. The obvious solution would be to apply the tagging efficiency as a function of both p_{T} and the production radius; however, the production radius of electrons in data is unknown, so this solution cannot be implemented.

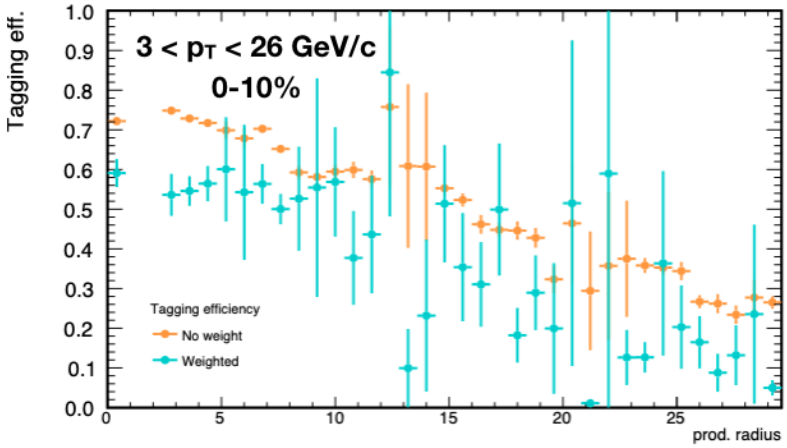

Figure 4.10: The photonic electron tagging efficiency as a function of production radius (in cm). The blue distribution is after applying the π_0 and η weights described in Section 3.3.3.2.

Instead, the possible effect of the production radius bias is estimated using a "MC closure test." A closure test involves repeating the analysis steps in a MC sample and seeing whether the method reproduces the true value. In this case, the invariant mass method of estimating the photonic electron yield and DCA was performed in the MC sample and compared with the true photonic electron yield and DCA. It was found that although the photonic yield matched the true yield within 5% (Figure 4.11), the photonic electron DCA produced using the invariant mass method was much narrower than the true distribution. This can be seen in Figure 4.11, where the DCA distribution obtained using the invariant mass method is divided by the true DCA.

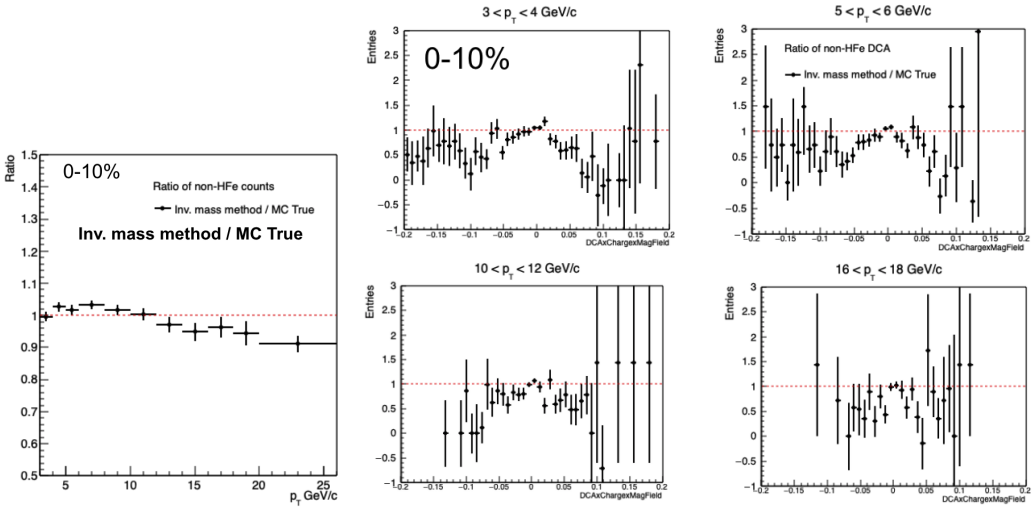

Figure 4.11: Left: The photonic electron yield in a MC sample calculated using the invariant mass method compared with the true yield. Right: Ratio of the photonic electron DCA distribution obtained using the invariant mass method divided by the true distribution. The DCA distributions were not normalized before dividing.

To estimate the ultimate effect on the beauty-decay electron yield, this closure test was extended to include the fitting procedure. The steps are as follows: the true photonic electrons were combined with true charm- and beauty-decay electrons such that the fraction of photonic electrons to heavy-flavor electrons roughly matches what is estimated in data (Figure 4.12). Then, the photonic electron DCA distribution obtained using the invariant mass procedure in the MC sample was subtracted from the combined true photonic and heavy-flavor DCA. Finally, the beauty-decay electron yield was obtained by fitting with templates and compared with the true beauty-decay electron yield. The ratio of the two is shown in Figure 4.13. To extract the p_{T}-dependent systematic uncertainty, this ratio was fitted with Equation 4.2.

$$f(p_{\mathrm{T}}) = P_0 + e^{(P_1 + P_2 \cdot p_{\mathrm{T}})} - 1 \tag{4.2}$$

The resulting parameters are listed in Table 4.4. In 0-10% collisions, the systematic uncertainty is 20% at $p_{\mathrm{T}} = 3$ GeV/c and decreases to 6% at high momentum. In 30-50%, the uncertainty is smaller: 10% at $p_{\mathrm{T}} = 3$ GeV/c and decreasing to 2% with increasing momentum.

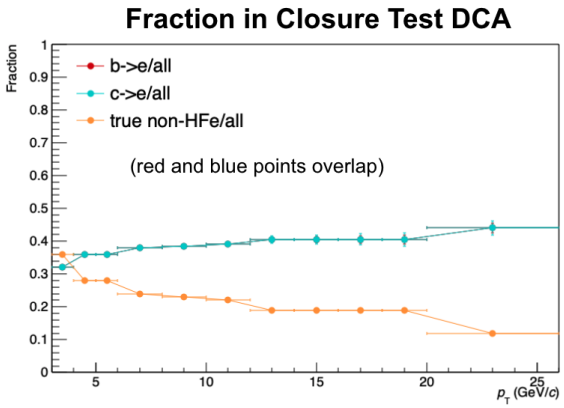

Figure 4.12: Fraction of the beauty-decay (red), charm-decay (cyan), and photonic electrons (gold) combined for the photonic electron closure test.

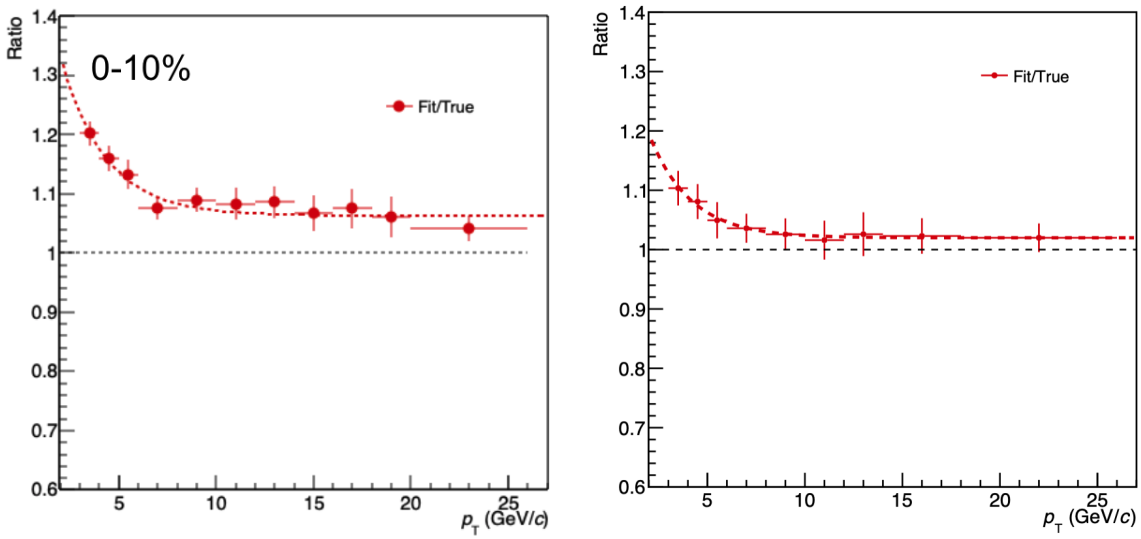

Figure 4.13: Ratio of the photonic electron DCA distribution obtained using the invariant mass method divided by the true distribution. Left: 0-10% centrality. Right: 30-50% centrality.

4.4 W background

At high-momentum, the background source of electrons from W decays is no longer negligible. From previous studies [53], the contribution is estimated to be 20% at $p_{\mathrm{T}} = 26$ GeV/c, though it falls quickly as one goes to lower momenta. To estimate the potential effect of the W background on this analysis, a closure test was performed

Table 4.4: Fit parameters used for the systematic uncertainty from the photonic electron closure test

Parameter No.	0-10%	30-50%
0	1.06307	1.01994
1	-0.442010	-0.802139
2	-0.433046	-0.471058

(similar to the one described in Section 4.3.1). In this test, the DCA of heavy-flavor decay electrons combined with Dalitz decay electrons were fitted with the charm and beauty templates and the fit result compared with the true beauty-decay election yield. In this case, the Dalitz decay electrons served as a proxy for W decay electrons, since both W bosons and π^0 and η mesons decay close to the primary vertex and generate very narrow electron DCA distributions. (The decay lengths of the W, π^0, and η are approximately 9.5×10^{-8}, 25.5, and 0.15 nm respectively.) The fraction of electrons from Dalitz decays included in the sample is shown on the left in Figure 4.14 and is consistent with the W decay electron fraction in [53].

A comparison of the fit results and the true beauty-decay electron yield is shown on the right in Figure 4.14. Though the W decay electron fraction is quite large in the final p_{T} bin, the effect on the beauty-decay electron measurement is less than 5%. To account for this small effect, an additional 5% systematic uncertainty was assigned for $18 < p_{\mathrm{T}} < 26$ GeV/c.

4.5 MC Template Corrections

A number of corrections need to be applied to the templates because the MC sample differs from data, as discussed in Section 3.4.2. This includes applying weights to correct the p_{T} distributions of the mother B and D mesons of the electrons and correcting the ratio of the different mother charm species in the charm templates. To estimate the systematic uncertainties of the template corrections, the D meson weight, B meson weight, and the ratio of the different charm species were varied. The B meson weighting relies on the choice of the theoretical prediction used to estimate the B meson R_{AA}. To cover a reasonable range of possible values, the TAMU [147] B meson R_{AA} was varied by adding half the difference from unity: $R_{\mathrm{AA}}^{Var} = R_{\mathrm{AA}}^{TAMU} \pm 0.5 \cdot (1 - R_{\mathrm{AA}}^{TAMU})$. The variation in the TAMU prediction is shown

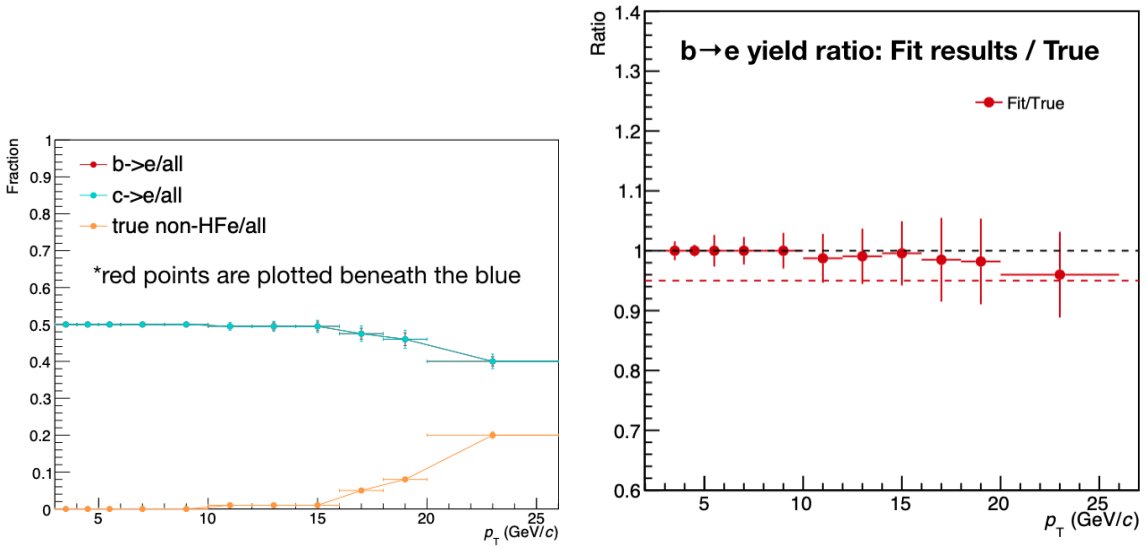

Figure 4.14: Left: Fraction of Dalitz-decay electrons (used as a W decay electron proxy) used in the closure test to estimate the effect of the W decay electron background. Right: The effect of the W decay background on the beauty-decay electron yield in the closure test.

at the top of Figure 4.15 for both 0-10% and 30-50%. An example of the effect on the beauty-decay electron yield is shown at the bottom of the figure for 0-10% centrality. The uncertainty assigned to the beauty-decay electron yield due to the B meson weighting procedure is 10% for $p_{\mathrm{T}} < 6$ GeV/c in both centrality ranges. In 0-10% centrality, the uncertainty is 3% for $p_{\mathrm{T}} > 6$, and in 30-50% centrality, the uncertainty is 5% for $6 < p_{\mathrm{T}} < 8$ GeV/c. The B meson weight is one of the largest sources of systematic uncertainty at low p_{T} (< 6 GeV/c).

To test the systematic uncertainty of weighting the D meson spectrum in the charm template, the D meson weight is "tilted" within the error bars of the D^0 meson data measurement [36]. In other words, the slope of the measurement is changed as much as possible while staying within the error bars (systematic and statistical errors added in quadrature). The variation of the D^0 meson data measurement can be seen in Figure 3.13. The ratio of the beauty-decay electron yield with these variations can be seen in Figure 4.16. In central collisions, a systematic uncertainty of 1% was assigned for $p_{\mathrm{T}} < 20$ GeV/c and 5% for higher p_{T}. In semi-central collisions, a flat 1% uncertainty was assigned for the D meson weight procedure.

The charm template also includes corrections so that the $\frac{\Lambda_c}{D^0}$, $\frac{D_s}{D^0}$, and $\frac{D^+}{D^0}$ of the

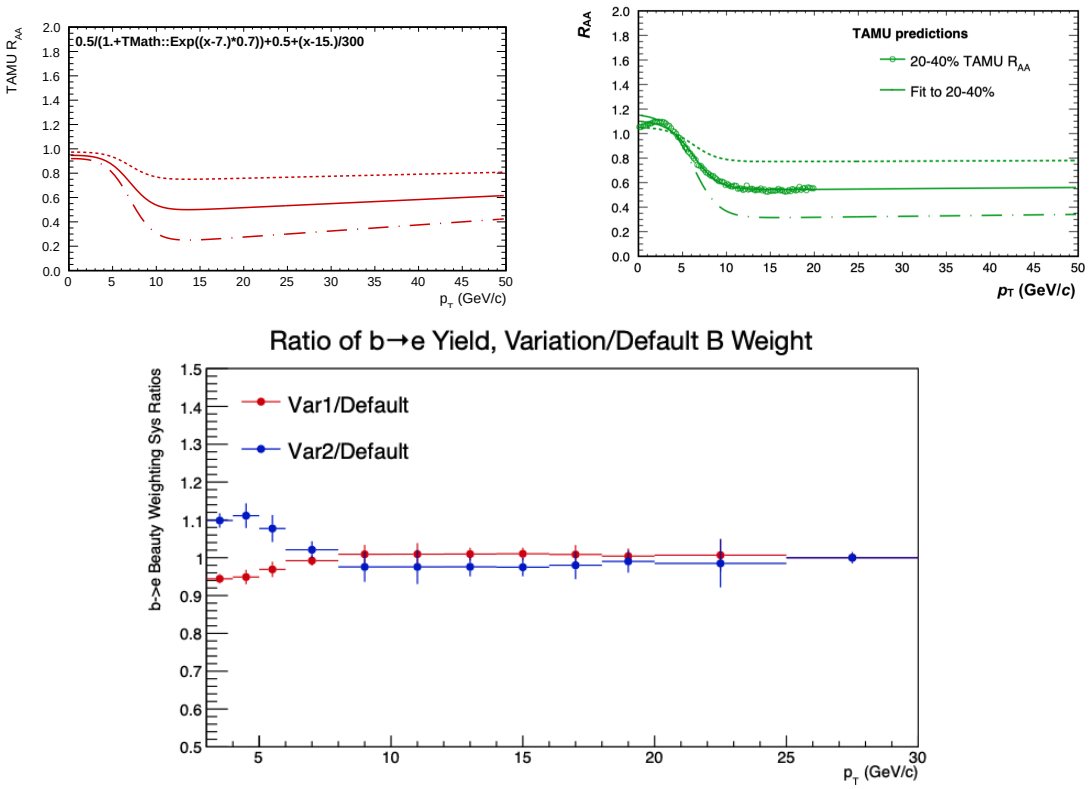

Figure 4.15: Top: Variation of the 0-10% (20-40%) TAMU B meson R_{AA} used for the 0-10% (30-50%) beauty electron yield systematics. Bottom: The ratios of the beauty-decay electron yield used for the B weight systematic uncertainty estimation in 0-10% centrality.

electron mothers in the charm template match what is seen in data measurements with ALICE. The $\frac{D_s}{D^0}$ and $\frac{D^+}{D^0}$ data measurements are roughly constant in p_{T}, so a flat line is fit to the data and a single value used for the charm templates in the full p_{T} range. To obtain the systematic uncertainty, the value obtained from the fit are varied according to the error of the fit parameters (see Figure 3.16). In the case of the $\frac{\Lambda_c}{D^0}$, the fraction value was varied between 0.79 and 1.39 according to the uncertainty of the $\frac{\Lambda_c}{D^0}$ measured by ALICE in [149]. These ratios in the charm templates were varied individually and in tandem, and the effect on the beauty-decay electron yield was used to estimate the systematic uncertainty. Figure 4.17 shows an example of the effect on the 30-50% semi-central measurement. From the spread in the variations, a systematic uncertainty of 5% (2%) was assigned for central (semi-central) collisions.

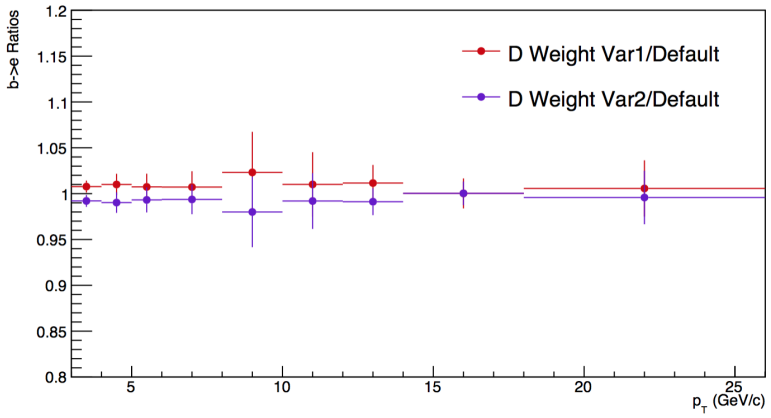

Figure 4.16: Effect of varying the D meson weight used in the charm templates on the 30-50% beauty-decay electron yield.

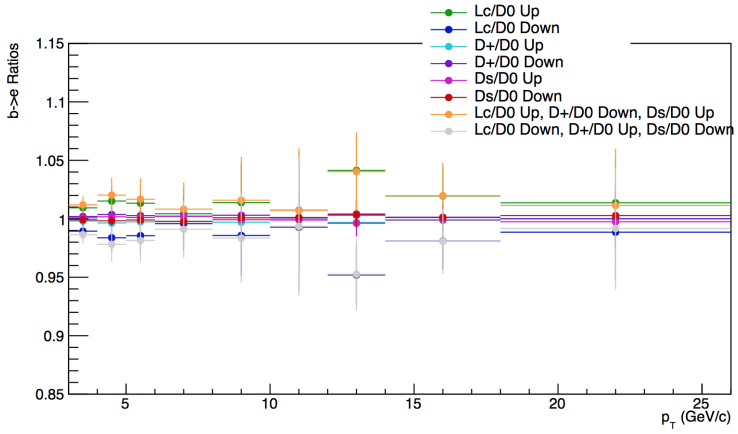

Figure 4.17: Effects of varying the D^0 ratio corrections in the charm template on the 30-50% beauty-decay electron yield.

4.6 Fit stability

The fitting routine was also varied to test for potential sources of systematic uncertainty. These include the effect of using different DCA binning sizes and different DCA fit ranges (Figure 4.18). The default bin size in this analysis is 0.002 cm, and was varied to 0.0005, 0.001, 0.004, and 0.008 cm to test the stability of the fit. The fit range was varied by fitting in the central part of the DCA distribution, rather than in the full range of $-0.2 < DCA < 0.2$. The fit range variations are $-0.1 < DCA < 0.1$

cm and $-0.15 < DCA < 0.15$ cm . In 0-10% centrality, the effect of these variations on the beauty-decay electron yield was negligible. In 30-50%, a systematic uncertainty of 5% was assigned based on the spread of the beauty-decay electron yields obtained with the varied bin sizes and fit ranges.

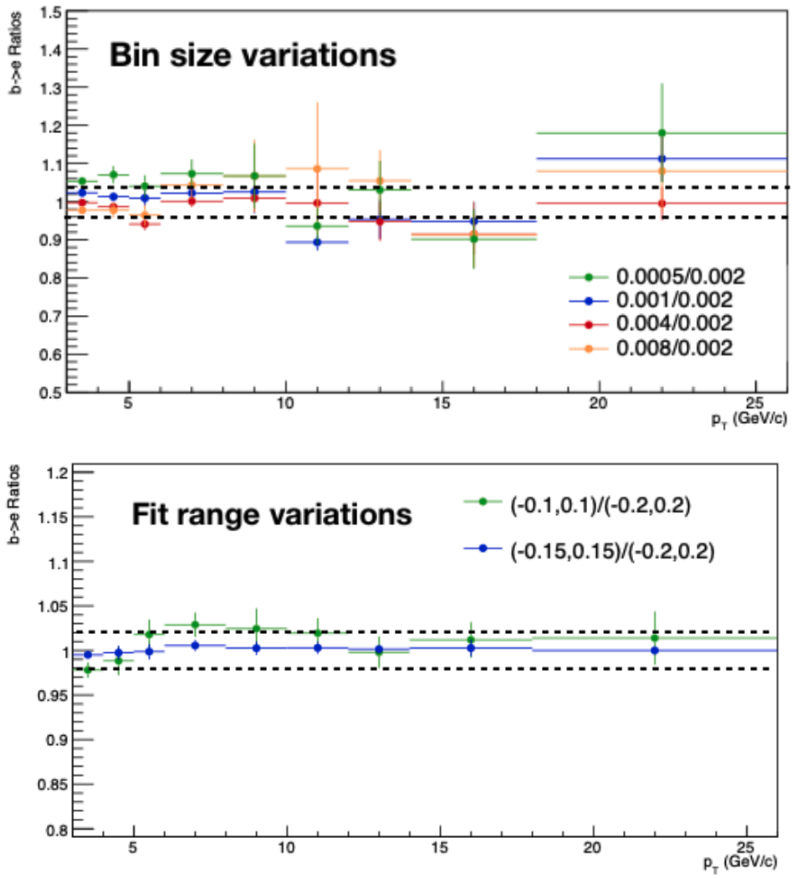

Figure 4.18: Effects of varying the DCA bin size and the DCA fit range in 30-50% on the beauty-decay electron yield.

4.7 Weighted Log-likelihood Fit & Errors

As mentioned in Section 3.4, a weighted log-likelihood fit was performed to fit the templates to the heavy-flavor electron DCA distribution. To test this fitting method, several closure tests were performed; heavy-flavor electron DCA distributions were created using MC with a known beauty contribution. These DCA distributions were

then fitted with the templates using the weighted log-likelihood fit, and the results evaluated against the true number of beauty-decay electrons.

The heavy-flavor DCA distributions produced had a similar number of entries as minimum bias data, reproducing some of the statistical fluctuations of the true measurement. The beauty- and charm-decay electrons were weighted according to their mother p_{T} and the D^0 ratio corrections were applied (the same corrections that are applied to the templates). In addition, the charm electron contribution was scaled in such a way that the beauty-decay electron over heavy-flavor decay electron ratio was roughly 50%. The fit results are compared with the true beauty electron number in Figure 4.19. There, one can see that the ratio of the two is consistent with unity within the error bars, which are given by the fit parameter uncertainty. This test was repeated with higher fraction of beauty-decay electrons (60%) and the results were also consistent with the true yield (see Figure 4.19).

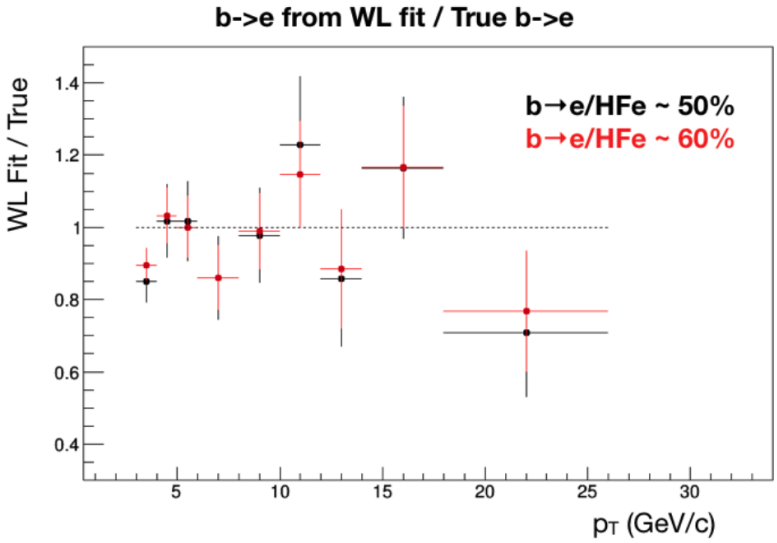

Figure 4.19: The fit results of the closure test compared to the true number of beauty electrons. The black (red) points are from a closure test in which 50% (60%) of the heavy-flavor electrons were from beauty decays.

The final test was to repeat the closure test with separate sub-sets of the MC sample and see if the parameter uncertainties given by the fits are reasonable given the spread of values. This was done for three sub-sets with no overlap of the simulated events. Each sample had a similar number of events, and the beauty and charm

electrons were added such that the beauty electron fraction was about 50%. The results are compared with the true beauty-decay electron yield on the left in Figure 4.20.

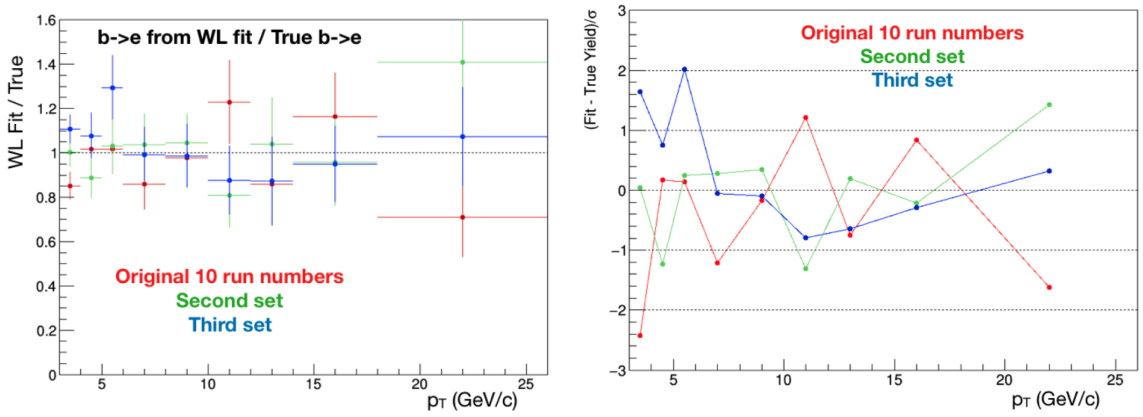

Figure 4.20: Left: The fit result/true number of beauty electrons for each of the closure test trials. Right: The difference in the fit yield to the true beauty-decay electron yield, divided by the fit parameter uncertainty.

The results of the fit of all three samples/trials are reasonably consistent with the true number of beauty electrons. To see whether the errors from the fit are reasonable, the (fit yield - true yield)/σ was calculated and is shown on the right in Figure 4.20. In this case, the σ is the parameter uncertainty given by the fit routine. In this test, we see that 18 points (66.7%) are within 1σ and 25 points (92.6%) are within 2σ. This is roughly what one would expect, and gives a sanity check for the error bars given by the weighted log-likelihood fit.

Chapter 5: Results

In this chapter, beauty production, measured via the beauty-decay electron yield in Pb-Pb collisions at $\sqrt{s_{\rm NN}} = 5.02$ TeV will be presented along with the nuclear modification factor calculated using the pp reference detailed in Section 3.7. The results will be compared with other measurements and theoretical models.

5.1 Beauty-hadron decay electron yield

Figure 5.1 shows the beauty-decay electron yield in 0-10% central collisions and 30-50% semi-central Pb-Pb collisions. The measurement is performed using minimum-bias triggered data for $p_{\rm T} < 12$ GeV/c and EMCal-triggered EG1 data at higher momentum. With the two triggers, the measurement extends from $p_{\rm T} = 3$ GeV/c to 26 GeV/c, reaching a higher momentum than previous studies. (Past measurements of beauty-decay electrons only reached $p_{\rm T} = 8$ GeV/c [45].) The measurement is also shown here for the first time in two separate centrality ranges (0-10% and 30-50%), where the previous measurement in ALICE was performed in 0-20% alone. This allows us to test whether the energy loss of the beauty quark is dependent on the centrality of the collision.

Included in Figure 5.1 is a preliminary measurement (black) of the beauty-decay electron yield at low momentum ($2 < p_{\rm T} < 8$ GeV/c) in 0-10% centrality, also performed in Pb-Pb collisions at $\sqrt{s_{\rm NN}} = 5.02$ TeV using the ALICE detector. In this measurement, the electrons were identified using information from the TPC and TOF detector [150], which is better suited for measurements of low-momentum electrons. This measurement is complementary to the work performed in this thesis, which used the TPC and EMCal detectors. The TPC-TOF measurement had a slightly different analysis procedure than the one described in this thesis, using four MC templates to extract the beauty contribution to the total electron DCA. This procedure was also used in the previously published ALICE measurement at $\sqrt{s_{\rm NN}} = 2.76$ TeV, discussed in Section 5.2.1.

The measurement performed in this thesis is in good agreement with the TPC-TOF results in the region of overlap ($3 < p_{\rm T} < 8$ GeV/c), despite the difference in the

particle identification detectors and analysis methods. Taking the two measurements together extends the p_{T} reach even further to cover the range $2 < p_{\mathrm{T}} < 26$ GeV/c.

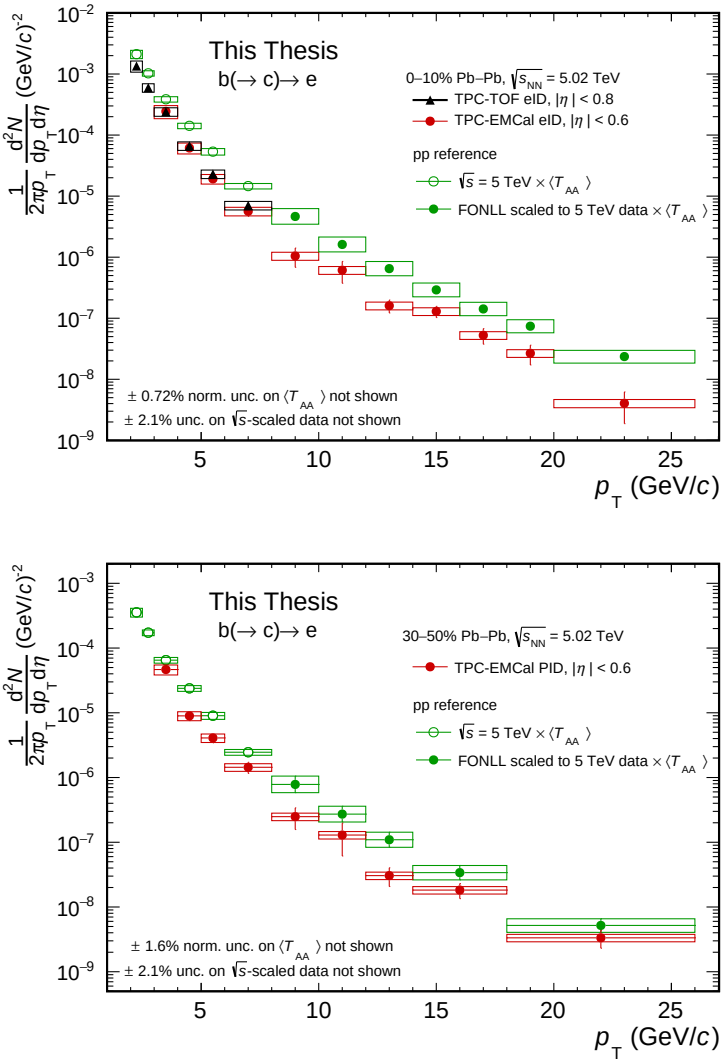

Figure 5.1: The momentum distribution of beauty-decay electrons (red) and pp reference (green) in 0-10% central collisions (top) and 30-50% semi-central collisions (bottom) from this thesis. The black distribution in 0-10% is the beauty-decay electron yield measured using the TPC and TOF detectors.

5.2 Nuclear modification factor: Energy loss in the QGP

As discussed in Section 1.6, the nuclear modification factor $R_{\rm AA}$ compares the momentum distribution of particles in heavy-ion collisions with the momentum distribution of the same particle in pp collisions. If beauty quarks lose energy as they traverse the QGP in a heavy-ion collision, their momentum distribution will be shifted to lower values w.r.t pp collisions, where a QGP is not formed. This would translate to an observed suppression of beauty-decay electrons in heavy-ion collisions, and an $R_{\rm AA} < 1$.

In order to calculate the $R_{\rm AA}$, the beauty-decay electron yield is divided by a "pp reference," which is also shown in Figure 5.1. Below $p_{\rm T} = 8$ GeV/c, the pp reference is the cross-section of beauty-decay electrons measured in pp collisions at $\sqrt{s} = 5.02$ TeV. At higher momentum, the reference is adapted from FONLL predictions, as discussed in Section 3.7. In Figure 5.1, the pp reference cross section is already multiplied by $\langle T_{\rm AA} \rangle$, known as the nuclear thickness function. In 0-10% collisions, the $\langle T_{\rm AA} \rangle = 23.26 \pm 0.17$ mb^{-1}, while in 30-50%, the $\langle T_{\rm AA} \rangle = 3.917 \pm 0.065$ mb^{-1} [133]. The uncertainty of the $\langle T_{\rm AA} \rangle$ is not explicitly included in the error bars, but is noted at the bottom left of Figure 5.1. Since the $\langle T_{\rm AA} \rangle$ is already applied in the figures, the red and green distributions show the numerator and denominator of the $R_{\rm AA}$ respectively; all that remains is to divide:

$$R_{\rm AA} = \frac{dN_{\rm AA}/dp_{\rm T}}{\langle T_{\rm AA} \rangle \cdot d\sigma_{\rm pp}/dp_{\rm T}} \tag{5.1}$$

The resulting $R_{\rm AA}$ is shown in Figure 5.2 for both collision centralities considered (0-10% and 30-50%). The statistical and systematic uncertainties of the Pb-Pb and pp measurement are propagated as though they are uncorrelated. The pp reference normalization uncertainty (2.1%) is combined in quadrature with the $\langle T_{\rm AA} \rangle$ uncertainty and reported as boxes at unity.

Several things can be noted at the outset. For one, the production of beauty-decay electrons in Pb-Pb collisions is suppressed by about a factor of 2 with respect to pp collisions. This adds to the evidence of previous measurements that the beauty quark is suppressed and loses energy in the QGP (as discussed in Section 1.6.2.2).

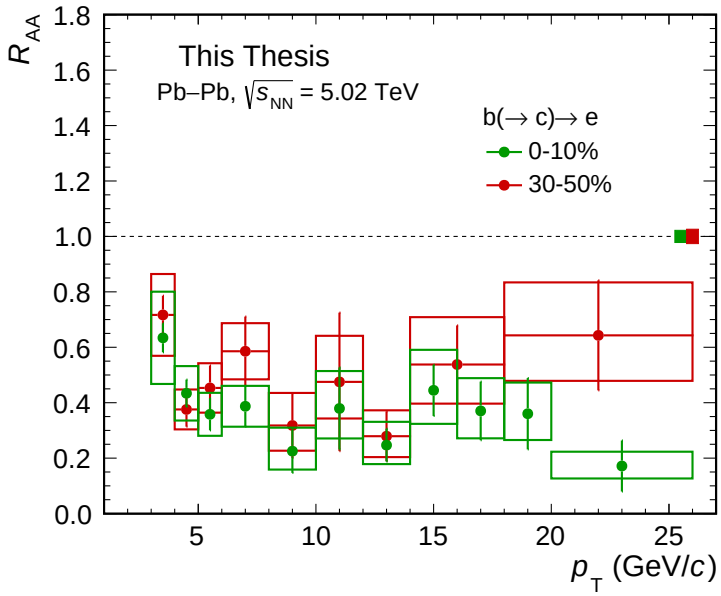

Figure 5.2: The beauty-decay electron R_{AA} in both 0-10% (green) and 30-50% (red) centrality.

Another trend seen here is that the beauty-decay electrons in 30-50% semi-central collisions (with $\sim$ 109 nucleons participating in the collision) appear to be less suppressed on average than in 0-10% central collisions (with $\sim$ 357 participants [133]). This may be due to the size of the QGP produced in these two types of collisions: the more off-center 30-50% collisions may produce a smaller QGP for the beauty quarks to travel through. However, the difference is not significant within the current errors of the measurement. This is, however, the first measurement of beauty-decay electrons using the EMCal to aid in electron identification and using data-driven methods to subtract the hadron contamination and photonic electron contributions to the DCA. Future measurements may be able to refine the methods to have less systematic uncertainty. Future studies can also determine the correlation of the systematic uncertainties in the 0-10% and 30-50% measurements. This would help quantify the R_{AA} differences in the two centrality classes.

The R_{AA} in 0-10% collisions measured in this thesis can be further extended using the TPC-TOF beauty-decay electron measurement mentioned in the previous section (Section 5.1). The R_{AA} obtained using the TPC-TOF method is shown in blue in Figure 5.3 along with the R_{AA} presented in this thesis in red. The two R_{AA} were

obtained using the same pp reference and $\langle T_{\mathrm{AA}} \rangle$ values. One can again see that the two measurements are in good agreement within the region of overlap from 3 to 8 GeV/c.

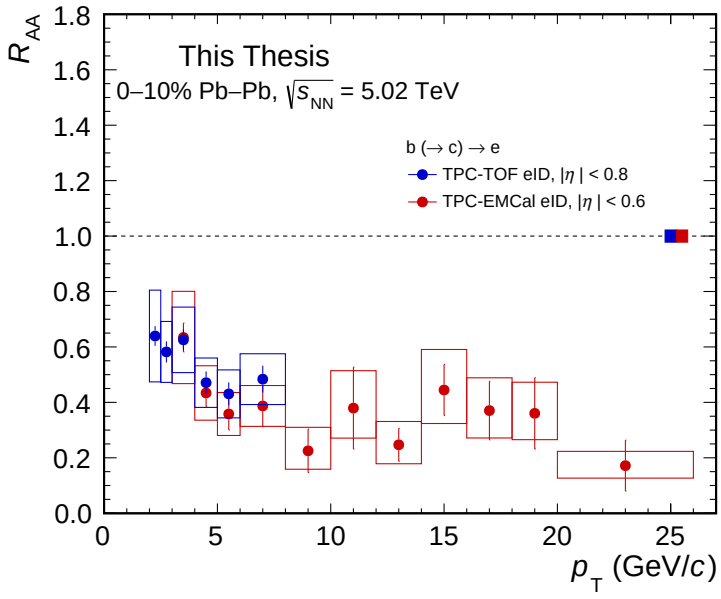

Figure 5.3: The beauty-decay electron R_{AA} in 0-10% from this thesis (red) compared with the beauty-decay electron R_{AA} obtained using the TPC and TOF detectors (blue).

5.2.1 Energy dependence: Comparison with 2.76 TeV

The previous measurement of beauty-decay electrons in Pb-Pb collisions performed with ALICE was at center-of-mass energy per nucleon pair of $\sqrt{s_{\mathrm{NN}}} = 2.76$, and was conducted for collisions in the 0-20% centrality range [45]. Therefore, it differs from this thesis measurement in both the energy of the collision (2.76 vs. 5.20 TeV) and the centrality. We can compare the two measurements to test the collision-energy and centrality dependence of beauty energy loss.

To disentangle these effects, it helps to consider what is expected from model predictions and past measurements. First, we expect that the difference in collision energy would only have a small effect on the R_{AA}. This trend has been seen for D mesons [36] and charged particles [151], where the R_{AA} at $\sqrt{s_{\mathrm{NN}}} = 2.76$ TeV and 5.02

TeV was consistent within uncertainties. The similarity of the R_{AA}'s across different collision energies was predicted by the Djordjevic model in [82]. In that model, the R_{AA} of beauty quarks would decrease by about 5% due to the increase in average medium temperature (which increases energy loss). However, this decrease is mostly canceled out by a change in the expected momentum distribution of beauty quarks at higher energy; the harder p_{T} distribution of beauty quarks would increase the R_{AA} by about 5%.

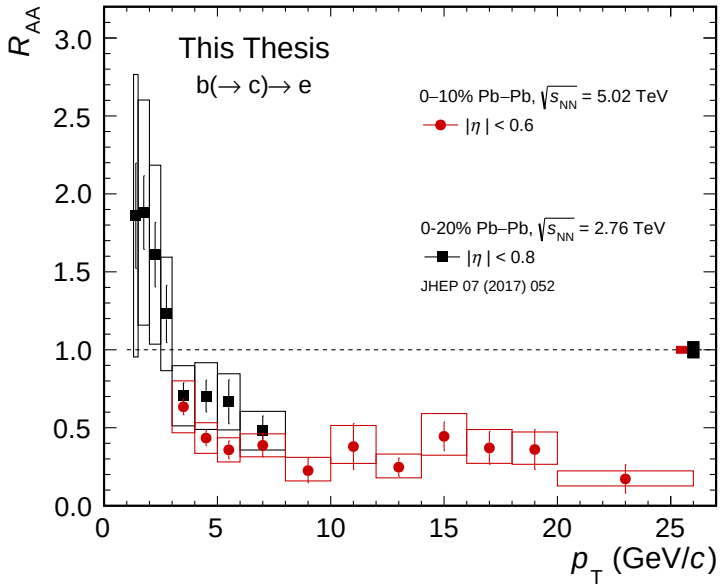

Figure 5.4: Comparison of the R_{AA} from this thesis with the previous ALICE measurement in 0-20% Pb-Pb collisions at $\sqrt{s_{\mathrm{NN}}} = 2.76$ TeV [45].

Since the difference in collision energy is expected to have a negligible effect, we can assume that any remaining deviations between the previous 2.76 TeV measurement and the 5.02 TeV measurement in this thesis are mostly due to differences in the centrality and the experimental methods. Figure 5.4 shows a comparison of the two measurements. In the limited overlap region, $3 < p_{\mathrm{T}} < 8$ GeV/c, the two analyses are consistent within uncertainties. The 0-10% points are slightly lower, but this is to be expected given the difference in centrality range. Thus, the analysis routine described in this thesis compares favorably with published results while allowing a wider range of momenta to be studied.

5.2.2 Mass dependence: Charm and beauty

As was discussed in Section 1.5, we expect that charm quarks will lose more energy in the QGP medium than beauty quarks due to the mass-dependence of the energy loss processes. Thus, we expect that the R_{AA} of beauty-decay particles will be higher than that of charm-decay particles. We can test this hypothesis by comparing this thesis measurement of beauty-decay electrons (b→e) with previous measurements of heavy-flavor decay electrons (from both charm and beauty decays: (c,b→e)) [53]. This is shown in Figure 5.5. It should be noted that this is *not* a direct comparison of beauty and charm, since the heavy-flavor decay electrons include a certain fraction of beauty-decay electrons.

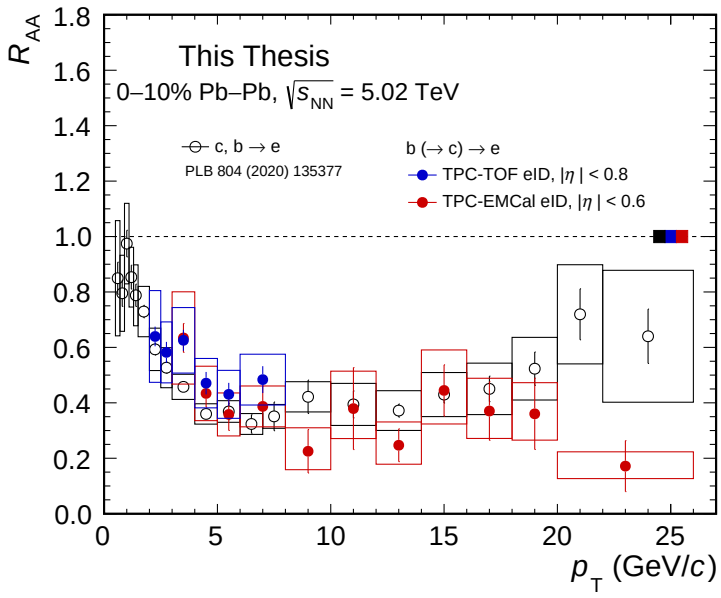

Figure 5.5: Comparison of the beauty-decay electron R_{AA} with previous ALICE measurements of heavy-flavor decay electrons [53].

Figure 5.5 shows a comparison of the beauty-decay electrons and heavy-flavor decay electrons in 0-10% collisions. In the plot, the TPC-TOF preliminary measurement of beauty-decay electrons is also included to extend the comparison to lower momentum. Though the error bars are large, one sees a hint that the beauty-decay electron R_{AA} in 0-10% collisions lies slightly higher than the combined charm- and beauty-decay electron R_{AA} at low momentum. At higher momentum, however, the

two are mostly overlapping, and consistent within the uncertainties.

The overlap at higher momentum is in keeping with theoretical expectations, and is caused by two factors. The first is that this measurement is not an exact comparison of charm and beauty; instead, we are comparing beauty-decay particles with a combination of both charm- and beauty-decay particles. If the beauty-decay electrons make up a large fraction of the heavy-flavor decay electrons, it would follow that the two nuclear modification factors would be similar. In fact, it is likely that the fraction of beauty-decay electrons in the combined heavy-flavor decay electron sample increases with momentum. This trend has been measured in pp collisions with ALICE [80, 81], and is shown in Figure 5.6 for pp collisions at $\sqrt{s} = 5.02$ TeV. This plot clearly shows that heavy-flavor decay electrons are mostly from charm decays in $2 < p_{\mathrm{T}} < 4$ GeV/c, but beauty-decay electrons begin to dominate at increased momentum. In the p_{T} range between 5-8 GeV/c, beauty-decay electrons make up about 60% of the heavy-flavor decay electrons.

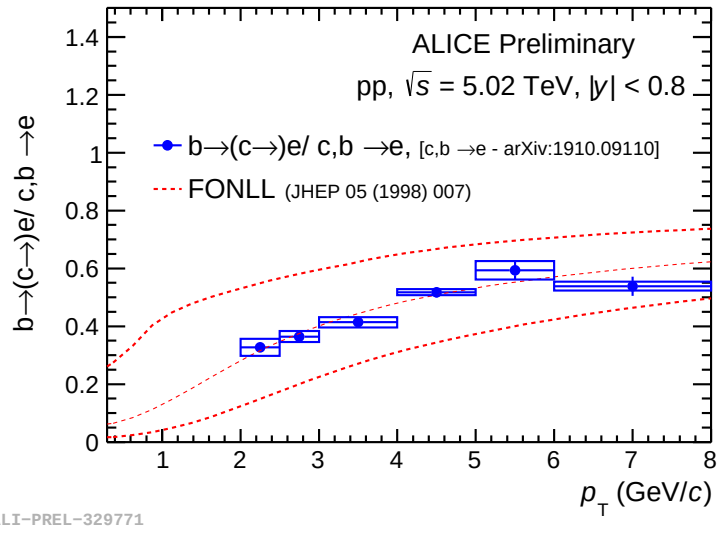

Figure 5.6: Fraction of beauty-decay electrons divided by heavy-flavor decay electrons (b/(b+c)) versus transverse momentum in pp collisions at $\sqrt{s} = 5.02$ TeV [80]. The red dashed lines are the FONLL model prediction and its uncertainty band.

The second reason for the overlap is that the mass-dependent effects of energy loss become negligible at high momentum [55]. This behavior can be seen in Figure 5.7, where the theoretical predictions of the beauty- and charm-decay electron R_{AA} are

shown. (Note that in this case, we are comparing beauty-decay electrons with *pure* charm-decay electrons.) In both the Djordjevic [66] and DAB-MOD M&T models [68], the two distributions begin to merge around $p_{\mathrm{T}} = 15$ GeV/c. This is completely independent of the composition of the heavy-flavor sample, since here we are comparing beauty-decay electrons with pure charm-decay electrons. Even in this ideal case, we see that the two distributions are expected to overlap at high momentum.

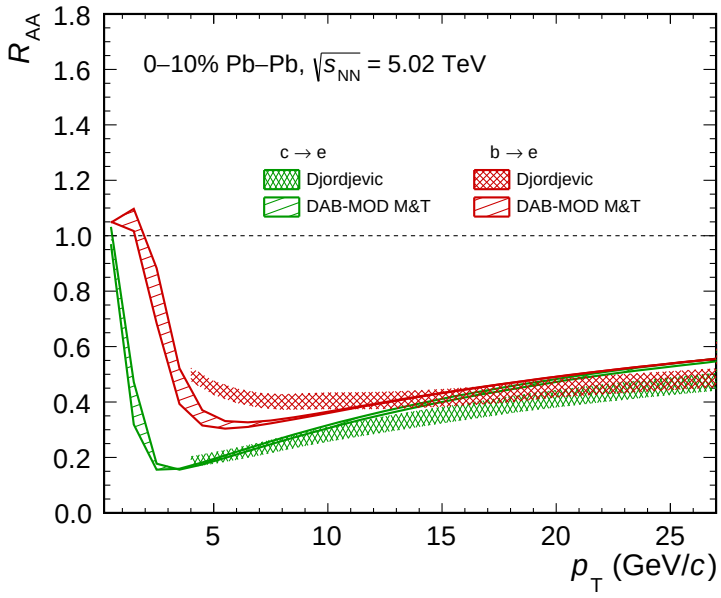

Figure 5.7: The DAB-MOD M&T [68] and Djordjevic model [66] predictions for charm- and beauty-decay electron R_{AA}.

Let us now consider these two effects in tandem: at what momentum do we expect the beauty-decay electron and heavy-flavor decay electron R_{AA} to overlap when both the higher beauty-decay electron fraction and the reduced mass-dependence of the energy loss are taken into account? This can be seen in predictions using the Djordjevic [66] and PHSD [67] models in Figure 5.8. In these predictions, the R_{AA} of beauty-decay and heavy-flavor decay electrons begin to merge around $p_{\mathrm{T}} \sim 10$ GeV/c. This is consistent with what is seen in Figure 5.5.

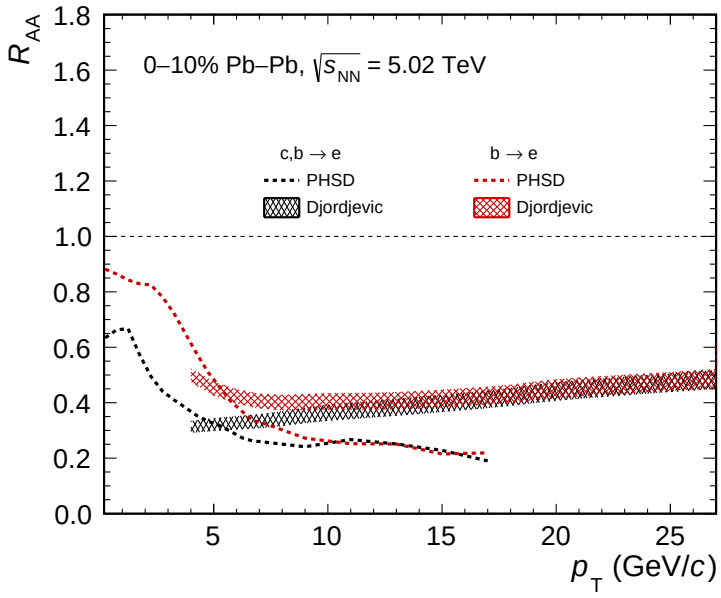

Figure 5.8: The PHSD [67] and Djordjevic model [66] predictions for heavy-flavor decay and beauty-decay electron R_{AA}.

5.2.3 Model predictions

The energy loss of high-p_{T} particles, extracted via model comparisons with the R_{AA}, can be used to estimate the density of the produced QGP medium. Past comparisons of RHIC data and a pQCD-based model with medium-modified parton fragmentation functions found that the initial gluon (energy) densities achieved in relativistic heavy ion collisions were 30 (100) times larger than in cold nuclei [152]. Similar estimates were obtained by modeling the QGP as an ultra-dense gluon gas; the experimental results were consistent with gluon densities of 1,100 per unit rapidity, corresponding to temperatures over 2 times the critical temperature predicted in lattice QCD and initial energy densities of 14-20 GeV/fm^3 [153]. For reference, cold nuclear matter has an energy density of 0.15 GeV/fm^3 [18], and lattice QCD predicts a phase transition around 1 GeV/fm^3 [15]. The good agreement between these theoretical models and R_{AA} results provide evidence that the conditions necessary to form a QGP have been met, and that the suppression seen in data is consistent with parton energy loss.

The R_{AA} results from this thesis analysis are compared with five theoretical models: Djordjevic [66], PHSD [67], MC@sHQ+EPOS2 [69], DAB-MOD M&T [68], and

LIDO [70]. Each has a different approach to reproducing the results of a heavy-ion collision, as discussed in Section 1.8. PHSD, MC@sHQ+EPOS2, DAB-MOD M&T, and LIDO are based on heavy-flavor quark transport modeling, while the Djordjevic model is based on pQCD calculations of energy loss by high-momentum partons. All models with the exception of PHSD include heavy-flavor energy loss via parton collisions in the medium and via gluon radiation. (PHSD only considers collisional energy loss.) The heavy-flavor quarks are hadronized via fragmentation in all the models. PHSD, MC@sHQ+EPOS2, and LIDO also include fragmentation via coalescence, in which partons close in phase space bind together to form hadrons.

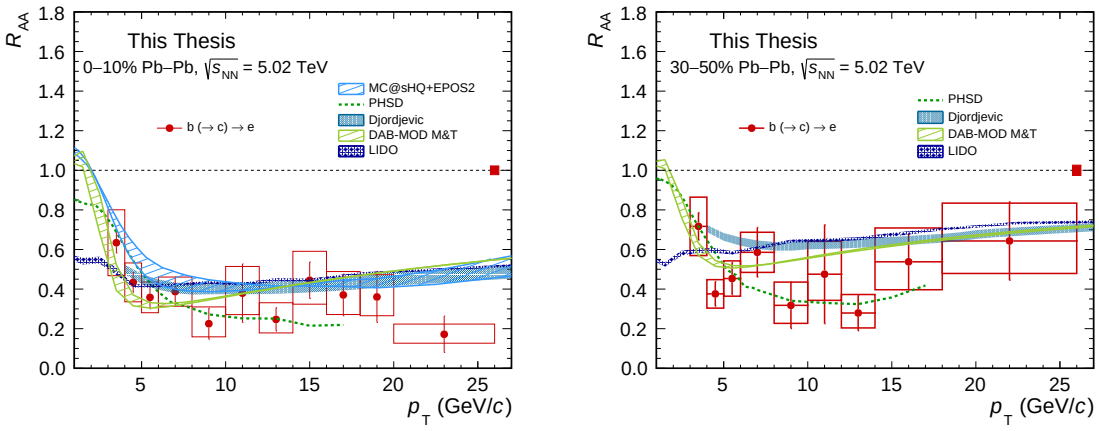

Figure 5.9: The R_{AA} of beauty-decay electrons compared with theoretical models: Djordjevic [66], PHSD [67], MC@sHQ+EPOS2 [69], DAB-MOD M&T [68], and LIDO [70].

Figure 5.9 shows the R_{AA} of beauty-decay electrons compared with the model predictions. Predictions from each model were provided via private correspondence with the theorists, and are available for both 0-10% and 30-50% centrality with the exception of MC@sHQ+EPOS2, which does not include a prediction for 30-50% centrality. Within the uncertainties of the measurement, all the model predictions are in agreement with the data points. The MC@sHQ+EPOS2, PHSD, and LIDO models are also in agreement with the beauty-decay electron v_2 measurement, discussed in Section 1.7 and shown again in Figure 5.10. This shows that the three models provide a good description of both the energy loss processes measured in the R_{AA} and the azimuthal anisotropy exhibited in the v_2 measurement.

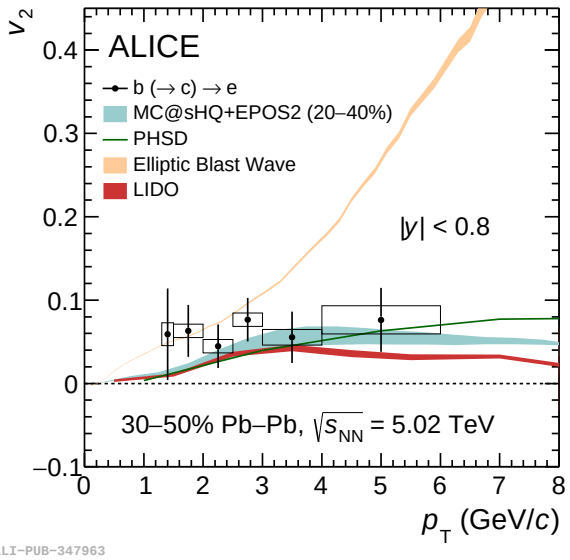

Figure 5.10: The elliptic flow v_2 of beauty-decay electrons measured in ALICE in 30-50% Pb-Pb collisions [63, 65].

The Djordjevic predictions, in agreement with the measurement, also predicted a negligible difference in the R_{AA} in collisions with $\sqrt{s_{\mathrm{NN}}}$ = 2.76 and 5.02 TeV, discussed in Section 5.2.1. This prediction relied on the assumption that the average increase in the medium temperature between the two energies is roughly 7%, and that both collisional and radiative energy loss has a non-trivial temperature dependence. The T-dependence used in the model is non-analytic, lying between a linear (T) and quadratic (T^2) dependence [82].

At high momentum, the different model predictions begin to merge with the exception of the PHSD prediction, which tends to dip lower than the other models. This is interesting, as PHSD is the only model shown here that does not include radiative energy loss, which is dominant at higher momentum. However, PHSD involves microscopic transport calculations, which are computationally very expensive. From private correspondence with the theorists, we have learned that at large momentum, the model can suffer from statistical fluctuations, particularly in the last few points (at p_{T} = 11, 13, 15, and 17 GeV/c). Thus some part of the deviation from other models may be due to low statistics. The PHSD model has been used recently to extract the spatial diffusion coefficient (D_s) for the charm quark [154]. The model

found that $2\pi TD_s \approx 2$ at the critical temperature for QGP formation, consistent with values obtained with lattice QCD calculations.

In 0-10% collisions, the model predictions vary the most for $p_{\mathrm{T}} < 5$ GeV/c. In this low-momentum region, the different treatments of the medium description and the hadronization processes can have an effect on the R_{AA} shape. For example, the LIDO prediction, which is lower than the other models at low-p_{T}, increases when only hadronization via fragmentation (not coalescence) is included. This can be seen in Figure 5.11. In future studies, it will be interesting to see whether smaller uncertainties will help further discriminate between the models in 0-10% collisions at low momentum. In 30-50%, the outlook is even more exciting, as the difference in the model predictions is more pronounced in a wider momentum range.

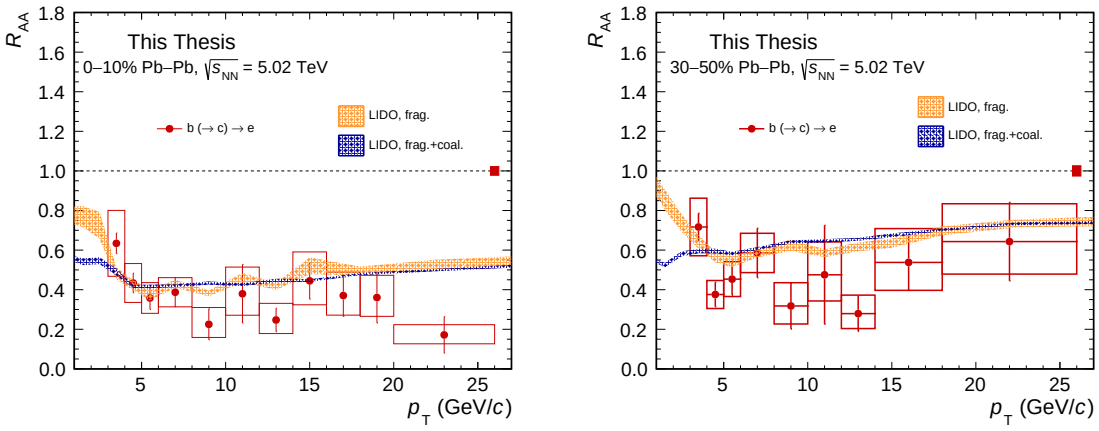

Figure 5.11: The R_{AA} of beauty-decay electrons compared with LIDO [70]. The full LIDO prediction with hadronization via fragmentation and coalescence is in blue; the prediction with hadronization via fragmentation alone is in orange.

Chapter 6: Summary and Outlook

Heavy-ion collisions offer a unique opportunity to study the Quark-Gluon Plasma in a laboratory setting. Though the QGP cannot be measured directly due to its short lifetime, the physics of the quarks and gluons within the medium can be deduced by the hadrons and decay products that are ultimately measured by the ALICE detector. In this thesis, we focused on measuring the physics of the beauty quark through electrons produced by beauty hadrons. Beauty quarks are useful probes of the QGP, as they are created very early in the collision process via hard parton-parton scattering. They experience the full evolution of the QGP and collision without changing flavor, then decay into particles we can measure with our detectors. They can be used to study the mass-dependence of different physical processes in the QGP, particularly energy loss processes. By comparing beauty and charm measurements, in this case, the beauty-decay electron and heavy-flavor decay electron R_{AA}, we can test whether the beauty quark loses less energy than the charm quark, as expected from the mass-dependent effects of energy loss.

The beauty-decay electron R_{AA} was measured using the excellent tracking and particle identification capabilities of the ALICE detector. The TPC and ITS provided the tracking and primary vertex reconstruction necessary to achieve good DCA resolution. The TPC also aided in the identification of electrons through energy loss measurements in the detector gas mixture. Finally, the EMCal provided additional separation power to isolate electrons from hadrons. It was also used to trigger on events with large energy depositions in the calorimeter material, which improved the statistics of high-momentum electrons. This allowed us to measure beauty-decay electrons to a higher momentum than ever before.

To isolate electrons from beauty-hadron decays from other electron sources, two techniques were used. The first was to remove photonic electrons by using an invariant mass analysis. Electrons that formed unlike-sign pairs with low invariant mass were subtracted from the sample. After that, the electrons in the sample were mainly produced in charm and beauty hadron decays. The charm- and beauty-decay electrons were separated by fitting their combined DCA distribution with two templates made in MC simulations, one for charm-decay electrons and one for beauty-decay

electrons. This was possible because the two heavy-flavor sources have different DCA shapes; because beauty hadrons have longer lifetimes before decaying into electrons, their decay electrons tend to have a wider DCA distribution.

Finally, to calculate the nuclear modification factor, R_{AA}, the beauty-decay electron yield measured in Pb-Pb collisions was divided by the cross-section of beauty-decay electrons in pp collisions, scaled by the nuclear thickness function $\langle T_{\mathrm{AA}} \rangle$. The measured R_{AA} agreed with previous measurements in the region of overlap, validating the analysis methods used in this thesis. In comparing the measured R_{AA} in two centrality classes, 0-10% and 30-50%, we saw a hint that the beauty quark is more suppressed in central collisions, likely due to a larger QGP medium created in the most head-on collisions. In addition, comparisons with past ALICE measurements at $\sqrt{s_{\mathrm{NN}}} = 2.76$ TeV revealed that the suppression of beauty-decay electrons has a negligible collision-energy dependence, at least in the overlapping region of $3 < p_{\mathrm{T}} < 8$ GeV/c. The beauty-decay electron R_{AA} was further compared with measurements of the heavy-flavor decay electron R_{AA} (from charm and beauty decays). In 0-10% centrality, there is a hint that at low-momentum (2-5 GeV/c) the beauty-decay electron R_{AA} was slightly higher, signalling less energy loss in the QGP. This is confirms our expectations that the mass-dependence of energy loss causes charm to be more suppressed than beauty. At higher momentum, the fraction of beauty-decay electrons in the heavy-flavor decay electron sample increases, and the mass-dependent effect of energy loss become negligible. Thus, the two distributions merged at higher momentum, as expected by theoretical models. Finally, the beauty-decay electron R_{AA} was compared with various theoretical predictions. There we saw the measurement does not yet have a small enough uncertainty to favor one model over another. However, this is the first time beauty-decay electrons have been measured at such a large momentum; future measurements may be able to refine the method to achieve more discriminatory power. In summary, this measurement supports the conclusion that 1) beauty quarks lose more energy in the QGP in head-on collisions versus more glancing collisions due to a larger QGP system size, 2) the suppression of beauty has a negligible collision-energy dependence when comparing results at $s_{\mathrm{AA}} = 2.76$ and 5.02 TeV, and 3) energy loss of quarks traveling through the QGP is mass-dependent and the mass-dependence is stronger at low momentum.

6.1 Outlook and Future measurements

Though measurements of beauty hadrons and decay particles in heavy-ion collisions have thus far been extensive and impressive, there is more work to be done! Currently, efforts are underway to measure beauty-decay electrons in a new data sample, also at $\sqrt{s_{\mathrm{NN}}} = 5.02$ TeV, which was taken by ALICE in 2018. This sample includes centrality-triggered data in addition to minimum bias triggered data. The centrality trigger selects events with certain signal thresholds in the V0 detector, which correspond to specific centrality ranges. In the 2018 sample, central, semi-central, and peripheral events were separately selected using the centrality trigger. This sample is expected to provide about 5× more statistics to improve the R_{AA} measurement at low-momentum. The acceptance and statistics of the measurement can also be improved with the inclusion of the DCal detector, an additional section of the EMCal located in a different ϕ range. The extra statistics could help determine the extent of the difference between the beauty-decay and heavy-flavor decay electrons (Figure 5.5) by decreasing the error bars. It would also aid in the comparison of the two centrality classes, especially if the systematic uncertainty estimation is performed on the double ratio of the 30-50% and 0-10% nuclear modification factors. Such a study would let us quantify the suppression in one centrality versus another, while taking into account the correlated uncertainties of the two measurements. Finally, the increased statistics may help discriminate between model predictions.

Taking a larger view of the study of beauty physics, the LHC is currently in a long shutdown (dubbed LS2) to allow for detector upgrades. These detector upgrades, along with the increased luminosity of the beams in future runs, will allow us to improve upon beauty measurements. Of particular note is the ITS upgrade [155], which will improve resolution, allowing better tracking and reconstruction of the secondary vertices from the decays of beauty hadrons. It is expected to allow us to measure fully reconstructed B meson decays (via the $B^+ \to \overline{D^0}\pi^+$ channel) down to $p_{\mathrm{T}} = 2$ GeV/c and the Λ_b baryon down to around $p_{\mathrm{T}} = 7$ GeV/c. The B meson measurement would be a first for ALICE, and the Λ_b baryon measurement has not yet been performed by any heavy-ion experiment. The comparison of B mesons (b+light quark) and Λ_b (udb) will allow us to test the hadronization processes of the beauty quark, as it is expected that coalescence would increase the relative fraction of baryons like Λ_b over mesons. Also, the full reconstruction of beauty hadrons will

allow us to compare with measurements of reconstructed charm hadrons to have a more direct comparison of the charm and beauty R_{AA}, and thus the mass-dependence of energy loss. Thus the future of beauty studies in heavy-ion physics is filled with new possibilities.

Bibliography

[1]S. Sarkar, H. Satz, and B. C. Sinha, *The Physics of the Quark-Gluon Plasma*, Lect. Notes Phys., 785 (Springer, Heidelberg ; 2010).

[2]U. Heinz and M. Jacob, "Evidence for a New State of Matter: An Assessment of the Results from the CERN Lead Beam Programme", arXiv:nucl-th/0002042 (2000).

[3]I. Arsene et al., "Quark–gluon plasma and color glass condensate at RHIC? The perspective from the BRAHMS experiment", Nuclear Physics A, First Three Years of Operation of RHIC **757**, 1–27 (2005).

[4]B. B. Back et al., "The PHOBOS perspective on discoveries at RHIC", Nuclear Physics A, First Three Years of Operation of RHIC **757**, 28–101 (2005).

[5]J. Adams et al., "Experimental and theoretical challenges in the search for the quark–gluon plasma: The STAR Collaboration's critical assessment of the evidence from RHIC collisions", Nuclear Physics A, First Three Years of Operation of RHIC **757**, 102–183 (2005).

[6]K. Adcox et al., "Formation of dense partonic matter in relativistic nucleus–nucleus collisions at RHIC: Experimental evaluation by the PHENIX Collaboration", Nuclear Physics A, First Three Years of Operation of RHIC **757**, 184–283 (2005).

[7]P. Zyla et al., "Review of Particle Physics", PTEP **2020**, 083C01 (2020).

[8]T. C. Mcevilley, *The Shape of Ancient Thought: Comparative Studies in Greek and Indian Philosophies* (Skyhorse Publishing Company, Incorporated, New York, United States, 2001).

[9]R. Hooke, *Micrographia, or, Some physiological descriptions of minute bodies made by magnifying glasses with observations and inquiries thereupon* (London, England, 1665).

[10]J. Dalton, *A new system of chemical philosophy* (Printed by S. Russell for R. Bickerstaff, London, W. Dawson & Sons, Manchester, London, 1808).

[11]D. J. Gross and F. Wilczek, "Ultraviolet Behavior of Non-Abelian Gauge Theories", Phys. Rev. Lett. **30**, 1343–1346 (1973).

[12]H. D. Politzer, "Reliable Perturbative Results for Strong Interactions?", Phys. Rev. Lett. **30**, 1346–1349 (1973).

[13]J. C. Collins and M. J. Perry, "Superdense Matter: Neutrons or Asymptotically Free Quarks?", Phys. Rev. Lett. **34**, 1353–1356 (1975).

[14]N. Cabibbo and G. Parisi, "Exponential hadronic spectrum and quark liberation", Phys. Lett. B **59**, 67–69 (1975).

[15]F. Karsch, "Lattice QCD at High Temperature and Density", Lect. Notes Phys. **583**, 209–249 (2002).

[16]S. Borsányi et al., "Is there still any T_c mystery in lattice QCD? Results with physical masses in the continuum limit III", J. High Energ. Phys. **2010**, 73 (2010).

[17]A. Bazavov et al., "Equation of state in $(2 + 1)$-flavor QCD", Phys. Rev. D **90**, 094503 (2014).

[18]A. Andronic, "An overview of the experimental study of quark-gluon matter in high-energy nucleus-nucleus collisions", Int. J. Mod. Phys. A **29**, 1430047 (2014).

[19]J. D. Bjorken, "Highly relativistic nucleus-nucleus collisions: The central rapidity region", Phys. Rev. D **27**, 140–151 (1983).

[20]P. Koch, B. Müller, and J. Rafelski, "Strangeness in relativistic heavy ion collisions", Physics Reports **142**, 167–262 (1986).

[21]T. Matsui and H. Satz, "J/ψ suppression by quark-gluon plasma formation", Phys. Lett. B **178**, 416–422 (1986).

[22]F. Karsch, M. T. Mehr, and H. Satz, "Color screening and deconfinement for bound states of heavy quarks", Z. Phys. C - Particles and Fields **37**, 617–622 (1988).

[23]J. Bjorken, "Energy Loss of Energetic Partons in Quark-Gluon Plasma: Possible Extinction of High p_T Jets in Hadron-Hadron Collisions", FERMILAB-PUB-82-059-THY, FERMILAB-PUB-82-059-T (1982).

[24]E. Andersen et al., "Strangeness enhancement at mid-rapidity in Pb–Pb collisions at 158 A GeV/c", Phys. Lett. B **449**, 401–406 (1999).

[25]M. K. Mitrovski and The NA49 Collaboration, "Strangeness production at SPS energies from NA49", J. Phys. G: Nucl. Part. Phys. **32**, S43–S50 (2006).

[26]M. C. Abreu et al., "Evidence for deconfinement of quarks and gluons from the J/ψ suppression pattern measured in Pb-Pb collisions at the CERN-SPS", Phys. Lett. B **477**, 28–36 (2000).

[27]STAR Collaboration, "Disappearance of Back-To-Back High-p_T Hadron Correlations in Central Au + Au Collisions at $\sqrt{s_{NN}} = 200$ GeV", Phys. Rev. Lett. **90**, 082302 (2003).

[28]D. H. Hathaway, *The Solar Interior*, `https://solarscience.msfc.nasa.gov/interior.shtml`, Oct. 2015.

[29]G. Martinez, "Advances in Quark Gluon Plasma", arXiv:1304.1452 [nucl-ex] (2013).

[30]W. Busza, K. Rajagopal, and W. van der Schee, "Heavy Ion Collisions: The Big Picture, and the Big Questions", Annu. Rev. Nucl. Part. Sci. **68**, 339–376 (2018).

[31]A. Toia, *Participants and spectators at the heavy-ion fireball*, `https://cerncourier.com/a/participants-and-spectators-at-the-heavy-ion-fireball/`, Apr. 2013.

[32]R. Snellings, "Elliptic flow: a brief review", New J. Phys. **13**, 055008 (2011).

[33]F.-M. Liu and S.-X. Liu, "Quark-gluon plasma formation time and direct photons from heavy ion collisions", Phys. Rev. C **89**, 034906 (2014).

[34]V. Greco, C. M. Ko, and P. Lévai, "Parton Coalescence and the Antiproton/Pion Anomaly at RHIC", Phys. Rev. Lett. **90**, 202302 (2003).

[35]X. Dong, Y.-J. Lee, and R. Rapp, "Open Heavy-Flavor Production in Heavy-Ion Collisions", Annual Review of Nuclear and Particle Science **69**, 417–445 (2019).

[36]ALICE Collaboration, "Measurement of D^0, D^+, D^{*+} and D_s^+ production in Pb-Pb collisions at $\sqrt{s_{NN}} = 5.02$ TeV", J. High Energ. Phys. **2018**, 174 (2018).

[37]CMS Collaboration, "Measurement of the $B^{\pm}$ Meson Nuclear Modification Factor in Pb-Pb Collisions at $\sqrt{s_{NN}} = 5.02$ TeV", Phys. Rev. Lett. **119**, 152301 (2017).

[38]Y. L. Dokshitzer and D. E. Kharzeev, "Heavy quark colorimetry of QCD matter", Phys. Lett. B **519**, 199–206 (2001).

[39]M. L. Miller, K. Reygers, S. J. Sanders, and P. Steinberg, "Glauber Modeling in High-Energy Nuclear Collisions", Annu. Rev. Nucl. Part. Sci. **57**, 205–243 (2007).

[40]R. J. Glauber, "Cross Sections in Deuterium at High Energies", Phys. Rev. **100**, 242–248 (1955).

[41]R. J. Glauber, "Quantum Optics and Heavy Ion Physics", Nuclear Physics A, QUARK MATTER 2005 **774**, 3–13 (2006).

[42]I. Vitev, T. Goldman, M. B. Johnson, and J. W. Qiu, "Open charm tomography of cold nuclear matter", Phys. Rev. D **74**, 054010 (2006).

[43]ALICE Collaboration, "Measurement of prompt D^0, D^+, D^{*+}, and D_s^+ production in p–Pb collisions at $\sqrt{s_{NN}} = 5.02$ TeV", J. High Energ. Phys. **2019**, 92 (2019).

[44]Z.-B. Kang et al., "Multiple scattering effects on heavy meson production in p+A collisions at backward rapidity", Phys. Lett. B **740**, 23–29 (2015).

[45]ALICE Collaboration, "Measurement of electrons from beauty-hadron decays in p-Pb collisions at $\sqrt{s_{NN}}= 5.02$ TeV and Pb-Pb collisions at $\sqrt{s_{NN}}= 2.76$ TeV", J. High Energ. Phys. **2017**, 52 (2017).

[46]ALICE Collaboration, "Transverse momentum spectra and nuclear modification factors of charged particles in pp, p-Pb and Pb-Pb collisions at the LHC", J. High Energ. Phys. **2018**, 13 (2018).

[47]ALICE Collaboration, "Measurement of the production of high-p_T electrons from heavy-flavour hadron decays in Pb-Pb collisions at $\sqrt{s_{NN}} = 2.76$ TeV", Phys. Lett. B **771**, 467–481 (2017).

[48]ALICE Collaboration, "Prompt and non-prompt J/ψ production and nuclear modification at mid-rapidity in p–Pb collisions at $\sqrt{s_{NN}} = \mathbf{5.02}$ TeV", Eur. Phys. J. C **78**, 466 (2018).

[49]CMS Collaboration, "Measurement of prompt and nonprompt charmonium suppression in PbPb collisions at 5.02 tev", Eur. Phys. J. C **78**, 509 (2018).

[50]CMS Collaboration, "Studies of Beauty Suppression via Nonprompt D^0 Mesons in Pb-Pb Collisions at $\sqrt{s_{NN}} = 5.02$ TeV", Phys. Rev. Lett. **123**, 022001 (2019).

[51]F. Si et al., "Charm and beauty isolation from heavy flavor decay electrons in Au+Au collisions at sNN = 200 GeV at RHIC", Phys. Lett. B **805**, 135465 (2020).

[52]PHENIX Collaboration, "Single electron yields from semileptonic charm and bottom hadron decays in Au+Au collisions at $\sqrt{s_{NN}}= 200$ GeV", Phys. Rev. C **93**, 034904 (2016).

[53]ALICE Collaboration, "Measurement of electrons from semileptonic heavy-flavour hadron decays at midrapidity in pp and Pb-Pb collisions at $\sqrt{s_{\rm NN}}$ = 5.02 TeV", Phys. Lett. B **804**, 135377 (2020).

[54]ALICE Collaboration, "Production of muons from heavy-flavour hadron decays at high transverse momentum in Pb-Pb collisions at $\sqrt{s_{\rm NN}}$= 5.02 and 2.76 TeV", arXiv:2011.05718 [hep-ex, physics:nucl-ex] (2020).

[55]N. Armesto, A. Dainese, C. A. Salgado, and U. A. Wiedemann, "Testing the color charge and mass dependence of parton energy loss with heavy-to-light ratios at BNL RHIC and CERN LHC", Phys. Rev. D **71**, 054027 (2005).

[56]P. Foka and M. A. Janik, "An overview of experimental results from ultra-relativistic heavy-ion collisions at the CERN LHC: bulk properties and dynamical evolution", Reviews in Physics **1**, 154–171 (2016).

[57]S. Voloshin and Y. Zhang, "Flow study in relativistic nuclear collisions by Fourier expansion of azimuthal particle distributions", Z Phys C - Particles and Fields **70**, 665–671 (1996).

[58]P. F. Kolb and U. Heinz, "Hydrodynamic description of ultrarelativistic heavy-ion collisions", arXiv:nucl-th/0305084 (2003).

[59]S. Batsouli, S. Kelly, M. Gyulassy, and J. L. Nagle, "Does the Charm Flow at RHIC?", Phys. Lett. B **557**, 26–32 (2003).

[60]M. Gyulassy, I. Vitev, and X.-N. Wang, "High p_T Azimuthal Asymmetry in Non-central A+A at RHIC", Phys. Rev. Lett. **86**, 2537–2540 (2001).

[61]E. V. Shuryak, "Azimuthal asymmetry at large p_t seem to be too large for a pure "jet quenching"", Phys. Rev. C **66**, 027902 (2002).

[62]J. Noronha-Hostler, B. Betz, J. Noronha, and M. Gyulassy, "Event-by-Event Hydrodynamics+Jet Energy Loss: A Solution to the $R_{AA} \bigotimes v_2$ Puzzle", Phys. Rev. Lett. **116**, 252301 (2016).

[63]ALICE Collaboration, "Elliptic flow of electrons from beauty-hadron decays in Pb-Pb collisions at $\sqrt{s_{\rm NN}}$ = 5.02 TeV", arXiv:2005.11130 [hep-ex, physics:nucl-ex] (2020).

[64]K. Reygers, A. Schmah, A. Berdnikova, and X. Sun, "Blast-wave description of Υ elliptic flow at energies available at the CERN Large Hadron Collider", Phys. Rev. C **101**, 064905 (2020).

[65]ALICE Collaboration, "D-meson azimuthal anisotropy in mid-central Pb-Pb collisions at $\sqrt{s_{\mathrm{NN}}} = 5.02$ TeV", Phys. Rev. Lett. **120**, 102301 (2018).

[66]D. Zigic et al., "DREENA-B framework: First predictions of RAA and v2 within dynamical energy loss formalism in evolving QCD medium", Phys. Lett. B **791**, 236–241 (2019).

[67]T. Song et al., "Tomography of the quark-gluon plasma by charm quarks", Phys. Rev. C **92**, 014910 (2015).

[68]C. A. G. Prado et al., "Event-by-event correlations between soft hadrons and D^0 mesons in 5.02 TeV PbPb collisions at the CERN Large Hadron Collider", Phys. Rev. C **96**, 064903 (2017).

[69]M. Nahrgang, J. Aichelin, P. B. Gossiaux, and K. Werner, "Influence of hadronic bound states above T_c on heavy-quark observables in Pb + Pb collisions at the CERN Large Hadron Collider", Phys. Rev. C **89**, 014905 (2014).

[70]W. Ke, Y. Xu, and S. A. Bass, "Linearized Boltzmann-Langevin model for heavy quark transport in hot and dense QCD matter", Phys. Rev. C **98**, 064901 (2018).

[71]M. Cacciari, M. Greco, and P. Nason, "The pT spectrum in heavy-flavour hadroproduction", J. High Energy Phys. **1998**, 007–007 (1998).

[72]M. Cacciari et al., "Theoretical predictions for charm and bottom production at the LHC", J. High Energ. Phys. **2012**, 137 (2012).

[73]W. Cassing, "From Kadanoff-Baym dynamics to off-shell parton transport", Eur. Phys. J. Spec. Top. **168**, 3–87 (2009).

[74]W. Cassing, "Dynamical quasiparticles properties and effective interactions in the sQGP", Nuclear Physics A **795**, 70–97 (2007).

[75]K. Saraswat, P. Shukla, V. Kumar, and V. Singh, "Energy loss of heavy quarks and B and D meson spectra in PbPb collisions at LHC energies", Nuclear Physics A **961**, 169–182 (2017).

[76]R. J. Fries, S. A. Bass, B. Muller, and C. Nonaka, "Hadronization in heavy ion collisions: Recombination and fragmentation of partons", Phys. Rev. Lett. **90**, 202303 (2003).

[77]CMS Collaboration, "Measurement of the differential inclusive B^+ hadron cross sections in pp collisions at $\sqrt{s}$= 13 TeV", Phys. Lett. B **771**, 435–456 (2017).

[78]ALICE Collaboration, "Measurement of beauty and charm production in pp collisions at $\sqrt{s}$= 5.02 TeV via non-prompt and prompt D mesons", arXiv:2102.13601 [hep-ex, physics:nucl-ex] (2021).

[79]B. Abelev et al., "Beauty production in pp collisions at $\sqrt{s}$= 2.76 TeV measured via semi-electronic decays", Phys. Lett. B **738**, 97–108 (2014).

[80]M. Cai, *Beauty production with ALICE at the LHC*, `https://cds.cern.ch/record/2722080`, June 2020.

[81]ALICE Collaboration, "Measurement of electrons from beauty hadron decays in pp collisions at $\sqrt{s}$= 7 TeV", Phys. Lett. B **721**, 13–23 (2013).

[82]M. Djordjevic and M. Djordjevic, "Predictions of heavy-flavor suppression at 5.1 TeV Pb + Pb collisions at the CERN Large Hadron Collider", Phys. Rev. C **92**, 024918 (2015).

[83]M. Cacciari et al., "Theoretical predictions for charm and bottom production at the LHC", J. High Energ. Phys. **2012**, 137 (2012).

[84]V. G. Kartvelishvili, A. K. Likhoded, and V. A. Petrov, "On the fragmentation functions of heavy quarks into hadrons", Phys. Lett. B **78**, 615–617 (1978).

[85]T. Sjöstrand et al., "An Introduction to PYTHIA 8.2", Computer Physics Communications **191**, 159–177 (2015).

[86]H. Berrehrah et al., "Collisional processes of on-shell and off-shell heavy quarks in vacuum and in the quark-gluon plasma", Phys. Rev. C **89**, 054901 (2014).

[87]H. Berrehrah et al., "Dynamical collisional energy loss and transport properties of on- and off-shell heavy quarks in vacuum and in the quark gluon plasma", Phys. Rev. C **90**, 064906 (2014).

[88]E. L. Bratkovskaya et al., "Heavy flavor in relativistic heavy-ion collisions", J. Phys.: Conf. Ser. **668**, 012008 (2016).

[89]ALICE Collaboration, "Suppression of high transverse momentum D mesons in central Pb-Pb collisions at $\sqrt{s_{\mathrm{NN}}} = 2.76$ TeV", J. High Energ. Phys. **2012**, 112 (2012).

[90]R. Katz et al., "Heavy-flavor dynamics in event-by-event viscous hydrodynamic backgrounds", arXiv:1812.08009 [nucl-th] (2019).

[91]J. Noronha-Hostler et al., "Bulk viscosity effects in event-by-event relativistic hydrodynamics", Phys. Rev. C **88**, 044916 (2013).

[92]G. D. Moore and D. Teaney, "How Much do Heavy Quarks Thermalize in a Heavy Ion Collision?", Phys. Rev. C **71**, 064904 (2005).

[93]C. Peterson, D. Schlatter, I. Schmitt, and P. M. Zerwas, "Scaling violations in inclusive e^+e^- annihilation spectra", Phys. Rev. D **27**, 105–111 (1983).

[94]K. Werner et al., "Event-by-event simulation of the three-dimensional hydrodynamic evolution from flux tube initial conditions in ultrarelativistic heavy ion collisions", Phys. Rev. C **82**, 044904 (2010).

[95]Y. Xu et al., "Data-driven analysis for the temperature and momentum dependence of the heavy-quark diffusion coefficient in relativistic heavy-ion collisions", Phys. Rev. C **97**, 014907 (2018).

[96]C. Shen et al., "The iEBE-VISHNU code package for relativistic heavy-ion collisions", Computer Physics Communications **199**, 61–85 (2016).

[97]J. S. Moreland, J. E. Bernhard, and S. A. Bass, "Alternative ansatz to wounded nucleon and binary collision scaling in high-energy nuclear collisions", Phys. Rev. C **92**, 011901 (2015).

[98]S. A. Bass et al., "Microscopic models for ultrarelativistic heavy ion collisions", Progress in Particle and Nuclear Physics **41**, 255–369 (1998).

[99]M. Bleicher et al., "Relativistic hadron-hadron collisions in the ultra-relativistic quantum molecular dynamics model", J. Phys. G: Nucl. Part. Phys. **25**, 1859–1896 (1999).

[100]L. Evans and P. Bryant, "LHC Machine", Journal of Instrumentation **3**, S08001–S08001 (2008).

[101]A. Breskin and R. Voss, *The CERN Large Hadron Collider: Accelerator and Experiments* (CERN, Geneva, 2009).

[102]J. Amos, *Large Hadron Collider can be 'world's biggest rain meter'*, https://www.bbc.com/news/science-environment-36094282, Apr. 2016.

[103]M. Schaumann, *LHC report: xenon in action*, https://home.cern/news/news/accelerators/lhc-report-xenon-action, Oct. 2017.

[104]ALICE Collaboration, "The ALICE experiment at the CERN LHC", Journal of Instrumentation **3**, S08002–S08002 (2008).

[105]ATLAS Collaboration, "The ATLAS Experiment at the CERN Large Hadron Collider", Journal of Instrumentation **3**, S08003–S08003 (2008).

[106]CMS Collaboration, "The CMS experiment at the CERN LHC", Journal of Instrumentation **3**, S08004–S08004 (2008).

[107]LHCb Collaboration, "The LHCb Detector at the LHC", Journal of Instrumentation **3**, S08005–S08005 (2008).

[108]LHCf Collaboration, "The LHCf detector at the CERN Large Hadron Collider", Journal of Instrumentation **3**, S08006–S08006 (2008).

[109]B. Acharya et al., "The physics programme of the MoEDAL experiment at the LHC", Int. J. Mod. Phys. A **29**, 1430050 (2014).

[110]TOTEM Collaboration, "The TOTEM Experiment at the CERN Large Hadron Collider", Journal of Instrumentation **3**, S08007–S08007 (2008).

[111]G. Aad et al., "Observation of a new particle in the search for the Standard Model Higgs boson with the ATLAS detector at the LHC", Phys. Lett. B **716**, 1–29 (2012).

[112]S. Chatrchyan et al., "Observation of a new boson at a mass of 125 GeV with the CMS experiment at the LHC", Phys. Lett. B **716**, 30–61 (2012).

[113]ALICE Collaboration, "The ALICE Transition Radiation Detector: Construction, operation, and performance", Nucl. Inst. Meth. A **881**, 88–127 (2018).

[114]A. Akindinov et al., "Space charge limited avalanche growth in multigap resistive plate chambers", Eur. Phys. J. C **34**, s325–s331 (2004).

[115]ALICE Collaboration, "Alignment of the ALICE Inner Tracking System with cosmic-ray tracks", Journal of Instrumentation **5**, P03003–P03003 (2010).

[116]D. Nouais et al., "The ALICE Silicon Drift Detector system", Nucl. Inst. Meth. A, Proceedings of the 10th International Workshop on Vertex Detectors **501**, 119–125 (2003).

[117]J. Alme et al., "The ALICE TPC, a large 3-dimensional tracking device with fast readout for ultra-high multiplicity events", Nucl. Inst. Meth. A **622**, 316–367 (2010).

[118]G. Dellacasa et al., *ALICE time projection chamber: Technical Design Report*, Technical design report. ALICE, CERN-LHCC-2000-001, CERN-OPEN-2000-183, ALICE-TDR-7 (CERN, Geneva, 2000).

[119]R. Frühwirth, "Application of Kalman filtering to track and vertex fitting", Nucl. Inst. Meth. A **262**, 444–450 (1987).

[120]ALICE Collaboration, "Performance of the ALICE experiment at the CERN LHC", Int. J. Mod. Phys. A **29**, 1430044 (2014).

[121]P. Cortese et al., *ALICE electromagnetic calorimeter technical design report*, tech. rep., CERN-LHCC-2008-014, ALICE-TDR-14 (Aug. 2008).

[122]U. Abeysekara et al., *ALICE EMCal Physics Performance Report*, tech. rep., arXiv:1008.0413 (Aug. 2010).

[123]F. Ronchetti and the ALICE Collaboration, "The ALICE electromagnetic calorimeter project", Journal of Physics: Conference Series **160**, 012012 (2009).

[124]A. Fantoni and the ALICE collaboration, "The ALICE Electromagnetic Calorimeter: EMCAL", Journal of Physics: Conference Series **293**, 012043 (2011).

[125]T. R. P.-R. Aronsson, "Cross section of bottom electrons in proton-proton collisions in the ALICE experiment", CERN-THESIS-2014-461, PhD thesis (Yale University, Dec. 2018).

[126]G. C. Balbastre, "Study of the strong interaction with high-energy photons at the LHC: Experience with the ALICE-EMCal detector operation and measurements", tel-02306044, Report/Thesis (Université Grenoble Alpes, Oct. 2019).

[127]T. C. Awes et al., "A simple method of shower localization and identification in laterally segmented calorimeters", Nucl. Inst. Meth. A **311**, 130–138 (1992).

[128]S. Acharya et al., "Production of π^0 and η mesons up to high transverse momentum in pp collisions at 2.76 TeV", Eur. Phys. J. C **77**, 339 (2017).

[129]O. Bourrion et al., "The ALICE EMCal L1 trigger first year of operation experience", Journal of Instrumentation **8**, C01013–C01013 (2013).

[130]M. Krivda et al., "The ALICE Central Trigger Processor (CTP) upgrade", Journal of Instrumentation **11**, C03051–C03051 (2016).

[131]P. Cortese et al., *ALICE forward detectors: FMD, TO and VO: Technical Design Report*, Technical design report. ALICE, CERN-LHCC-2004-025, ALICE-TDR-11 (CERN, Geneva, 2004).

[132]ALICE Collaboration, "Centrality determination of Pb-Pb collisions at $\sqrt{s_{\mathrm{NN}}}$= 2.76 TeV with ALICE", Phys. Rev. C **88**, 044909 (2013).

[133]ALICE Collaboration, *Centrality determination in heavy ion collisions*, ALICE-PUBLIC-2018-011, Aug. 2018.

[134]B. Alver, M. Baker, C. Loizides, and P. Steinberg, "The PHOBOS Glauber Monte Carlo", arXiv:0805.4411 [nucl-ex] (2008).

[135]C. Loizides, J. Kamin, and D. d'Enterria, "Improved Monte Carlo Glauber predictions at present and future nuclear colliders", Phys. Rev. C **97**, 054910 (2018).

[136]C. Loizides, J. Kamin, and D. d'Enterria, "Erratum: Improved Monte Carlo Glauber predictions at present and future nuclear colliders [Phys. Rev. C 97, 054910 (2018)]", Phys. Rev. C **99**, 019901 (2019).

[137]H. De Vries, C. W. De Jager, and C. De Vries, "Nuclear charge-density-distribution parameters from elastic electron scattering", Atomic Data and Nuclear Data Tables **36**, 495–536 (1987).

[138]X.-N. Wang and M. Gyulassy, "HIJING 1.0: A Monte Carlo Program for Parton and Particle Production in High Energy Hadronic and Nuclear Collisions", Computer Physics Communications **83**, 307–331 (1994).

[139]P. Z. Skands, "Tuning Monte Carlo Generators: The Perugia Tunes", Phys. Rev. D **82**, 074018 (2010).

[140]R. Brun et al., *GEANT: Detector Description and Simulation Tool*, CERN-W-5013, Geneva, 1993.

[141]W. Blum, W. Riegler, and L. Rolandi, *Particle Detection with Drift Chambers*, 2nd ed., Particle Acceleration and Detection (Springer, Berlin, 2008).

[142]ALICE Collaboration, "Energy dependence of the transverse momentum distributions of charged particles in pp collisions measured by ALICE", Eur. Phys. J. C **73**, 2662 (2013).

[143]ALICE Collaboration, "Measurements of low-p_{T} electrons from semileptonic heavy-flavour hadron decays at mid-rapidity in pp and Pb-Pb collisions at $\sqrt{\mathbf{s}_{\mathrm{NN}}} = 2.76$ TeV", J. High Energ. Phys. **2018**, 61 (2018).

[144]C. Oleari, "The POWHEG-BOX", Nucl. Phys. B - Proceedings Supplements **205-206**, 36–41 (2010).

[145]ALICE Collaboration, "Measurement of electrons from semileptonic heavy-flavour hadron decays in pp collisions at $\sqrt{s} = 7$ TeV", Phys. Rev. D **86**, 112007 (2012).

[146]F. James, *Statistical Methods in Experimental Physics*, 2nd ed. (World Scientific, Nov. 2006).

[147]M. He, R. J. Fries, and R. Rapp, "Heavy flavor at the large hadron collider in a strong coupling approach", Phys. Lett. B **735**, 445–450 (2014).

[148]L. Vermunt, "Measurement of Λ_{c}^{+} baryons and $\mathrm{D}_{\mathrm{s}}^{+}$ mesons in Pb-Pb collisions with ALICE", arXiv:1910.11738 [nucl-ex] (2019).

[149]ALICE Collaboration, "Λ_{c}^{+} production in Pb–Pb collisions at $\sqrt{s_{\mathrm{NN}}}$= 5.02 TeV", Phys. Lett. B **793**, 212–223 (2019).

[150]C. d. Conti, "Measurement of electrons from open heavy-flavor hadron decays in pp at $\sqrt{s} = 13$ TeV and electrons from beauty-hadron decays in Pb-Pb at $\sqrt{s_{\mathrm{NN}}} =$ 5.02 TeV collisions by ALICE at LHC", PhD thesis (Universidade de São Paulo, Mar. 2019).

[151]The ALICE Collaboration, "Transverse momentum spectra and nuclear modification factors of charged particles in pp, p-Pb and Pb-Pb collisions at the LHC", J. High Energ. Phys. **2018**, 13 (2018).

[152]X.-N. Wang, "Discovery of jet quenching and beyond", Nuclear Physics A **750**, 98–120 (2005).

[153]P. Braun-Munzinger and J. Stachel, "The quest for the quark–gluon plasma", Nature **448**, 302–309 (2007).

[154]X. Dong and V. Greco, "Heavy quark production and properties of Quark–Gluon Plasma", Progress in Particle and Nuclear Physics **104**, 97–141 (2019).

[155]B. Abelev et al, "Technical Design Report for the Upgrade of the ALICE Inner Tracking System", J. Phys. G: Nucl. Part. Phys. **41**, 087002 (2014).